Investigation into the resonance behaviour of the internal water column of an open-ended monopile

MSc Offshore and Dredging Engineering

Ernst Mulder

Delft University of Technology

TU Delft

Investigation into the resonance behaviour of the internal water column of an open-ended monopile

MSc Offshore and Dredging Engineering

by

Ernst Mulder

Student number:	4605152	
Project Duration:	February, 2023 - January, 2024	
Thesis committee:	Dr. B. Font,	Delft University of Technology
	Dr. D. Fiscaletti,	Delft University of Technology
	Ir. D.A. Fidalgo Domingos,	Delft University of Technology
	Dr.ir. P.R. Wellens,	Delft University of Technology (chair)
	Ir. E. Kalker,	Van Oord
Faculty:	Faculty of Mechanical Engineering, Delft	

TU Delft

Van Oord
Marine ingenuity

Preface

This report presents my Master's thesis in Offshore and Dredging Engineering at TU Delft. Having enjoyed the diverse courses within the Master program, the primary objective of this thesis is to successfully graduate from the program and contribute meaningfully to the field of offshore wind engineering. My thesis research primarily focuses on hydrodynamics, a subject that connects my Bachelor background as a Maritime Engineer with my current Master's studies.

Throughout my thesis research, I had the privilege of working as an intern at Van Oord, a leading international contractor in dredging, marine engineering, and offshore projects. I am grateful for the opportunity to gain practical experience and apply the theoretical knowledge acquired during my studies. I extend my sincere thanks to my professor at TU Delft, Dr. ir. Peter Wellens, for providing valuable feedback on my work and guiding me on areas for improvement. At Van Oord, special thanks to Edwin Kalker and James Braithwaite for their dedicated efforts in helping me achieve the final result. I am also grateful to the entire Hydrodynamics department at Van Oord, who were always willing to assist and engage in discussions.

Finally, a heartfelt thanks to my family, friends, and girlfriend for their unwavering motivation, belief, and unconditional support.

Ernst Mulder
Delft, January 2024

Abstract

The offshore wind industry is increasingly constructing wind turbines farther from the coast, in deeper water, and under more extreme conditions. This requires larger (monopile) foundations and necessitates new installation methods. An important factor affecting workability is the dynamic behavior of the monopile during installation.

The objective of this thesis is to develop a method for determining the hydrodynamic loads caused by internal sloshing in an open-ended monopile (MP) as it transitions from a horizontal to a vertical position in the splash zone.

First, the resonance frequencies of the internal water column are predicted with analytical approximations based on linear theory. Distinction is made between piston mode and sloshing. Two numerical methods, linear potential flow (LPF), and computational fluid dynamics (CFD) are used to verify the resonance frequencies. Since the CFD analysis is done in 2D, a 2D representation of the open-ended monopile is considered. Due to the presence of viscous effects in CFD, the resonance observed with CFD consistently occurs at a lower frequency than for the analytical and LPF methods. Also it is found that an decrease in inclination angle of the monopile with respect to the horizontal, while maintaining the same submerged length, results in lower resonance frequency for both piston mode and sloshing in both LPF and CFD.

To assess the accuracy of LPF in describing the motion of the internal water column, it is compared to the CFD model. Input excitation in the CFD model is low enough to avoid non-linear sloshing modes and other non-linear behaviour of the free-surface. The ComFLOW 2D CFD model has been validated against various works from the literature for the accurate representation of gap resonance frequencies.

For both the piston mode and sloshing resonance, discrepancies between the two numerical methods are found, which can be attributed to viscous effects. At resonance viscous effects are non-negligible, therefore the LPF method over-predicts the severity of the piston mode and sloshing. The influence of both the submergence of the monopile and its inclination angle with respect to the horizontal is considered.

The hydrodynamic coefficients for added mass and damping are found with forced oscillation for both upright and inclined geometries. While good agreement is found between the LPF and CFD results away from resonance, the CFD results in the vicinity of the resonance frequency are used to tune the LPF model, by way of additional linear damping, to achieve more accurate results.

It can be concluded from the present work that the resonance of the internal water column near the first sloshing mode significantly affects the overall hydrodynamic force and must be taken into account. At the peak hydrodynamic force observed during the first sloshing mode, the sloshing induces forces 5.59 times higher (submergence of 5 meters), 3.62 times higher (submergence of 10 meters), and 2.33 times higher (submergence of 15 meters) compared to cases where sloshing is not considered.

Looking forward, it is strongly advised to conduct forced oscillation tests with larger amplitudes, as this explores the effect of non-linear chaotic sloshing. Additionally, expanding the CFD analyses to 3D, where more non-linear sloshing effects are expected, such as swirling, is recommended. Furthermore, given the differences in results between LPF and CFD, it is valuable to validate the findings through model experiments.

Contents

Preface i

Abstract ii

Nomenclature v

Conventions vii

1 Introduction 1
1.1 Offshore wind industry . . . 1
1.2 The monopile foundation . . . 1
1.2.1 Standard installation method . . . 1

2 Research Motivation 3
2.1 Problem statement . . . 3
2.2 Literature review . . . 3
2.2.1 Vertical cylinder in waves . . . 3
2.2.2 First order potential flow . . . 4
2.2.3 Diffraction modelling for thin-walled structures . . . 4
2.2.4 Water behaviour inside MP . . . 5
2.2.5 Mechanical sloshing model . . . 6
2.2.6 Vessel Shielding . . . 7
2.2.7 Diffraction and CFD . . . 7

3 Research Objectives 9
3.1 Research objective . . . 9
3.2 Research questions . . . 9

4 Analytical description 10
4.1 Theoretical description . . . 10
4.2 Piston mode . . . 11
4.2.1 Two-dimensional . . . 11
4.2.2 Three-dimensional . . . 11
4.3 Sloshing mode . . . 15
4.3.1 Natural frequency of the sloshing liquid . . . 15
4.3.2 Two-dimensional . . . 15
4.3.3 Inclined sloshing frequency - 2D . . . 16
4.3.4 Three-dimensional . . . 16
4.3.5 Inclined sloshing frequency - 3D . . . 19

5 Linear potential flow 21
5.1 Diffraction modelling . . . 21
5.1.1 Governing equations . . . 21
5.1.2 Dipole panels . . . 22
5.2 Piston mode . . . 22
5.2.1 Dipole panels vs. conventional panels . . . 24
5.3 Sloshing . . . 25
5.3.1 Asymmetric sloshing mode . . . 25
5.3.2 Symmetric sloshing mode . . . 30
5.3.3 Damping lid . . . 31
5.3.4 Two-dimensional approach . . . 33
5.4 Focus on 10 meter submergence . . . 34
5.5 Inclined cylinder . . . 36

6 Computational fluid dynamics **38**
6.1 Governing equations . . . 38
6.1.1 One-phase flow model . . . 38
6.2 Numerical model . . . 40
6.2.1 Cell labelling . . . 40
6.2.2 Discretization and solution . . . 40
6.2.3 Initial settings . . . 41
6.3 Validation of the CFD code ComFLOW . . . 42
6.3.1 Phase difference . . . 44
6.3.2 Grid resolution . . . 44
6.3.3 Generating and absorbing boundary condition (GABC) . . . 45
6.4 Fixed geometry with regular incident waves . . . 46
6.4.1 Piston mode - 2D - Upright . . . 46
6.4.2 Piston mode - 2D - Inclined . . . 49
6.5 Geometry forced to oscillate in calm water . . . 50
6.5.1 Sloshing mode - 2D - Upright . . . 50
6.5.2 Determination of the hydrodynamic properties . . . 56
6.5.3 Sloshing mode - 2D - Inclined . . . 59

7 Results **61**
7.1 Validation of LPF using CFD . . . 61
7.1.1 Upright structure . . . 61
7.1.2 Inclined structure . . . 64
7.2 Modelling the sloshing resonance . . . 65
7.2.1 Damping lid for modelling purposes . . . 65
7.2.2 Hydrodynamic force ratio . . . 67

8 Experimental model tests **69**
8.1 Other model test in the research field . . . 69

9 Conclusions **70**
9.1 Determination of the resonance frequencies . . . 70
9.2 Accuracy of linear system description . . . 71
9.3 Effect of the resonance of the internal water column . . . 72
9.4 Primary research question . . . 72

10 Recommendations **73**
10.1 Resonance behaviour . . . 73
10.2 Monopile installation method . . . 73
10.3 Environmental conditions . . . 73
10.4 2D CFD . . . 73
10.5 3D CFD . . . 74
10.6 Experimental model tests . . . 74
10.7 Mechanical sloshing model . . . 74

A Appendix A: Grid resolution **79**
A.1 Gap resonance . . . 80
A.2 Piston mode . . . 81
A.3 Sloshing mode . . . 82

B Appendix B: Potential theory (OrcaWave) **83**
B.1 Governing equations . . . 84
B.1.1 First-order equations . . . 84
B.1.2 Boundary value problems . . . 84
B.1.3 The potential formulation . . . 84

C Appendix C: Analytical forced oscillation description for a 3D cylinder **86**
C.1 Fundamental sloshing mode . . . 87

D Appendix D: Analysis of 2D forced oscillation results **88**

Nomenclature

Abbreviations

Abbreviation	Definition
BiCGSTAB	Bi-conjugate gradient stabilized method
CFD	Computational fluid dynamics
CFL	Courant-Friedrichs-Lewy condition
CM	Center of Mass
DOF	Degree of freedom
GABC	Generating and absorbing boundary condition
ILU	Incomplete lower-upper preconditioner
ISA	International standard atmosphere
LPF	Linear potential flow
MP	Monopile
OWF	Offshore wind farm
OWT	Offshore wind turbine
RAO	Response amplitude operator

Latin Symbols

Symbol	Definition	Unit
A_w	wave amplitude	[m]
D_i	inner diameter	[m]
D_o	outer diameter	[m]
g	gravitational acceleration [=9.81]	[m/s^2]
h	submergence	[m]
H	wave height	[m]
$J_\alpha(.)$	the Bessel function of the first kind [α is a real non-negative number]	
k	wave number	
R	radius of a circular cylindrical tank or a circular spherical tank [=$\frac{1}{2}D$]	[m]
t	time	[s]
T	period	[s]
V	velocity	[m/s]

Greek Symbols

Symbol	Definition	Unit
α	used for definition of different angles	
ϵ	damping parameter	
η	fluid surface elevation	[m]
η_i	translatory ($i = 1, 2, 3$) and angular ($i = 4, 5, 6$) components of motion	
$\iota_{m,i}$	roots of the equation $J'_m(\iota_{m,i}) = 0$	

Symbol	Definition	Unit
κ	moonpool geometry factor	
λ	wavelength	[m]
Λ	dimensionless excitation frequency	
ω	angular frequency	[rad/s]
Ω	excitation frequency	[rad/s]
ρ	density	[kg/m^3]
σ	surface tension	[N/m]
Φ	velocity potential	

Conventions

Coordinate system

In this section the coordinate system conventions for a vessel and cylinder are given.

Coordinate	Origin at	Positive direction
X	aft perpendicular (APP) or base of the cylinder	towards bow
Y	centre line (CL) or base of the cylinder	towards port side (PS)
Z	baseline (or keel (BL) or base of the cylinder	upwards

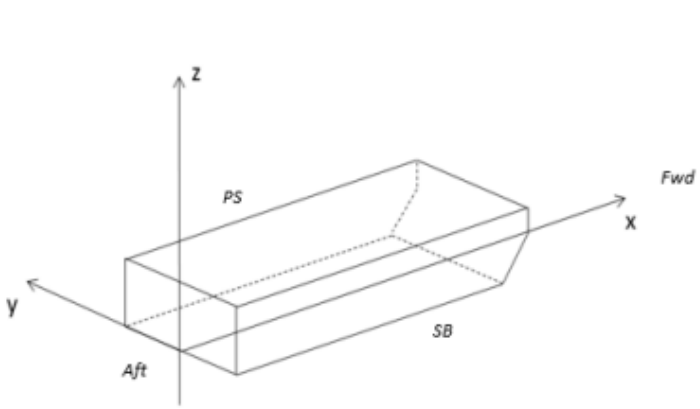

(a) Coordinate system vessel. [28]

(b) Coordinate system cylinder [20].

Figure 1: Schematic representation of coordinate system conventions.

Motions

In this section the motion conventions are given.

Motion	Description	Positive direction
surge (η_1)	motion in x-direction	towards bow
sway (η_2)	motion in y-direction	to port side (PS)
heave (η_3)	motion in z-direction	upwards
roll (η_4)	rotation around axis parallel to x-axis	starboard (SB) down
pitch (η_5)	rotation around axis parallel to y-axis	bow down
yaw (η_6)	rotation around axis parallel to z-axis	bow to port side

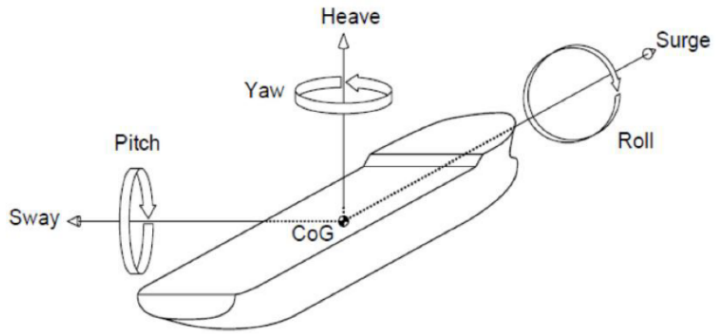

Figure 2: Schematic representation of (vessel) motion conventions with respect to center of gravity [20].

Wave heading

In this section the wave heading convention is given. This convention is similar for current and wind.

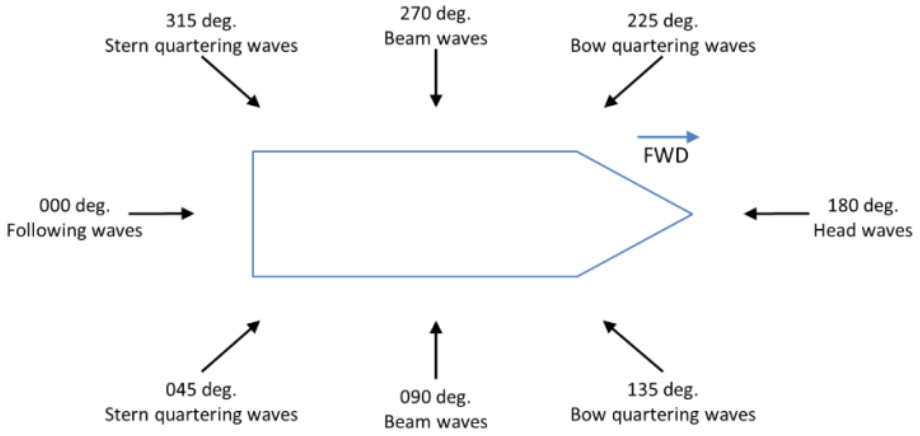

Figure 3: Wave heading convention with respect to vessel. [28]

1 Introduction

This chapter provides the necessary background information on the thesis subject, which helps readers understand why the graduation topic is relevant. It gives readers a foundation of knowledge to better comprehend the main theme of the thesis.

1.1. Offshore wind industry

The offshore wind industry is a continuously growing market. In this market, it is important to extract the maximum possible efficiency from an offshore wind farm (OWF). In recent years there has been an urge to place OWFs further and further from the coast. There are multiple factors that explain this trend. Firstly, stronger and more consistent winds at greater distances from shore allow an offshore wind turbine (OWT) to generate more electricity. Secondly, installing OWFs further out at sea can reduce the impact of visual and noise pollution on coastal communities. Thirdly, suitable sites for wind farms are becoming increasingly scarce closer to shore, prompting developers to look to deeper waters further out at sea. Additionally, advances in turbine technology have resulted in the production of larger and more powerful turbines, which require more space and are better suited to installation further out at sea. Finally, the cost of building and operating OWFs has decreased significantly in recent years, making it more economically feasible to install turbines further out at sea.

A challenge of building OWFs further out at sea is the increase of seabed depth to which the foundations have to be fixed. In general there are two categories of OWT foundations, bottom-fixed and floating. Among the bottom-fixed foundations, the monopile is the simplest in terms of production and installation. Other options are the jacket or the gravity based foundation [24]. Floating OWT rely on mooring and anchoring systems for their station keeping. Examples of floating foundations are the spar, the semi-submersible platform and the tension leg platform [24].

1.2. The monopile foundation

The focus of this study is exclusively on monopile foundations. From this point onward, a monopile (MP) will be indicated as MP. A MP is a thin-walled, hollow steel cylinder that are installed in the seabed by means of a powerful hydraulic hammer [44] or a vibratory hammer [10]. At present, MPs are the prevailing foundation type for supporting OWTs, accounting for about 80% of such installations [21]. The main reason for MPs to be the preferred option, is the simplicity in design, fabrication and installation processes. MPs are typically used in hard to semi-hard seabed conditions [24]. Typically a MP is around 5 meter in diameter and has a slenderness ratio (length/radius) of 10 to 12, which makes them suitable for shallow to moderate water depths of 35 meter [21]. However, since the OWF will be in increasingly deeper waters, the MP size will increase as well. Such large MPs are referred to as XL, for diameters up to 10 meters, and XXL, for diameters larger than 10 meters.

1.2.1. Standard installation method

For the installation of MP foundations, either a jack-up vessel or a floating heavy lifting vessel is used. The MP foundations can be transported to the site either on a barge (feedering) or on the installation

vessel (shuttling), depending on the specifications of the installation vessel. For most projects shuttling is the most economic way of transportation. However, when the project site is very far from the shuttling port, feedering might be the preferred option [27]. Also for projects in the United States, carried out by foreign installation vessels, feedering is used because of the Jones act [61].

The primary benefit of utilizing a jack-up is its ability to offer a secure and steady platform for installation purposes. However, the installation and retrieval of the jack-up legs can be time-consuming and must be conducted during favourable weather conditions [56]. Compared to jack-up vessels, floating heavy lifting vessels are more versatile for offshore operations and are proficient in executing mass installations of wind farms because they allow for swift transit between foundations [39]. Heavy lifting vessels use dynamic positioning systems for station-keeping. Nonetheless, the installation of foundations using a floating vessel is more susceptible to weather conditions due to the heave, pitch, and roll motions of the vessel, unlike the stable jack-up platform.

The widely used installation method in the industry consists of four steps. First the MP is upended from a horizontal to a vertical position, from the transportation barge or on the installation vessel, using an upending frame. Then the crane brings the MP into position besides the ship, where a pile-handling tool, such as a gripper device, is used to hold the MP in vertical position. The MP is lowered until it stands on the seabed and driven into the seabed by a hydraulic hammer. When the MP is in place, the transition piece can be placed on top. Nowadays, also MP foundations without transition pieces are used, and this last step is skipped [24].

2

Research Motivation

This chapter provides the problem statement and a literature review.

2.1. Problem statement

The main focus of this study is the upending phase of a MP installation procedure, in which a MP is upended from a horizontal to a vertical position, partly through the wave zone. In this phase, the hydrodynamic loads will influence the motions of the MP. While the hydrodynamic loading on the MP structure may not be a critical concern for the MP itself, it will create dynamic loading on the cranes. Therefore, an accurate estimation of these loads is necessary. In other words, to determine the hydrodynamic behaviour of the MP will increase the accuracy of workability predictions.

In the context of XXL MP installation, there are distinctive aspects that necessitate thorough investigation to be able to comprehend the hydrodynamic behaviour. Firstly, the Morison equation, a conventional tool for such analysis, is not appropriate due to the significant diameter of XXL MPs. Consequently, a more suitable description of MP behavior using potential flow theory is used. Secondly, the open-ended configuration of the MP on both sides introduces complexities involving internal water dynamics and flow separation at the bottom edge.

Among these complexities, the internal water behavior presents the most substantial source of uncertainty in understanding MP hydrodynamics. Especially resonance effects of the internal water column are relevant, since these can be significant and possibly critical for the operation. Moreover, frequencies near the resonance frequency may commonly appear in the wave spectrum at the operational location.

Furthermore, unlike conventional installation methods, due to the adoption of the ”tandem lifting” procedure, XXL MPS are subjected to inclined splash-zone entry instead of solely vertical lowering. The effect of the inclination on the internal water behaviour should be investigated.

2.2. Literature review

2.2.1. Vertical cylinder in waves

The force model on a vertical MP is described by Lin Li et al. [38], using Morison equation [52] for the horizontal wave force. Strip theory is employed in this model to calculate excitation forces based on the slender body assumption. According to Faltinsen and Timokha [17], the primary assumption of the Morison equation is that the diffraction potential remains constant across the entire body. Because of this assumption, the Morison equation is only applicable if the diameter of the cylinder is small with regards to the wavelength. If this is not the case, diffraction effects have to be taken into account [59]. For the large diameter XXL MPs this implies that diffraction has to be considered for smaller wave periods. Another disadvantage of the standard Morison equation only applies to vertical cylindrical structures, which is not constantly the case during upending [41].

Another technique to model the hydrodynamic loads is potential flow theory. It evaluates pressure integrals around the surface of a body and is suitable for situations where the floating body is significantly larger than the wavelength of the incident sea state. It accurately accounts for wave excitation

forces, diffraction, radiation loads, added mass, and damping caused by the presence of the submerged structure. However, this theory does not account for viscous drag loading.

To analyse the dynamic response during the installation of large diameter MPs, it is relevant to look at research for large diameter cylindrical floating structures such as semi-submersible wind turbine foundations. To simulate the dynamic response of such a structure Kvittem et al. [35] combines the use of potential flow theory, which accounts for radiation and diffraction effects, with Morison's equation which accounts for viscous effects. Other examples of closed vertical cylinders subjected to external water flow are spar buoy ([75],[34]) and the tension leg platform (TLP) [53].

2.2.2. First order potential flow

The MP upending operation from a horizontal to a vertical position alongside the ship takes approximately 20 minutes [27]. This is relatively long compared to the expected wave periods, and therefore it can be considered a stationary operation. The potential flow theory assumes inviscid, incompressible and irrotational flow [16]. Also, no transient effects are present due to the steady state conditions [16]. A disadvantage of potential flow theory is that viscous effects are not taken into account. Viscous effects might be important for the overall behaviour of the MP, considering the water behaviour inside the MP (2.2.4).

If the viscous effects are not considered, the hydrodynamic problem in regular waves can be divided in two components [16]. Steady-state condition is assumed, so no transient effects are present due to initialconditions. This condition implies that the linear dynamic motions and loads acting on the structure are harmonically oscillating with the same frequency as the wave-induced loads that excite the structure. Due to linearity these two components can be added to give the total hydrodynamic loading. The two components are [17]:

1. The forces and moments acting on the structure when the body is restrained from oscillating and incident regular waves are present. The hydrodynamic loads consist of the Froude-Kriloff loads and the diffraction forces and moments, collectively referred to as *wave excitation loads*. The Froude-Kriloff forces arise from the pressure field within the incident waves, which are undisturbed by the structure. Newman [54] refers to what we call the diffraction problem as the scattering problem. Newman [54] refers to what is known as the *diffraction problem* as the scattering problem. In his terminology, the diffraction loads encompass the combined effects of the Froude-Kriloff and scattering loads.
2. The forces and moments acting on the body when the structure is forced to oscillate in undisturbed water at the wave excitation frequency corresponding to any rigid-body motion mode. There are no incident waves present, but the oscillations of the body lead to the generation of radiating waves. The hydrodynamic loads are identified as *added mass*, *damping* and *restoring* forces and moments. This subproblem is known as the *radiation problem*.

It is important to emphasize that in a nonlinear theory, the diffraction and radiation problem cannot be separated.

2.2.3. Diffraction modelling for thin-walled structures

There are multiple numerical modelling programs that determine the linear hydrodynamic loads and as such assess the performance of offshore structures. Currently, the boundary element method (BEM) based on the potential flow theory remains a prevalent technique for evaluating a wide range of selective sea states, despite the high accuracy of computational fluid dynamics (CFD) based on Navier-Stokes (N-S) equations. This is mainly due to BEM's lower computational cost, which has made it an essential tool in the field. Generating appropriate panels for simulation in BEM analyses for thin structures, like the thin-walled XXL MP, can be challenging [65]. Consequently, numerical modeling of structures with thin components may require a considerable number of panels to achieve accurate results.

Research by Sheng et al. [65] concluded that open source software HAMS [41] could handle thin structures as accurately as commercial code WAMIT [36]. Other radiation-diffraction analyses software packages are ANSYS-AQWA and NEMOH. Sheng et al. [65] found that NEMOH could not predict the hydrodynamic parameters correctly for a thin walled structure.

In the graduation thesis of Van Steensel [69] the hydrodynamic diffraction of a hollow cylinder was modelled with ANSYS-AQWA. The results for radiation damping, added mass and wave loads per frequency excitation were than used in Orcaflex models to compare with the results for model experiments.

An interesting take away from this research regarding ANSYS-AQWA is that unwillingly a standing wave was generated inside the cylinder because of the water oscillation. The model does not account for viscous effects, which would partly damp out oscillations in real-world scenarios, leading to unrealistically high surface elevations. This could be fixed with a numerical trick. By implementing an abstract (not physical) lid inside the cylinder, which suppresses the vertical velocity. However, the amount of viscous damping this internal lid should represent is an approximation.

Regardless of the approach used for numerical modeling of the MP behavior, it is imperative to acquire experimental results to procure model-scale data that can be utilized for the purpose of validation and calibration of the integrated numerical model.

2.2.4. Water behaviour inside MP

The water behaviour inside the MP can best be compared with the water behaviour inside a partially filled circular tank. Ibrahim described liquid sloshing in the book ”Liquid sloshing dynamics” [22]. Liquid sloshing refers to any motion of a liquid’s free surface inside its container. A phenomenon caused by disturbance to partially filled containers. Depending on the shape of the container and the type of disturbance, the liquid surface experiences various types of motion. These include simple planar motion, nonplanar motion, rotational patterns, irregular beating, symmetric and asymmetric motion, quasi-periodic oscillations, as well as chaotic behaviour.

First the focus will be on the linear sloshing that can be expected. During the upending operation the MP will be open-ended on both sides. The water that will flow inside the MP during this operation will be in contact with the water surrounding the MP. It is expected that this water motion might show resonance at certain oscillatory frequencies. The natural mode at which the water is forced to oscillate up and down, in a heaving motion, is referred to as the piston-mode. The natural modes at which water is oscillation back and forth are refered to as the sloshing modes. Both modes are described by Molin [48] for moonpools (Figure 2.1). Moonpools are vertical openings in a vessel’s deck and hull, which are utilized for various maritime and offshore activities. For moonpools the natural modes are caused by the water motion that is influenced by wave-induced pressures and the motion of the vessel. Molin [48] showed that as the width and draught of the moonpool decrease, there is a corresponding rise in the frequency of the longitudinal sloshing modes.

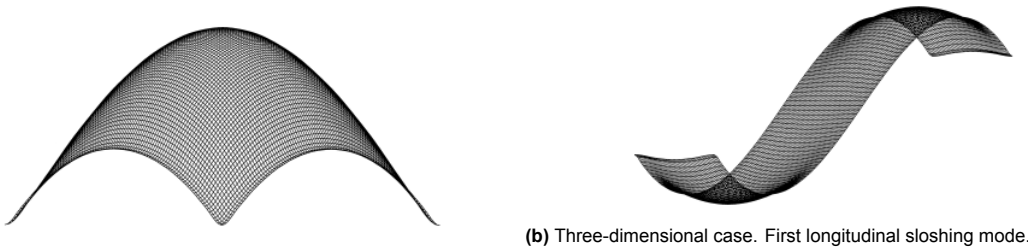

(a) Three-dimensional case. Piston mode. Square moonpool.

(b) Three-dimensional case. First longitudinal sloshing mode. Elongated moonpool.

Figure 2.1: Piston mode and sloshing mode as presented by Molin [48].

The effect of the resonance modes is that the water inside behaves more or less like a rigid body possible leading to significant loads. As the size of the MP increases, so does the volume of water, which can be a significant concern. Additional research is required to determine the impact of both the piston- and sloshing-modes on the behavior of the open-ended inclined XXL MP, as well as to assess the extent to which the internal water resonance-induced loads affect the overall motion of the MP.

The application of an open-ended vertical cylinder subjected to external water flow can be found in the oscillating water column (OWC) device, which converts wave energy to electricity [72]. Multiple OWC device concept are possible, but the one relevant for this research consists of a truncated, vertical, hollow cylinder which is partially submerged and open at the bottom. At the top, above the water, there is a turbine which generates energy from the air pressure that is created by passing waves. In the study by Wang and Falzarano [72] an analytical model has resolved the diffraction and radiation challenges associated with a floating vertical Oscillating Water Column (OWC) device by incorporating first-order wave forces and hydrodynamic properties. This model has similarities to a partially suspended cylinder in water subjected to waves.

A significant observation gathered during the monopile model tests conducted by Van Oord at SIN-

TEF [29] is the resonant sloshing behavior of the internal water column during the forced motion tests. During forced motion tests conducted with water inside the monopile, the occurrence of resonant sloshing is contingent upon several factors, including the water level, angle of inclination, motion frequency, and mode. The presence of significant sloshing amplitudes leads to non-linear free surface effects, which pose challenges in both the development of numerical or empirical simulation models and real-world upending operations. Liquid oscillations resulting from resonant sloshing can induce undesired movements of the monopile, complicating operational control. An example of an instance where sloshing is observed is given in Figure 2.2 from the SINTEF [29] model test campaign. Figure 2.2 shows snapshots of the free surface phenomena occurring during a specific test. In Figure 2.2, a 45 degrees inclination angle, an enforced horizontal motion of amplitude 1.5 meter, with a period of 6 seconds was present. In this test, a bottom plug was present, which is not the case in the desired installation sequence in the present work. In this specific test, the flow rapidly becomes violent, characterized by impinging jet flows that culminated in swirling sloshing patterns.

The swirling or rotary flow motions that are indicated in Figure 2.2 are described by Faltinsen and Timokha [17]. The direction of forced motion which is applied to the structure is also indicated in Figure 2.2. Swirling occurs during horizontal excitation when the forcing frequency is near the lowest natural frequency. A consequence of swirling is a lateral hydrodynamic force component that is perpendicular to the forced oscillation direction. To get a sense of swirling, it is possible to move a glass of water back and forth. It's worth noting that the rotation direction depends on transient conditions, and steady-state swirling motion can be either clockwise or counterclockwise. Additionally, swirling may change its rotation direction during transient conditions. Swirling is a nonlinear phenomenon.

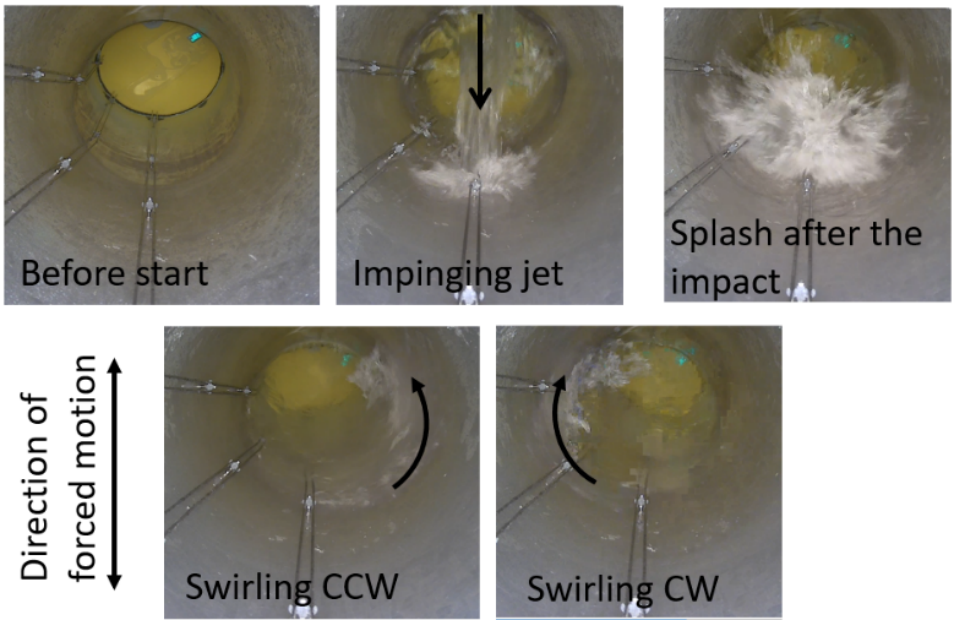

Figure 2.2: Violent sloshing accompanied with jet flows that subsequently transition into swirling or rotary flow patterns, oscillating back and forth. This dynamic behavior occurs under a 45-degree inclination, with water present inside the structure and the bottom plugin place. The horizontal amplitude of the imposed motion is 1.5 meters, and the period of forced motion is 6 seconds. [29]

2.2.5. Mechanical sloshing model

In the work by Sharma et al. [64], a mechanical model is proposed for predicting the highest amplitude of sloshing waves inside a cylindrical tank. The model is based on earlier work by Abrahamson et al. for linear fluid sloshing, Abrahamson et al. represented the lateral sloshing problem using spring-mass-damper systems [2] and pendulum based models [1]. The work by Abramson was mostly conducted to predict the dynamic behaviour of liquids in moving (cylindrical) tanks in the space craft technology. The model by Sharma et al. [64] consists of a linear, two degrees of freedom, spring-mass-damper system which contains two masses representing a sloshing mass and a non-sloshing mass of the partially filled cylindrical tank. A representation of the model is given in Figure 2.3. Through experimental

tests, the model has been validated, demonstrating its ability to provide an accurate representation of water sloshing within a laterally excited cylindrical tank. The model's accuracy and applicability can be further improved by incorporating additional modal masses, introducing non-linear and torsional springs to account for non-linear effects, and addressing the rotational dynamics of the free surface, especially near resonant frequencies. In the present work, the effect of the open bottom of the cylinder on the sloshing should be taken into account. Also the inclination of the cylinder and the effect it has on the motion of the internal water column is not considered by this model.

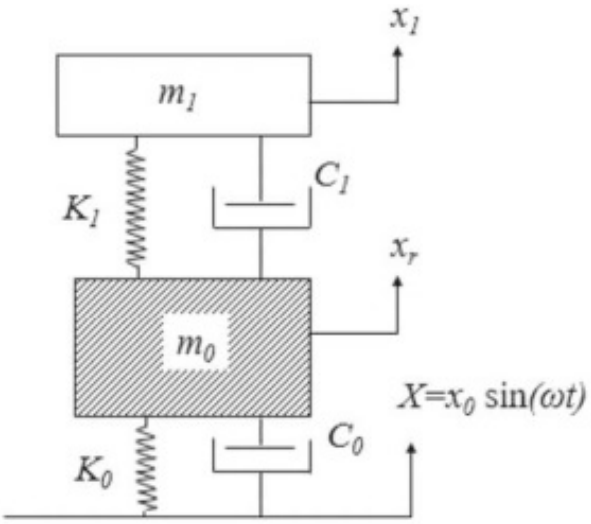

Figure 2.3: Proposed two DOF spring-mass-damper model for lateral sloshing [64].

2.2.6. Vessel Shielding

The wave spectrum that acts on the MP is influenced by the presence of the heavy lifting vessel (HLV). The diffraction and shielding effect from the vessel is studied by L. Li et al. [40]. The study focuses on the process of lowering the MP vertically alongside the vessel, in a conventional crane-gripper configuration. Thus it can be considered a multi-body system where the bodies (vessel and MP) are connected through the lift wire and the gripper, in which the lift wire controls the lowering of the MP and the gripper the horizontal motions of the MP. The study concludes that the motions of the MP in relatively short waves (Tp = 5 and 7 s) are significantly reduced when the MP is lowered on the leeward side of the vessel, compared to the same operation on the windward side of the vessel. The shielding effect decreases as the wave period increases, which can be explained through diffraction theory. Short waves are subject to diffraction by the vessel, whereas long waves are not. When it is decided to use a floating HLV in long waves (Tp > 11s) it is suggested to carry the operation out in head seas or following seas to avoid large roll motions of the vessel. These roll motions will significantly increase the gripper contact forces on the MP [40]. In the current study, we exclusively focus on the monopile, disregarding the presence of the vessel. It is advisable to incorporate the vessel and connecting cranes in future research to analyze the impact of multibody dynamics.

2.2.7. Diffraction and CFD

The internal water motion in an open ended monopile during the installation can have a significant effect. Specifically the effect of sloshing motions of the surface water level, near the natural sloshing modes, can have a pronounced effect on the monopile motions. Bunnik and Veldman [8] present two different models that take into account the effect of sloshing on ship motions. In the first model a linear diffraction method in the frequency domain is used for both the liquid motions in the containment system and the liquid motions outside the vessel. In the second model, a time-domain coupling technique where the computation of the sloshing liquid within the containment system is performed using computational fluid dynamics (CFD) utilizing the Volume of Fluid method. Meanwhile, the hydrodynamics of the ship are calculated using the linear diffraction method.

Both methods are employed to simulate model tests described by Molin [49], where the motion response of a barge with a water container partially filled on its deck was measured. The focus of the research is on the roll motion response in beam seas. Validating the models with these model tests show:

- The diffraction model produces a roll response (RAOs) that is reasonably consistent with the experimental results. However, there is a slight shift in the position of the 2^{nd} sloshing-induced peak, and the peak itself is narrower compared to the experiments. In order to achieve accurate added mass values and an appropriate roll response, it is necessary to introduce additional dissipation on the free surface of the tank.
- The coupled CFD-diffraction model exhibits excellent agreement with the experimental data. A study on grid refinement demonstrates that even with relatively coarse grids, satisfactory results can still be achieved.
- In more severe sea conditions, the second peak in the roll response noticeably decreases. This behavior is accurately predicted by the coupled CFD-diffraction model, although it slightly overestimates the actual response.

Although the coupled CFD-diffraction model yields favorable outcomes in the context of this specific large free-surface tank application, it is important to acknowledge its inherent limitations. An important limitation in the context of the current research is that viscous effects are not resolved due to the use of coarse grids without any resolution in boundary layers. As a result, when viscous effects become significant, refined boundary layers and turbulence models should be employed. The CFD model used by Bunnik and Veldman [8], did not allow such capabilities, but the newer version of ComFLOW (from ComFLOW 3 onward) does.
Furthermore, Bunnik and Veldman [8] only focused on beam seas. Wave directions other than beam seas have the potential to induce longitudinal tank sloshing and impact surge motions. The method presented in this paper can, in theory, handle such wave directions. However, it should be noted that incorporating non-beam seas would significantly increase the required CPU time, as sloshing would transition from a 2D effect to a 3D effect in those cases.

3

Research Objectives

In this chapter the research objectives, research questions and plan of approach will be given.

3.1. Research objective

The main objective of this research is develop a method that sufficiently conservatively predicts the effect of internal fluid motions on the overall hydrodynamic behaviour of a large-diameter, thin-walled, open-ended monopile as it is upended from a horizontal to vertical position in the splash zone.
To meet the main objective, multiple sub-objectives are formulated:

1. Analyze the internal water motions and loads resulting from fluid resonance in an open-ended cylinder, including piston-mode resonance and sloshing.
2. Investigate how the inclination angle of the monopile relative to the horizontal position during the upending operation affects these phenomena.
3. Investigate whether the resonance frequencies of the internal water column are within the expected range of frequencies occuring during the operation.
4. Develop a method to determine the hydrodynamic loads from internal sloshing on an upright and inclined cylinder during the complete upending cycle.
5. Examine the difference in hydrodynamic loads between the conventional method and the method that incorporates internal water effects.
6. Validate the computational model based on LPF with a CFD model.

3.2. Research questions

Primary research question

Is it possible to predict the internal water behavior, particularly resonance motions, in an open-ended monopile during the installation sequence, and what is the impact of this behavior on the overall motions of the monopile?

Secondary research questions

- Can an analytical equation be employed to determine the frequencies of the piston mode and sloshing mode within the internal water column of both vertical and inclined monopiles?
- Is it possible to describe the internal water behavior in an open-ended monopile accurately with linear theory, or is it necessary to take non-linearities into account?
- Is it feasible to formulate a precise method for translating the motions of the internal water column into forces acting upon the monopile?

4

Analytical description

In this chapter, analytical descriptions for the relevant phenomena will be treated. Two types of resonant motion are treated, known as the piston and sloshing modes. Both resonant modes will be initially examined in two dimensions and subsequently in three dimensions. The analytical derivations provided for the resonant modes will be utilized throughout the remainder of the report.

4.1. Theoretical description

The following theoretical description is grounded in several studies and expounded upon in the work of Faltinsen and Timokha [17]. In the frequency domain, the equations of rigid-body motions are represented by equation 4.1. As only the monopile is taken into account, the equations describing its motion involve six degrees of freedom (DOFs). In equation 4.1 only the equations of linear and angular momentum are used. The effect of sloshing is not yet incorporated in the equations of motion. Thus the considered hydrodynamic flow in these equations of motion are exterior to the structure.

$$\sum_{k=1}^{6}[(M_{jk}+A_{jk})\ddot{\eta}_k + B_{jk}\dot{\eta}_k + C_{jk}\eta_k] = F_j e^{i\sigma_e t} \qquad (j=1,...,6) \tag{4.1}$$

In equation 4.1, M_{jk} is the generalized mass matrix, A_{jk} is the hydrodynamic added mass matrix, B_{jk} is hydrodynamic damping matrix and C_{jk} is the restoring matrix. Furthermore, F_j are the complex amplitudes of the exciting force and moment components. The subscripts in, for example, $A_{jk}\ddot{\eta}_k$ refer to the force (or moment) component in the j-direction because of motion in the k-direction.

Because added mass and damping are frequency dependent, the equations of motion provided in equation 4.1 cannot be employed directly in the time domain. Nonetheless, if the steady-state solution is of interest, this issue can be bypassed by combining the responses to components of regular waves. If however a transient response is needed, for example the coupling between nonlinear sloshing in a ship tank and ship motion, the equations of motion are given as equation 4.2.

$$\begin{aligned}\sum_{k=1}^{6}\{[M_{jk}+A_{jk}(\infty)]\ddot{\eta}_k(t) + B_{jk}(\infty)\dot{\eta}_k(t) + \int_0^t h_{jk}(\tau)\dot{\eta}_k(t-\tau)d\tau + C_{jk}\eta_k\} = \\ F_j^{ext}(t) + F_j^{tank}[\eta_k(t)] \qquad (j=1,...,6)\end{aligned} \tag{4.2}$$

In equation 4.2, F_j^{ext} represents the linear external wave force and moment components. Furthermore, F_j^{tank} are the force and moment components associated with sloshing and are functions of $\eta_k(t)$ and the second time derivative of $\eta_k(t)$. The integrals in equation 4.2 are referred to as the convolution integrals or as Duhamel integrals. In these integrals $h_{jk}(t)$ are the retardation functions, which evaluation requires information on the behavior of either A_{jk} or B_{jk} at all frequencies. The structure terms M_{jk} and C_{jk} are the same as in equation 4.1. $A_{jk}(\infty)$ and $B_{jk}(\infty)$ mean infinite frequency added mass and damping coefficients.

The focus is now shifted from coupled ship motions and sloshing to coupled sway (could also be surge) motions and sloshing. The equations representing the steady-state response in the sway direction can be approximated as in equation 4.4.

$$[M + A_{22}(\sigma)]\ddot{\eta}_2 + B_{22}(\sigma)\dot{\eta}_2 = F_2^{exc} + F_2^{tank} \tag{4.3}$$

In equation 4.4, M is the mass of the structure, not including the mass of the liquid inside the tank. $A_{22}(\sigma)$ and $B_{22}(\sigma)$ are the linear sway added mass and damping associated with the external flow, respectively. These are a function of σ, the frequency of oscillation. F_2^{exc} is the external linear sway excitation force and F_2^{tank} is the sway force caused by the sloshing in the tank and can be expressed as equation 4.4.

$$F_2^{tank} = -C_{22}^{tank}(\sigma, \eta_2)\eta_2 \tag{4.4}$$

4.2. Piston mode

Given that the base of the monopile is open at the bottom, the water contained within it remains in direct connection with the encompassing water. The fluid can undergo a vertical movement in a uniform manner with an oscillating motion and a flat free surface as a result of an oscillatory force, such as waves.

4.2.1. Two-dimensional

Extensive research has been conducted on the piston-mode resonance between two ships, a moonpool, or between a ship and the quayside. The situation that can best be compared to that of a partly submerged vertical monopile is the moonpool. Molin [48] describes an approximation for the piston mode inside a moonpool. The approximation assumes the water inside the moonpool to be a solid body. Molin's formula was initially devised to estimate piston-mode resonance frequency occurring within a two-dimensional moonpool situated between two hulls. However, it also provides accurate approximations for three-dimensional cylindrical situations, as demonstrated in the research by [25]. Molin's formula with the relevant variables for the monopile is provided in equation 4.5.

$$\omega_{piston} = \sqrt{\frac{g}{h(1 + D_i(1.5 + \ln(D_o/2D_i))/\pi h)}} \tag{4.5}$$

In equation 4.5, h is the submergence of the monopile, D_i the inner diameter of the monopile and D_o the outer diameter of the monopile. Equation 4.5 is valid for deep water and it assumes a rigid boundary condition at $z = -h$ for all x and y coordinates, except at the moonpool opening. This assumption is necessary to obtain a closed semi-analytical solution. In other words, the accuracy of the estimate improves when the horizontal dimensions of the surrounding geometry are significantly larger than those of the moonpool [12]. It should therefore be evaluated whether equation 4.5 is valid for an upright monopile, which can be considered as a thin-walled moonpool. This reasoning is necessary for both the 2D and 3D piston-mode resonance frequency approximations by Molin.

4.2.2. Three-dimensional

For the three-dimensional piston mode, three different methods for finding the resonance frequency are introduced. First a function by Molin following from the function for two-dimensional piston mode is introduced, then Fukuda's formula is given. Both these methods are developed for a moonpool. Lastly, the upright cylinder is considered as a mass-spring system, and an approximation by Falnes [15] is used to find the natural frequency.

In case of a three-dimensional rectangular moonpool, Molin [48] also gives an approximate formula for the piston-mode resonance frequency. The formula, 4.6, considers a moonpool of length L, breadth b and submergence (or draught) of h.

$$\omega_{piston} = \sqrt{\frac{g}{h + bf_3(b/L)}} \tag{4.6}$$

where

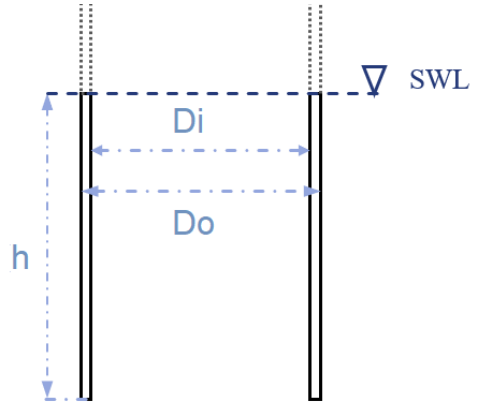

Figure 4.1: Parameters for Molin's two dimensional analytical piston mode determination for a partly submerged vertical cylinder. *(this figure is not to scale)*

$$f_3 = \frac{1}{\pi}\left\{\sinh^{-1}\left(\frac{L}{b}\right) + \frac{L}{b}\sinh^{-1}\left(\frac{b}{L}\right) + \frac{1}{3}\left(\frac{b}{L} + \frac{L^2}{b^2}\right) - \frac{1}{3}\left(1 + \frac{L^2}{b^2}\right)\sqrt{\frac{b^2}{L^2} + 1}\right\} \tag{4.7}$$

Equations 4.6 and 4.7 follows by generalizing the procedure for a two-dimensional moonpool. This procedure is expained by Faltinsen and Timokha [17].

Another method to calculate the wave frequency corresponding to the infrequency of the vertical oscillating water column in a three-dimensional moonpool (piston mode) is using Fukuda's formula [71]. This method is described by DNV [13] and employed by the diffraction software AQWA. Fukuda's formula is presented in equation 4.8.

$$\omega_{piston} = \frac{2\pi}{T_{piston}} = \sqrt{\frac{g}{h + \kappa\sqrt{A}}} \tag{4.8}$$

In equation 4.8, A is the cross sectional area of the internal surface area, h is the submergence and κ is a shape dependent constant. The value of κ = $8/(3\pi^{3/2}) = 0.479$ for a circular area, 0.460 for a rectangular area (b/l=0.5) and 0.473 for a square area. The coefficient of could be related to the added mass at the lower surface of the moonpool. [71]

Piston mode natural frequency for an upright cylinder

First, the natural frequency of the piston mode will be determined for an upright cylinder. The system can be considered a mass-spring system, thus the linear equation of motion in heave direction is given by:

$$(m + a_{33})\ddot{\eta_3} + b_{33}\dot{\eta_3} + c_{33}\eta_3 = F_{ex3} \tag{4.9}$$

in which m and a_{33} are mass and added mass respectively, b is the linearized damping, C is the stiffness, F is the excitation force and η_3 is the heave motion of the water.

The mass, M, is equal to the volume of the water column times the water density:

$$m = A_{wl}\rho_w h, \qquad A_{wl} = \frac{\pi}{4}D_i^2 \tag{4.10}$$

In this equation A_{wl} is the water plane area inside the cylinder, ρ_w is the water density, h is the submerged length and D_i is the inner diameter. See Figure 4.2.

The stiffness, c_{33}, is given by:

$$c_{33} = A_{wl}\rho_w g \tag{4.11}$$

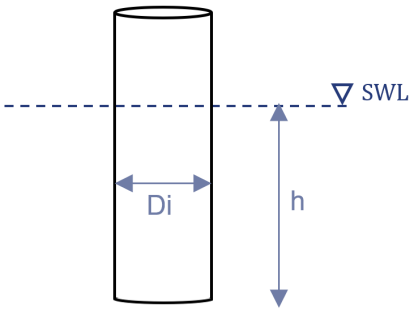

Figure 4.2: Upright cylinder. *(this figure is not to scale)*

The equation of motion can be solved to find the natural frequency by assuming harmonic motion: $\eta = \eta_a e^{iwt}$. Considering equation 4.9, 4.10 and 4.11 the homogeneous equation of motion in heave direction becomes:

$$-\omega^2(A_{wl}\rho_w h + a_{33}(\omega)) + i\omega b_{33}(\omega) + A_{wl}\rho_w g = 0 \tag{4.12}$$

This analytical analysis does not consider damping. In reality, both linear radiation damping, and nonlinear viscous damping might influence the natural frequency of the system. The undamped natural frequency for the piston body is given by:

$$\omega_n = \sqrt{\frac{c_{33}}{m + a_{33}(\omega)}} = \sqrt{\frac{A_{wl}\rho_w g}{A_{wl}\rho_w h + a_{33}(\omega)}} \tag{4.13}$$

The water present below the water column is likely to move with the water within the cylinder, resulting in an "added mass" that reduces the frequency. According to Kristiansen [32], it is clear that the natural frequencies decrease in proportion to the square root of the submerged length of the cylinder. The magnitude of the added mass varies in the context of gap resonance problems, introducing an element of uncertainty ([32]). It is expected that the added mass depends on several geometric parameters, including cylinder thickness, length, and diameter. Additionally, the added mass is highly dependent on the wave frequency, with the expectation that it increases significantly near resonance, in contrast to its behavior at relatively low or very high frequencies. To estimate the added mass, Falnes [15] introduced a correction to account for the added mass of the oscillating water column. Falnes [15] estimates the added mass at ω_n as:

$$a_{33} = 0.76\frac{2\pi}{3}R^3\rho_w \tag{4.14}$$

In this approximation R is the inner radius of the cylinder, and thus half of the inner diameter (=$\frac{1}{2}D_i$). Implementing this into the equation of the natural frequency gives:

$$\omega_{piston} = \sqrt{\frac{A_{wl}\rho_w g}{A_{wl}\rho_w h + 0.76\frac{2\pi}{3}R^3\rho_w}} \approx \sqrt{\frac{g}{h + 0.5R}} \tag{4.15}$$

Piston mode natural frequency for an inclined cylinder

For an inclined cylinder, linear equation of motion in body fixed heave direction (so for the body fixed axis system which rotates together with the body), is given by equation 4.16.

$$(m + a)\ddot{\eta_{3-bf}} + b\dot{\eta_{3-bf}} + c\eta_{3-bf} = F_{ex3-bf} \tag{4.16}$$

in which m and a are mass and added mass respectively, b is the linearized damping, c is the stiffness, F is the excitation force and η_{3-bf} is the heave motion of the water in the body-fixed axis system.

For an inclined cylinder, as opposed to an upright one, the surface-piercing area of the geometry increases because the cylindrical shape becomes elliptical. This is illustrated in Figure 4.3.

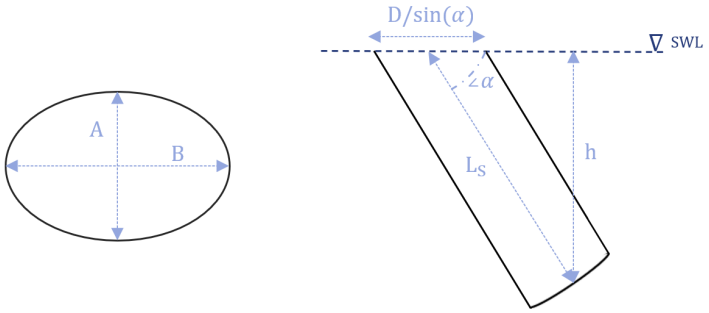

Figure 4.3: The surface piercing area and side-view of an inclined cylinder. [4] *(this figure is not to scale)*

For the surface piercing area in Figure 4.3, the length of A is equal to the diameter (D) of the cylinder and the length of B is equal to $D/\sin(\alpha)$. The surface piercing area is given by equation 4.17.

$$A_{wl} = \pi \frac{A}{2}\frac{B}{2} = \frac{\pi}{4}\frac{D^2}{\sin\alpha} \tag{4.17}$$

In the right Figure in Figure 4.3, D is the diameter of the cylinder, h indicates the submergence, L_s indicates the submerged length and α is the inclination angle with respect to the waterline.

For an inclined cylinder, compared to an upright cylinder with the same submergence, a larger submerged length is present. This submerged length depends on the inclination angle, since $L_s = h/\sin\alpha$. The natural frequency can be thus be found with equation 4.18 as stated by Balkema [4].

$$\omega_n = \sqrt{\frac{c}{m+a}} = \sqrt{\frac{A_{wl}\rho_w g}{A_{wl}\rho_w L_s + a(\omega)}} = \sqrt{\frac{A_{wl}\rho_w g}{A_{wl}\rho_w \frac{h}{sin(\alpha)} + a(\omega)}} \tag{4.18}$$

This implies that if the influence of the change in added mass is disregarded, the piston-mode natural period is inversely proportional to the sine of the inclination angle ($1/\sin(\alpha)$). This means that as the inclination with respect to the horizontal decreases, and assuming the submergence remains constant, the piston-mode natural frequency will decrease. However, in reality, the influence of the added mass cannot be disregarded, as it will have an impact on the piston-mode period [4].

4.3. Sloshing mode

The interaction between waves, vessel motions, and the monopile can induce a back-and-forth sloshing motion, characterized by sinusoidal deflections of the water surface within the cylinder. This generates discrepancies in water levels and applies pressure loads on the monopile due to fluid accelerations.

Bunnik and Veldman [8] analysed sloshing behaviour in a rectangular sloshing tank. They concluded that the exclusion of non-linearities and viscous effects in diffraction theory leads to a significant overestimation of the liquid motions at the natural sloshing frequencies of the sloshing tank. The first two natural modes for sloshing in a two-dimensional rectangular tank can be found in Figure 4.4 from the book *Sloshing* by Faltinsen and Timokha [17].

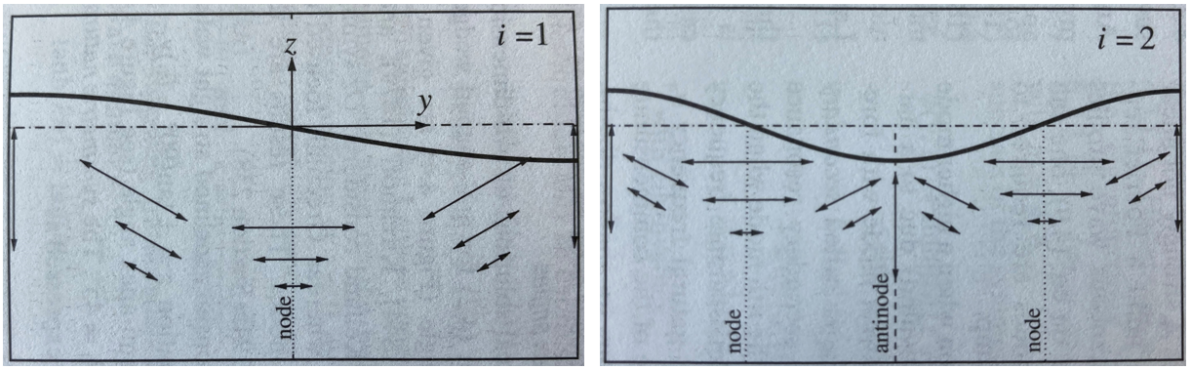

Figure 4.4: The first two natural modes for sloshing in a two-dimensional rectangular tank. Dotted and dashed lines refer to nodal and antinodal lines, respectively. Liquid particle motions at and between the nodal and antinodal lines are indicated by arrows [17].

Focusing on the sloshing behavior in a cylinder, lateral sloshing pertains to the behavior of the liquid surface within an upright cylinder when subjected to lateral excitation. The significance of lateral sloshing lies in its ability to generate asymmetric mode shapes. An overview of the governing equations and boundary conditions that are relevant to the issue of lateral sloshing in a two-dimensional and cylindrical tank will be presented in this chapter.

4.3.1. Natural frequency of the sloshing liquid

According to Ibrahim [22], when a partially filled container undergoes lateral excitation, the free surface of the liquid column inside the container may assume arbitrary shapes such as planar, non-planar, beating, or chaotic. Since theoretical analysis of this behaviour can be very difficult, the following assumptions are applied [64]:

1. To simplify the analysis and avoid the complications arising from container flexibility, it is assumed that the tank holding the liquid is rigid.
2. In order to linearize the problem, the assumption is made that the wave heights on the free surface of the liquid are small.
3. The analysis considers the liquid to be incompressible, irrotational, homogeneous, and inviscid.
4. It is assumed that the total volume of liquid within the tank remains constant.

4.3.2. Two-dimensional

Faltinsen and Timokha [17] noted that the most straightforward scenario in two dimensions, featuring precise analytical natural modes and frequencies, is related to the sloshing phenomenon occurring within a planar rectangular tank. When the method of Faltinsen and Timokha [17] is not applied to a rectangular tank but rather to the two-dimensional depiction of the monopile, equation 4.19 yields the natural frequency and period of sloshing.

$$\omega_i = \frac{2\pi}{T_i} = \sqrt{g\frac{\pi i}{D_i}\tanh(\frac{\pi i}{D_i}h)} \tag{4.19}$$

Figure 4.5 schematically clarifies the two-dimensional notation. In the two-dimensional representation of the monopile, the breadth of the tank is equal to the inner diameter of the monopile, D_i and the height of the liquid to the submergence of the monopile, h. Since the 2D geometry of the monopile does not have a bottom, equation 4.19 can only be used when the liquid-depth-to-breadth ratio, $h/D_i \gtrsim 1$. This is the deep liquid condition, when the liquid motions of the free surface do not "feel" the tank bottom [17].

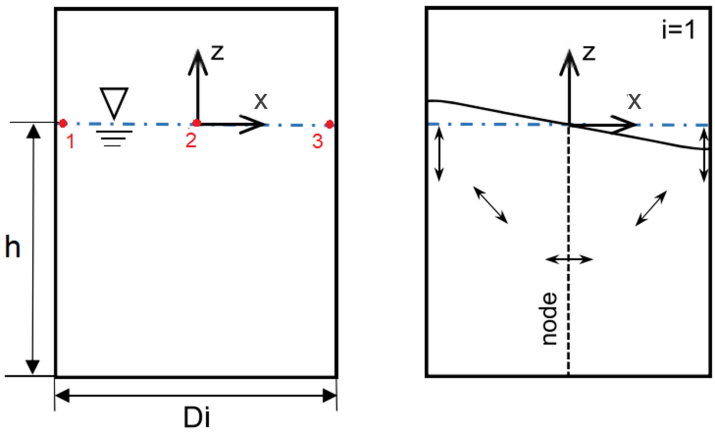

Figure 4.5: a) Mean liquid shape for a two-dimensional rectangular tank (with monopile notations). b) Standing wave corresponding to the first natural mode for sloshing. [25]

4.3.3. Inclined sloshing frequency - 2D

In the literature, specific research on the sloshing frequency for an inclined rectangular 2D geometry, where h > D (ensuring that the water surface does not interfere with the bottom of the geometry), is not present. If we consider Figure 4.5 as the starting point and rotate it around the center point on the still water level (SWL), the submerged length will remain constant. The length of the water surface will be equal to $D_i/\sin(\alpha)$, where α is the inclination angle (90 degrees corresponds to vertical). Incorporating the adjusted water surface length in equation 4.19 will be used as the first approximation of the natural sloshing frequency for an inclined 2D geometry. It is important to note that this will not provide an accurate determination of the sloshing frequency. Equation 4.19 for an open-ended structure is only valid for a deep liquid, a condition not met as the inclination angles decrease. Consequently, it is employed as a preliminary approximation, and the actual sloshing frequency will be determined through LPF and CFD.

4.3.4. Three-dimensional

In the three-dimensional analysis, the monopile geometry is conceptualized as an upright circular cylindrical tank. The geometric definitions of this tank are given in Figure 4.6, in which a cylindrical coordinate system is used (r, θ, z).

Based on the definitions in Figure 4.6, the cylinder in Figure 4.7 is considered with radius, R, and liquid height, h. Since the liquid is incompressible, irrotational and inviscid, the velocity field can be described as $v = \nabla\varphi$. The variable φ denotes the single valued velocity potential function and satisfies Laplace's equation:

$$\nabla^2\varphi = 0 \tag{4.20}$$

Since a closed cylinder is considered, the velocity potential satisfies the no-penetration condition at the side and bottom:

(4.21)

At the free surface the kinematic condition is present which states that the particles situated on the surface should stay on the surface. This condition is accompanied by the requirement that the pressure exerted on the liquid's surface remains constant [64]:

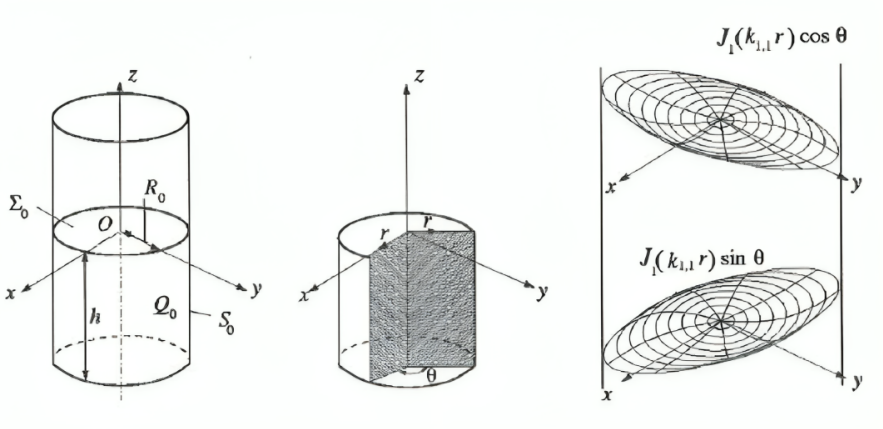

Figure 4.6: Geometric definitions for natural sloshing modes in an upright circular cylindrical tank. Meridional plane cross-section and wave patterns are shown for the two lowest modes (from [17]).

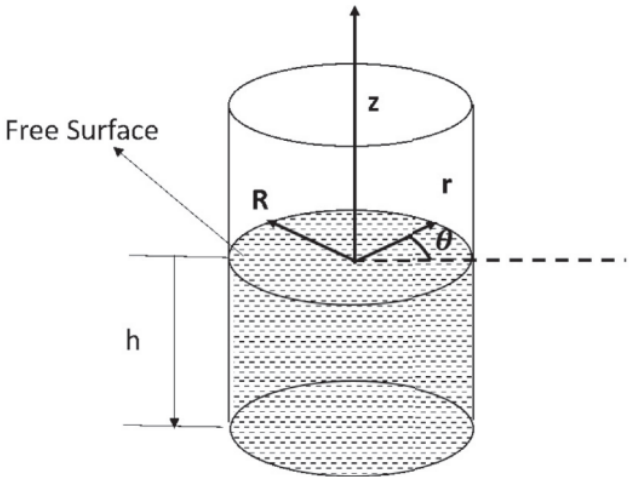

Figure 4.7: Cylindrical coordinate system (r, θ, z) assumed for the cylindrical tank containing liquid up to depth of h [64].

$$\frac{\partial^2 \varphi}{\partial t^2} + g\frac{\partial \varphi}{\partial z} = 0 \tag{4.22}$$

In equation 4.22, t is the time and g is the gravitational acceleration. As stated first by Bauer [5], the boundary value problem is solved to obtain the velocity potential function satisfying the conditions (4.20,4.21):

$$\varphi = \sum_m \sum_i \left[\alpha_{m,i}(t)\cos(m\theta) + \beta_{m,i}(t)\sin(m\theta)\right] J_m(k_{m,i}r)\frac{\cosh\left[k_{m,i}(z+h)\right]}{\cosh(k_{m,i}h)} \tag{4.23}$$

In equation 4.23, $\alpha_{m,i}$ and $\beta_{m,i}$ are time dependent variables, relying on the initial conditions of the free surface. J_m is the Bessel of the first kind, of order m. The wave number, $k_{m,i}$ is given by:

$$k_{m,i} = \frac{\iota'_{m,i}}{R}, \qquad m = 0, 1, 2, ..., \qquad i = 1, 2, ... \tag{4.24}$$

Table 4.1 provides the value of $\iota_{m,i}$, which represents the i^{th} zero of the derivative of the Bessel function of order m, denoted as J'_m.

If $\alpha_{m,i}$ and $\beta_{m,i}$ are expressed as harmonics functions and equation 4.23 is substituted in equation 4.22, the resonant frequencies for the sloshing modes, $\omega_{m,i}$, of the liquid column are given by the dispersion relation [22]:

$$\omega_{m,i}^2 = gk_{m,i} \tanh(k_{m,i}h), \quad m = 0, 1, 2, ..., \quad i = 1, 2, ... \tag{4.25}$$

From equation 4.25, it becomes clear that for large cylinders, the natural frequencies of the liquid are small. Also, when a cylinder is filled to a certain level, the natural frequencies of the liquid reach a point where they no longer vary with the liquid height. This occurs because the hyperbolic tangent function becomes approximately 1 ($\tanh(k_{m,i}h) \approx 1$). Then making the square of the natural frequencies $\omega^2 \approx gk_{m,i}$.

At the liquid height where $\tanh(k_{m,i}h) \approx 1$, the linearized hydrodynamic theory can also be applied to vertical cylinders without a bottom, since the natural frequency is then no longer dependent on the liquid height.

Table 4.1: The first roots $\iota_{m,i}$ of the derivative of the Bessel function J'_m.

$i \backslash m$	J'_0	J'_1	J'_2	J'_3	J'_4
1	3.8317	1.8412	3.0542	4.2012	5.3175
2	7.0156	5.3314	6.7061	8.0152	9.2824
3	10.1735	8.5363	9.9695	11.3459	12.6819
4	13.3237	11.7060	13.1704	14.5858	15.9641

These findings are also described by Ibrahim [22], and Faltinsen and Timokha [17]. The natural frequencies of sloshing are a function of the non-dimensional submergence-to-radius ratio [17]. This implies that the submergence of the liquid in relation to the cylinder's diameter affects the behavior until a certain steady-state is achieved. Ibrahim [22] formulated that for a partially filled circular, cylindrical container, the natural frequency remains constant when the ratio $h/R > 2$. Faltinsen and Timokha [17] states that a difference in natural frequency will be minimal when $h/R > 1.5$. The section above and the formulations by Ibrahim [22] and Faltinsen and Timokha [17] entail that in a sufficiently filled circular container, the resonance of the liquid at the bottom ceases, and only the top layer experiences sloshing.

Formula 4.26 defines the calculation of natural sloshing periods in three dimensions for the monopile, with the wave number excluded from the equation.

$$\omega_{m,i} = \frac{2\pi}{T_{m,i}} = \sqrt{2g\iota_{m,i} \tanh\left(2\iota_{m,i}h/D_i\right)/D_i} \tag{4.26}$$

In formula 4.26, $\omega_{m,i}$ denotes the sloshing frequency for the i^{th} mode, $\iota_{m,i}$ is the i^{th} zero of the derivative of the Bessel function of order m, denoted as $J'_m(\iota_{m,i}) = 0$. As before, h refers to the submergence (or draught) and D_i to the inner diameter.

If surface tension is considered, the natural frequency follows from equation 4.27, according to Ibrahim [22], in which σ is the surface tension and ρ_f is the liquid density.

$$\omega_{m,i}^2 = [gk_{m,i} + \frac{\sigma}{\rho_f}k_{m,i}^3] \tanh(k_{m,i}h), \quad m = 0, 1, 2, ..., \quad i = 1, 2, ... \tag{4.27}$$

This equation pertains to the slip contact line and demonstrates that surface tension leads to an increase in the normal mode frequencies.

The fluid surface elevation, η, measured from the undisturbed free surface is given by equation 4.28. In this equation $\bar{\alpha}_{m,i}$ and $\bar{\beta}_{m,i}$ are constant and determined from initial conditions.

$$\eta = \frac{1}{g}\sum_{m=0}^{\infty}\sum_{i=1}^{\infty}\left[\bar{\alpha}_{m,i}\cos(m\theta) + \bar{\beta}_{m,i}\sin(m\theta)\right]J_m\left(k_{m,i}r\right)\cosh\left(k_{m,i}h\right)\left(\omega_{m,i}\cos(\omega_{m,i}t)\right) \tag{4.28}$$

The symmetric mode shape is given by 4.29. For the first mode, $m = 0$, the motion exhibits symmetry around the center as angular ridges and furrows. In this situation, the roots of $J'_0(k_{0,1}r) = 0\,|_{r=R}$ are given in the first column of Table 4.1. The nodal circles corresponding to these modes are given by $\eta = 0$, or $J_0(k_{0,1}r) = 0$. Given that there is no lateral shift of the liquid center-of-mass for any of these modes, they do not generate any lateral forces or torques.

$$\eta(r,\theta,t) = \frac{1}{g}\sum_{m=0}^{\infty}\sum_{i=1}^{\infty}[\bar{\alpha}_{m,i}\cos(m\theta)]J_m\left(k_{m,i}r\right)\cosh\left(k_{m,i}h\right)\left(\omega_{m,i}\cos(\omega_{m,i}t)\right) \tag{4.29}$$

The asymmetric mode shape is given by 4.30. For the first mode, $m = 1$, there is a nodal diameter perpendicular to direction of the regular incident wave (or in the case of forced oscillation, the motion of the geometry). The roots of $J_1'(k_{1,1}r) = 0\,|_{r=R}$ are given in the second column of Table 4.1.

$$\eta(r,\theta,t) = \frac{1}{g}\sum_{m=0}^{\infty}\sum_{i=1}^{\infty}[\bar{\beta}_{m,i}\sin(m\theta)]J_m\left(k_{m,i}r\right)\cosh\left(k_{m,i}h\right)\left(\omega_{m,i}\cos(\omega_{m,i}t)\right) \tag{4.30}$$

In the present work, particular attention is given to the asymmetric mode shapes, since these are associated with a horizontal oscillation of the center of mass [70]. A 2D visual representation of first three asymmetric sloshing mode shapes in a 3D cylinder are shown in figure 4.8. For the first mode, $i = 1$, there is a nodal diameter perpendicular to the direction excitation, a positive peak at one wall, and a negative peak at the other wall. This mode is the fundamental asymmetric wave. The fundamental asymmetric wave is a standing wave with a wavelength twice the structure diameter and a node in the middle of the tank [17]. For the other modes, $i > 1$, there is an increasing number of intermediate peaks present. In figure 4.8 a sketch of the relative shift of the liquid center-of-mass is provided for each mode. The liquid center-of-mass shift for the fundamental mode ($i = 1$) is significantly larger compared to that of the higher modes for the same maximum wave amplitude. As the center-of-mass oscillation serves as the origin of slosh-induced forces and torques, the fundamental asymmetric wave generates considerably greater force and torque than any other mode [14]. For a 3D cylinder the analytical force oscillation description is given in Appendix C.

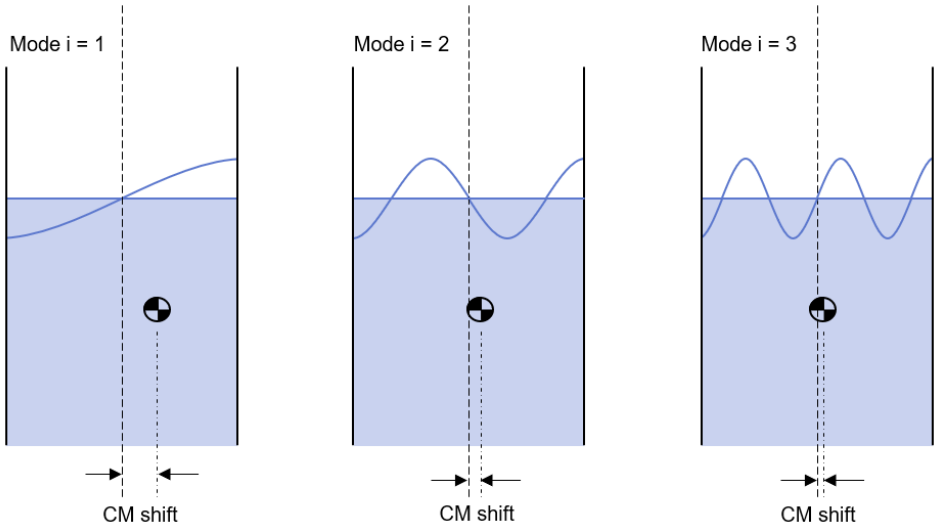

Figure 4.8: Slosh wave shapes for the first three asymmetric modes [14].

4.3.5. Inclined sloshing frequency - 3D

McNeill and Lamb [46] researched the fundamental sloshing frequency for an inclined, fluid-filled right circular cylinder. For an incompressible and inviscid fluid, in a tank with rigid walls, and only for small oscillations. Bugg [7] experimentally validated the method drafted by McNeill and Lamb [46]. Bugg [7] determined the frequency of liquid oscillations in a right circular cylindrical tank tilted at 0°, 30°, 45°, and 60° with respect to the vertical. The liquid fill height was varied as well. Two modes of oscillation were considered, one with its nodal line along the minor axis (the longitudinal mode) of the liquid free surface and one with is nodal line along the major axis (the lateral mode) of the surface. As the tank tilt angle increased, the frequency of both oscillation modes decreased. However, it was observed that the frequency of the former mode decreased significantly more than the latter mode as the tilt angle increased. In other words the frequency at which the first sloshing mode in longitudinal direction occurs, decreases most significantly when the inclination angle increases.

Table 4.2: The percentage deviation between the theoretical value for $\frac{\omega^2 R}{g}$ (from [46]) and the experimental results (from [7]) in percent for different inclination angles (α).

Inclination angle α	**Asymptotic value** [**46**]	**Deviation of** $\frac{\omega^2 R}{g}$ %
0	1.84	~ 0
30	1.24	10
45	0.834	14
60	0.491	~ 0

The theoretical curve for α = 0 degrees (i.e. in [7] and [46] this angle corresponds with an upright right circular cylinder), follows the expression:

$$\frac{\omega^2 R}{g} = 1.841 \cdot \tanh 1.841 \frac{h}{R} \tag{4.31}$$

In Figure 4.9 the coordinate system and the effect of liquid fill height and tilt angle on the longitudinal frequency are presented in the left figure. In the right figure, the experimental results from Bugg [7], are compared with the asymptotic values from McNeill and Lamb [46]. The asymptotic values predicted in [46] for the inclination angles are given in Table 4.2 as well as the deviation of the values for $\frac{\omega^2 R}{g}$ from the experimental result in the work by Bugg [7]. A cause of discrepancy between the theoretical description (from [46]) and the experimental results (from [7]) is the assumption in the theoretical description that the oscillating free surface remains flat. However, in reality, the actual free surface only remains flat under very small excitation amplitudes.

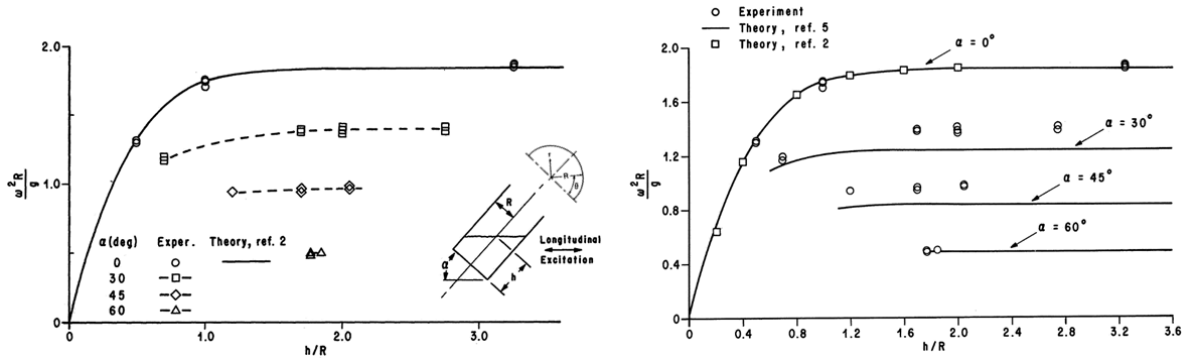

Figure 4.9: The left figure depicts, the effect of liquid fill height and tilt angle on longitudinal frequency (from [7]). The line '*Theory, ref. 2*' represents equation 4.31. In the right figure the theoretical data '*Theory, ref. 5*'(from [46]) is added for comparison.

5

Linear potential flow

In this chapter, the analytical derivations are used to determine the accuracy of a linear potential flow (LPF) model. For this model the diffraction software OrcaWave is used, produced by Orcina Ltd [57].

5.1. Diffraction modelling

The analysis of wave forces on a cylinder, aimed at determining the motions and forces, employs advanced three-dimensional linear radiation-diffraction analysis. In this analysis a linear approach is used, assuming small amplitude motions describe the waves and the cylinder oscillations. Due to this linear approach, the results will be presented in the frequency domain. The LPF method has some considerable limitations, most important of which are [8]:

- The model does not take into account the influence of viscosity.
- The fluid is assumed to be non-rotating.
- It is applicable only to minor ship movements and waves, as the boundary conditions are linearized.

However, it has been observed that the model yields satisfactory outcomes even in scenarios beyond its designated theoretical limits. As a result, further exploration was conducted to determine the potential usefulness of this method in predicting the impact of resonant behaviour of the internal water column on the movement of an open-ended vertical cylinder.

For the first part of the research the following assumptions are used:

- Only vertical, open-ended, thin-walled cylinders are analysed, assuming symmetrical mass distribution.
- The environment contains a unidirectional wave heading in positive x-direction (0.0°) and infinite water depth with a water density of 1.025 (te/m^3).
- The buoyancy of the cylinder is negligible compared to its weight.

Due to the first two assumptions, the vertically oriented body of revolution has three degrees of freedom, consisting of two translations in surge and heave and one rotation in pitch direction [45]. These motions will be analysed in the first part of this research.

5.1.1. Governing equations

The diffraction theory is comprehensively explained by Journée and Massie [26], particularly in Section 7.4.1 of their work. Therefore, their work is recommended as a reference for this section. A more elaborate description of the linear radiation-diffraction method used is given in Appendix B. The following explanation presents the theory in terms of hydrodynamic forces, but it is equally applicable to moments.

In linear potential theory, the potential of a floating object results from the combination of potentials arising from the undisturbed incoming wave (Φ_I), the scattered potential caused by the presence of a

fixed obstructing body (Φ_S), and the radiation potential, associated with the first-order oscillatory forced motions of the body (Φ_R).

The pressure on the panels is determined from the velocity potentials, via the linearized Bernoulli equation, as in B.2. The forces resulting from these pressures can be written as:

$$F = \rho \iint_S \left(\frac{\partial \Phi_I}{\partial t} + \frac{\partial \Phi_S}{\partial t} + \frac{\partial \Phi_R}{\partial t} + gz \right) \cdot n \cdot dS_B \tag{5.1}$$

In which n is the outward facing normal on dS_B and S_B the wetted body surface.

In equation 5.1, the term $\rho g z$ represents the hydrostatic buoyancy in still water. The hydrodynamic coefficients (A_{jk},B_{jk}) and the first-order wave forces F_j are determined by integrating the pressure (B.2) across the submerged section of the structure. Using these outcomes, the coupled equation of motion (4.1) is resolved for the motions in six directions.

The force can be subdivided into two components: the 'reactive' added mass and damping components, and the 'active' wave excitation components. The reactive force is due to the radiation waves induced by body motions in still water. The reactive forces are determined with the radiation potential. The added mass coefficients, dependent on the acceleration of excitation, are given by:

$$A_{jk} = -\Re\mathfrak{e} \left\{ \rho \iint_{S_B} \Phi_{R,k} n_j dS_B \right\} \tag{5.2}$$

The damping coefficients, dependent on the velocity of excitation, are given by:

$$B_{jk} = -\Im\mathfrak{m} \left\{ \rho\omega \iint_{S_B} \Phi_{R,k} n_j dS_B \right\} \tag{5.3}$$

The 'active' force components are derived from the undisturbed wave load (the Froude-Krylov force) and the diffraction load (resulting from the scattered potential). The resultant of these loads on a fixed body, is referred to as the wave excitation forces. The wave excitation forces are expressed as follows:

$$F_{FK} + F_{diff} = \rho \iint_{S_B} \left(\frac{\partial \Phi_I}{\partial t} + \frac{\partial \Phi_S}{\partial t} \right) n \cdot dS_B \tag{5.4}$$

5.1.2. Dipole panels

The requirements for the use of conventional panels in diffraction analysis are described by DNV [13]. In the diffraction analysis mentioned in this document, also dipole panels are used. The reason for using dipole panels is that the integral equations used in diffraction analysis are ill-conditioned for thin walled cylinders of thickness t, in combination with a large diameter of the cylinder. To resolve this problem, one could use panel sizes which are less than t. However, implementing such small panels in simulations can be impractical due to the need for a large number of mesh panels, resulting in computationally expensive calculations that may not be feasible or cost-effective.

Thus, a more viable approach is to utilize well-conditioned integral equations that are applicable in the idealized limit of vanishing thickness (t = 0), which can offer more efficient and computationally feasible solutions. The validity of using dipole panels will be explained in more depth in Section 5.2.1.

5.2. Piston mode

As mentioned in Section 4.2.1, the two-dimensional Molin [48] approximation for the piston-mode provides accurate approximations for three-dimensional cylindrical situations [25]. The piston mode as a function of diameter and submergence following from the analytical description by Molin [48] (equation 4.5) for an infinitely thin cylinder ($D_o = D_i$) is given in Figure 5.1.

The result of these analytical approximations to find the natural frequency of the piston mode considering added mass for a cylinder with a diameter of 11 meter at various submergence, h, can be found in Table 5.1. The natural frequency of the piston mode following from the diffraction model, using dipole panels, is also given in Table 5.1. The last column in the table represents the percentage deviation (Δ) between the Falnes analytical value and the diffraction value. The Falnes [15] method is favored over the Molin [48] and Fukuda [13] methods in this context, as the Molin method is formulated for a two-dimensional moonpool, whereas the Fukuda method pertains to a three-dimensional moonpool.

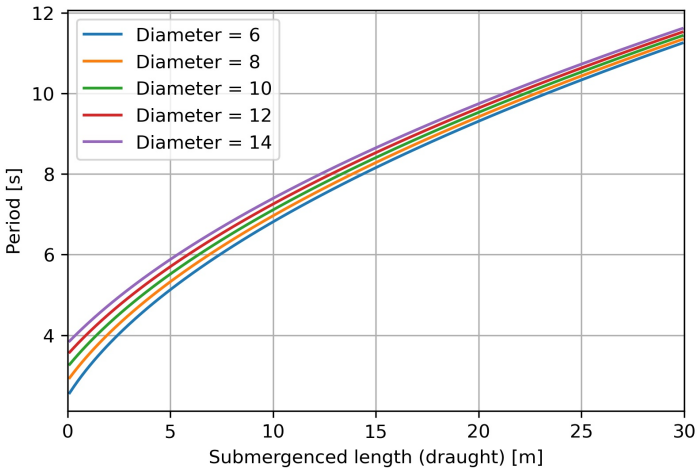

Figure 5.1: Molin's [48] piston mode period for infinitely thin cylinder as a function of diameter and submerged length.

The natural frequency derived from the diffraction model is based on the sea state RAOs. Sea state RAOs provide results at the field points for both pressure in the fluid and fluid velocity. Consequently, these RAOs will now be referred to as field point RAOs. The response amplitude of the vertical surface elevation of a field point is given by $\frac{z_a}{\zeta_a}(\omega)$. The first-order complex pressure and velocity are given in terms of the total first-order potential [57].

The field point is placed exactly in the centre $(x, y) = (0, 0)$ of the cylinder and follows the surface elevation in the z-direction. The first peak of the surface elevation of this field point is considered to coincide with the natural piston frequency. The absolute value of the surface elevation of the field point is visualized in Figure 5.2, since the field point RAO is a complex number. The three vertical lines with corresponding colors in Figure 5.2 represent the Falnes analytical approximation for the piston mode natural frequency. The peaks in the surface elevation curves at higher angular frequency are related to the sloshing resonance, which will be treated in Section 5.3.

The peak in surface elevation during piston mode resonance increases with greater submergence. This can be elucidated by considering the water column's ability to move up and down, generating waves that radiate away from the cylinder. With increased submergence, the energy dissipating through radiation diminishes because of reduced interaction with the surface water level outside the cylinder.

Table 5.1: Comparison of the natural piston mode frequency, ω_p, for a cylinder with D = 11 m, determined with different methods. The last column presents the percentage deviation between the Falnes [15] analytical approximation and the $\omega_p^{diffraction}$.

h [m]	ω_p^{Molin} [rad/s]	ω_p^{Fukuda} [rad/s]	ω_p^{Falnes} [rad/s]	$\omega_p^{diffraction}$ [rad/s]	Δ [%]
5	1.12	1.01	1.13	1.10	2.23
10	0.875	0.818	0.877	0.880	0.324
20	0.656	0.631	0.657	0.660	0.508

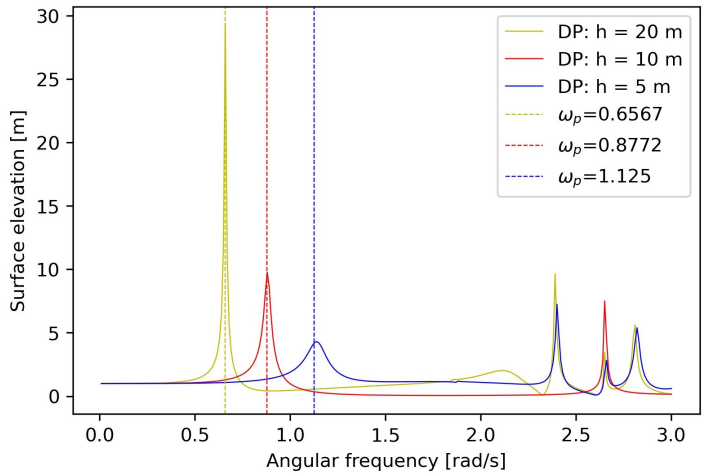

Figure 5.2: Absolute value of the field point RAO at center of cylinder [D=11m] at various submergence, h, with dipole panels. The vertical lines represent the analytical values from the Falnes approximation (equation 4.15).

5.2.1. Dipole panels vs. conventional panels

To investigate the validity of the dipole panels, the analysis from Figure 5.2 is also executed with a cylinder with the same inner diameter $(D = 11m)$, but with a wall thickness (WT) of 0.5 meter, resulting in an outer diameter of 12 meter. The results of this analysis in combination with the dipole panels (DP) results for the same frequency domain are given in Figure 5.3. The same trend can be observed for the surface elevation at the center of the cylinder for the DP and the WT model. Focusing on the lower frequency range, where the piston mode is observed, the resonance frequency of the model with wall thickness is slightly lower than for dipole panels. The deviation between the results should be sought in the nature of the dipole panels. Unlike conventional panels, the dipole panels are wet on both sides. Therefore, OrcaWave employs well-conditioned integral equations that apply in the idealized limit (thickness $t = 0$) [57].

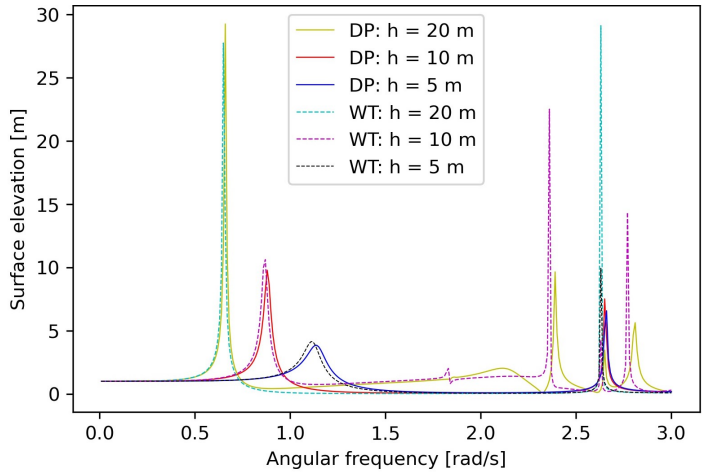

Figure 5.3: Absolute value of the field point RAO at center of cylinder [D=11m] at various submergence, h (DP = Dipole & WT = Wall thickness).

In Figure 5.4 the mesh view from OrcaWave is for both models analysed in Figure 5.3. The submergence is $h = 10m$. The waterlines and sea surface are indicated with blue. The model to the right shows the dipole panels (green) and the model to the left the conventional panels (red), this model includes a interior lid (yellow) to suppress the irregular frequencies between the panel layers. OrcaWave has a build in mesh validation, which performs various tests to all panels. This validation checks if the input data is correct and otherwise changes should be made to the panels supplied in the mesh files.

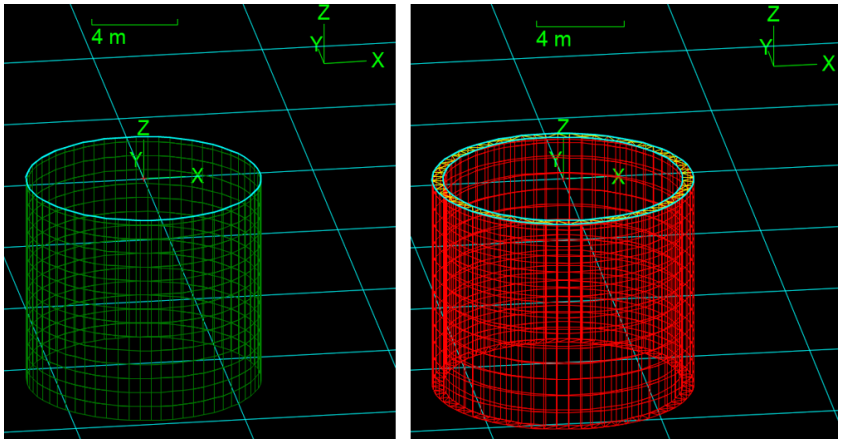

Figure 5.4: OrcaWave mesh view of cylinder with dipole panels (left) and conventional panels (right) at a subermence of $h = 10m$. Only the submerged panels are shown.

5.3. Sloshing

5.3.1. Asymmetric sloshing mode

The surge, sway, roll, or pitch excitations with a period, T, close to the highest natural period are of particular practical concern (Faltinsen and Timokha [17]). For the first mode, $m = 1$, the surface motion shows a nodal diameter perpendicular to the direction of rocking the container [22], as is visualized in Figure 4.8. Thus, for the first asymmetric sloshing mode, half a wave length fits into the width of the cylinder. The value of $\iota'_{m,I}$ for the fundamental mode, with $m = 1$ and $i = 1$, is found to be 1.84 (see Table 4.1). In Figure 5.5 the period $T_{1,1}$, based on equation 4.26, is given as a function of radius R for different values of the liquid depth h.

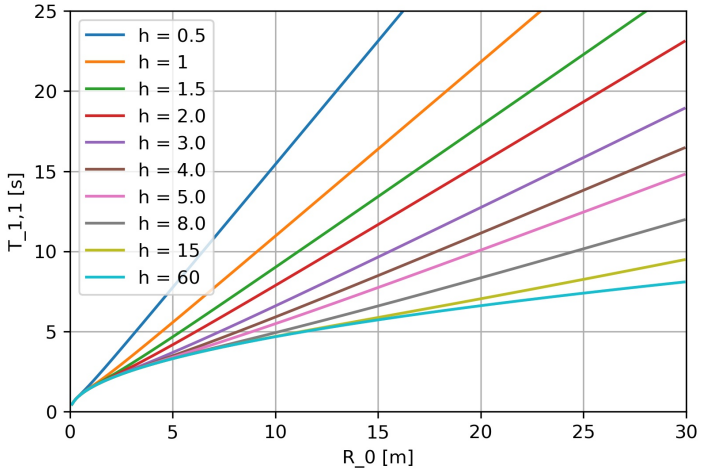

Figure 5.5: The highest natural period $T_{1,1}$ as a function of radius R_0 for an upright circular cylinder tank.

Initially, we verify whether the resonance frequencies determined analytically by equation 4.26 align with the frequencies exhibiting resonance behavior in the OrcaWave results. Subsequently, the characteristics of the added mass and damping curves are elucidated, followed by a comprehensive discussion of the results.

The following analysis is done for upright open cylinders with different diameters. The submergence has a constant value of h = 20 meters. In the analysis dipole panels are used for the whole geometry.

Added mass

The added mass in surge direction is plotted for cylinders with dipole panels, with varying diameters in Figure 5.6. In the figure, the analytically determined first sloshing frequencies (using equation 4.26) are

indicated by the dotted vertical lines. In Figure 5.7 a non-dimensionalized representation of the same results is given. The added mass is non-dimensionalized by dividing by the mass of the water column inside the cylinder and this dimensionless added mass is plotted against the non-dimensional relative wave height. The shape of the added mass curve can be explained by the sloshing dynamics in linear theory. Initially, there is a rise in the added mass, this is anticipated as the upper part of the internal water column start sloshing back and forth, in-phase with the incoming wave on the outside. The added mass coefficients increases towards infinity, until the resonance frequency is reached, at which the sloshing motion switches to out-of-phase with the incident wave, resulting in a vertical asymptotic as the added mass tends to negative infinity.

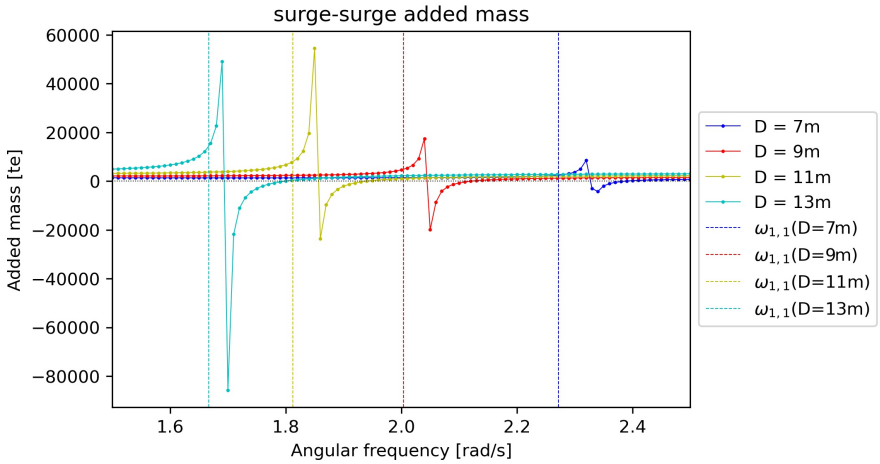

Figure 5.6: The added mass for an open ended cylinder. Different diameters are analysed analytically and with diffraction software. The submergence has a constant value of $h = 20m$. The vertical lines represent the analytical values following from equation 4.26.

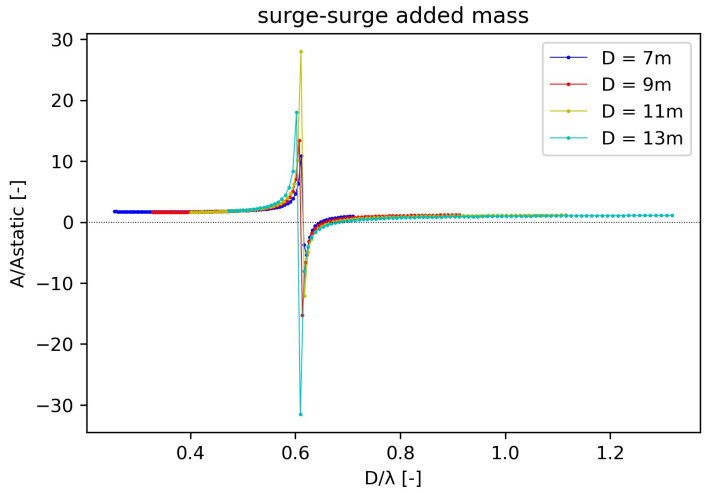

Figure 5.7: Non-dimensionalized Figure 5.6 by placing the value for D/λ on the x-axis, and A/A_{static} on the y-axis.

In Figure 5.6 it is visualized that the peaks in added mass do not correspond fully with the analytical sloshing frequency value found for a circular tank determined with equation 4.26. Table 5.2 shows the values and the deviation (Δ). It is evident that the analytically determined first sloshing frequency has a lower value than the frequency at which the added mass peaks due to the first sloshing mode.

Table 5.2: Comparison of the natural frequencies for the 1^{st} asymmetric sloshing mode $\omega_{1,1}$.

D [m]	$\omega_{1,1}^{diffraction}$ [rad/s]	$\omega_{1,1}^{analytical}$ [rad/s]	Δ [%]
7	2.32	2.27	2.13
9	2.04	2.00	1.82
11	1.85	1.81	2.09
13	1.69	1.67	1.38

In Figure 5.8 the 2^{nd} asymmetric sloshing mode natural frequency, $\omega_{1,2}$, are given. Again, for the analytical value, equation 4.26 is utilized and a submergence of 20 meter is given to the cylinder. Notice that compared to Figure 5.6, the peaks have significantly lower amplitudes and the frequency range of the horizontal axis is different. The second asymmetric modes for smaller diameters are not taken into account, since these occur at wave frequencies considered too high. Table 5.3 shows the frequency of the peak and the deviation to the analytically determined sloshing frequency (Δ).

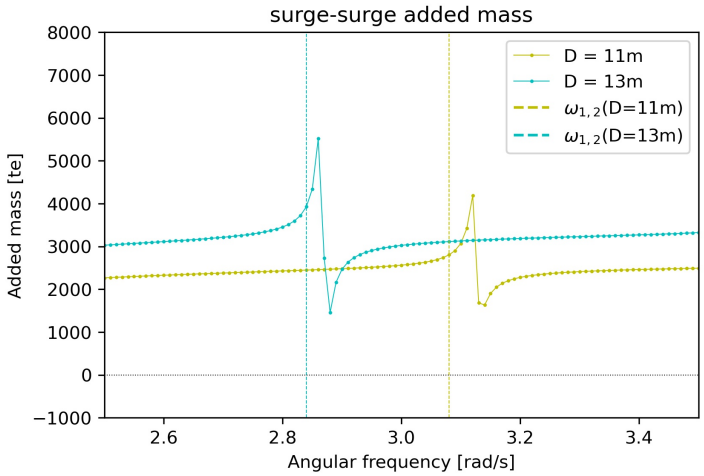

Figure 5.8: The added mass for an open ended cylinder. Different diameters are analysed analytically and with diffraction software. The submergence has a constant value of $h = 20m$. The vertical lines represent the second asymmetric sloshing frequencies following from equation 4.26.

Table 5.3: Comparison of the natural frequencies for the 2^{nd} asymmetric sloshing mode $\omega_{1,2}$.

D [m]	$\omega_{1,2}^{diffraction}$ [rad/s]	$\omega_{1,2}^{analytical}$ [rad/s]	Δ [%]
11	3.13	3.08	1.30
13	2.86	2.84	0.825

Damping

For slow oscillations (low frequency, where D/λ is small), the damping is small. As the wave frequency approaches the resonance frequency, the damping rapidly increases, potentially reaching an infinite value. This behavior is a result of the resonance phenomenon in the water inside the cylinder. Beyond the resonance frequency, for frequencies higher than resonance, the damping decreases again. In Figure 5.9 the damping corresponding to the added mass in Figure 5.6 can be found. A plot of the damping, at non-dimensionalized frequencies, is shown in Figure 5.10.

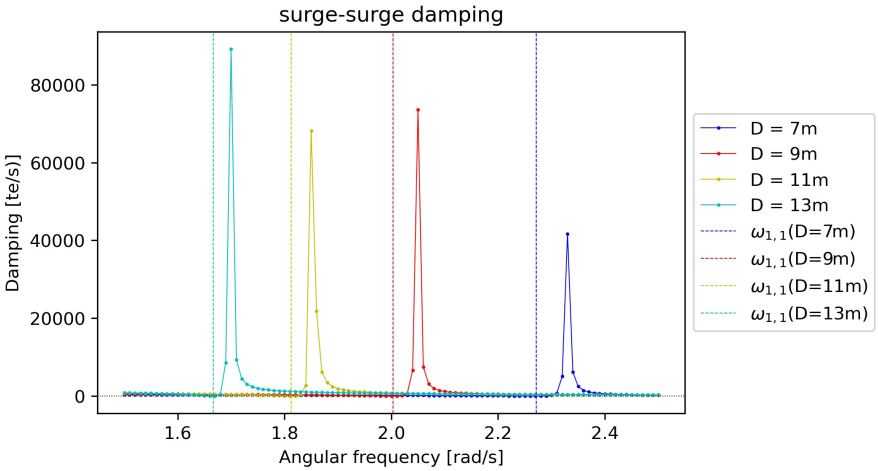

Figure 5.9: The damping for an open ended cylinder. Different diameters are analysed analytically and with diffraction software. The submergence has a constant value of $h = 20m$. The vertical lines represent the sloshing frequencies following from equation 4.26.

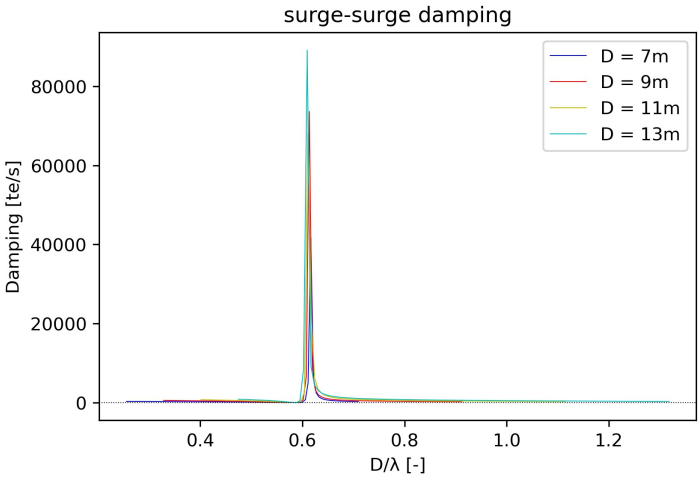

Figure 5.10: Adjusted Figure 5.9 by placing the value for D/λ on the x-axis.

Phase shift

Due to linearity, the force amplitude F_a is proportional to the wave amplitude ζ_a. This is referred to as the load RAO, representing the response amplitude characteristics $\frac{F_a}{\zeta_a}(\omega)$. The load RAO in surge direction is given in (5.11. The load RAO is composed of the wave excitation forces (the Froude-Krylov force and the diffraction force), as given in equation . Since viscous damping effects are disregarded, the linear theory predicts infinite steady-state response for a forcing frequency close to resonance of the liquid column. The absence of viscous damping is the key factor, as the sole potential damping source (radiated waves) is not possible for the liquid column due to the surrounding geometry. At the point in Figure 5.12 where the load RAO becomes zero ($D/\lambda \approx 0.59$), the internal sloshing waves are precisely out-of-phase with the incoming undisturbed wave. This leads to a 180-degree phase shift in the wave exciting force.

The phase shift is visualized in figure 5.11b and 5.12b. This abrupt phase shift is notable in this context due to the minimal damping of the cylinder. From the figures representing the added mass, damping, and load RAO (5.11,5.12) in the surge direction, it can be concluded that a 180-degree phase shift leads to a reduction in load to zero, followed by a rapid increase in the total wave force due to the potential damping rapidly increasing. Both phenomena arise from resonant behavior. First, the shift from out-of-phase to in-phase sloshing involves a phase adjustment, nullifying the wave exciting force. Second, as the in-phase behavior intensifies, this leads to substantial wave heights characterized by a sloshing motion within the cylinder.

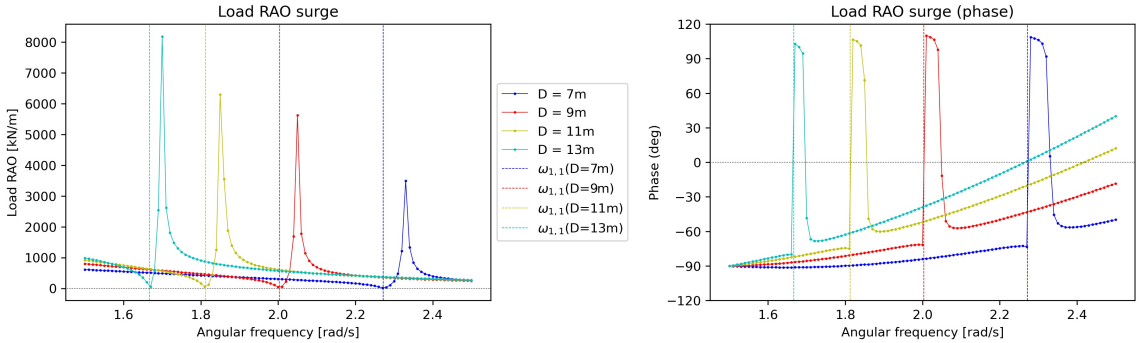

(a) Amplitude **(b)** Phase

Figure 5.11: Load RAO in surge direction for an open ended cylinder. Different diameters are analysed analytically and with diffraction software. The submergence has a constant value of $h = 20m$. The vertical lines represent the analytical values following from equation 4.26.

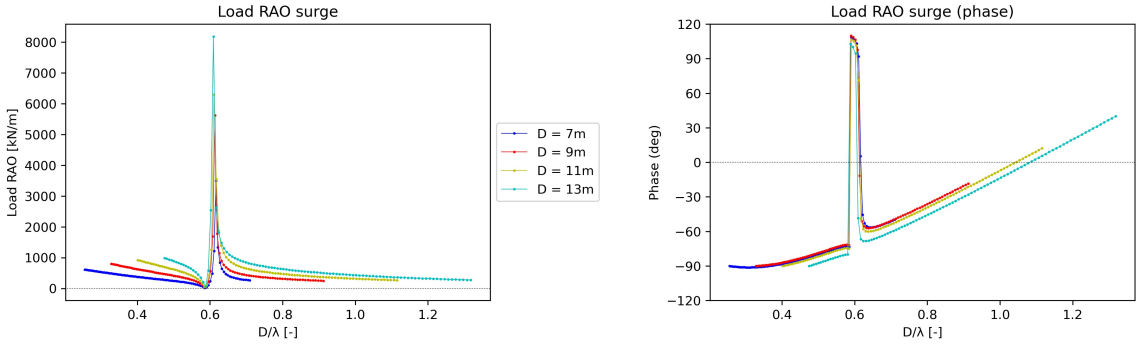

(a) Amplitude **(b)** Phase

Figure 5.12: Adjusted Figure 5.11 by placing the value for D/λ on the x-axis.

5.3.2. Symmetric sloshing mode

The surface motion of the first symmetric sloshing mode, $m = 0$, is symmetric about the origin in the form of angular ridges and furrows [22]. This mode is anticipated to exert minimal influence on the motions of the structure when compared to the asymmetric sloshing modes discussed in the previous section. This is because the peaks and troughs will symmetrically occur on opposite walls, resulting in the cancellation of forces. Additionally, there will be no horizontal Center of Gravity (COG) shift due to the symmetry about the vertical center axis. Figure 5.13 is a graph of the field point RAO at the center of the cylinder for different diameters. The vertical dotted lines give the analytical values for comparison, and the frequency range is bounded on the relevant region. Table 5.4 compares the value from the diffraction analyses and the analytical approach (i.e. equation 4.26).

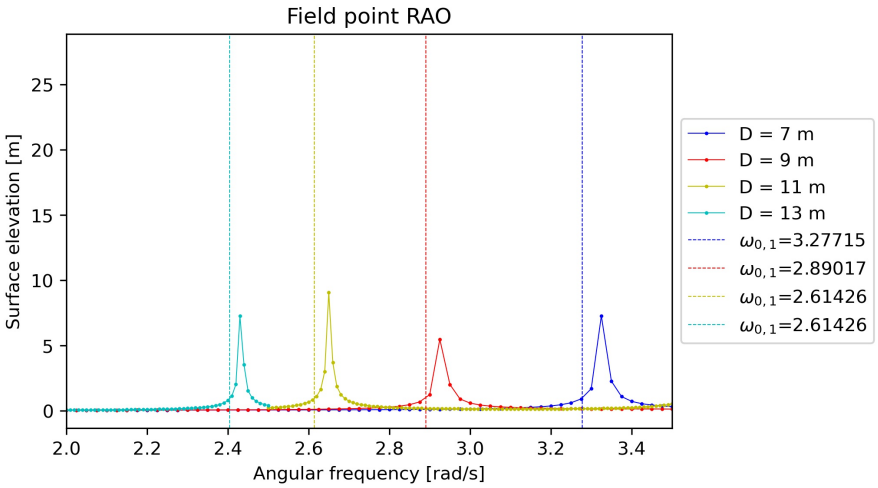

Figure 5.13: Absolute value of the field point RAO at center of cylinder for different diameters. The vertical dotted lines indicate the analytical value for the first symmetric sloshing mode, $\omega_{0,1}$ (see Table 5.4). The vertical lines represent the analytical values following from equation 4.26.

Table 5.4: Comparison of the natural frequencies for the 1^{st} symmetric sloshing mode $\omega_{0,1}$.

D [m]	$\omega_{0,1}^{diffraction}$ [rad/s]	$\omega_{0,1}^{analytical}$ [rad/s]	Δ [%]
7	3.33	3.28	1.46
9	2.93	2.89	1.21
11	2.65	2.61	1.37
13	2.43	2.40	0.84

5.3.3. Damping lid

The governing equations in diffraction modeling assume irrotational and inviscid fluid flow. While this assumption is applicable in numerous scenarios, it can lead to an overestimation of the response during resonance. In reality, viscous effects often dampen the response, and these effects are not accounted for by potential theory. The resonance of the fluid within the open-ended cylinder is such a situation, where potential theory tends to over-predict the amplitude of the response at a particular wave frequency.

Introducing a damping lid inside the open-ended cylinder, on the free water surface, introduces viscosity and enhances the realism of potential theory models. Nevertheless, it is crucial to investigate the appropriate level of damping that the lid should impose. In the present work, Computational Fluid Dynamics (CFD) analysis is employed to determine the optimal amount of damping required for obtaining physically valid results (7.2.1). A mesh view of the damping lid used in a cylinder model with dipole panels is given in Figure 5.14.

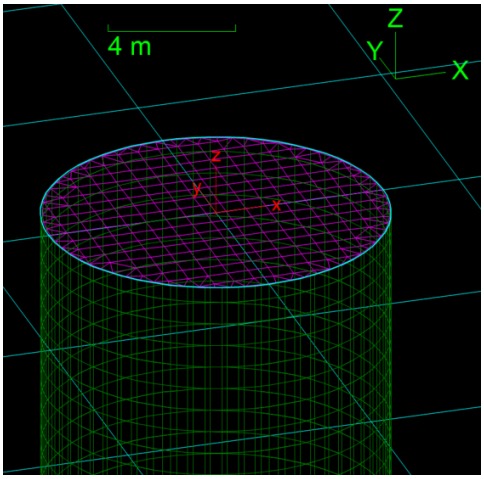

Figure 5.14: OrcaWave mesh view of cylinder with dipole panels and a damping lid, at a submergence of $h = 20m$. Only a part of the submerged panels are shown.

The use of the damping lid should not be mistaken for the interior lid, as depicted in Figure 5.4. In this study, the 'interior lid' refers to panels implemented to suppress irregular frequencies, while the 'damping lid' pertains to panels utilized to attain more realistic resonance results.

The damping lid model, used in OrcaWave, employs a model that incorporates a damping term directly proportional to the free-surface elevation, η, within the free-surface boundary condition (specifically, scheme 6 as outlined in the work by Li [37]). The modified free-surface boundary condition is given in equation 5.5. The initial free-surface boundary condition is provided in Appendix B, equation B.4.

$$g\frac{\partial \phi}{\partial Z} - \omega^2[1 - i\epsilon(\mathbf{F})]\phi = q_F(\mathbf{X}) \qquad \mathbf{X} \in S_F \tag{5.5}$$

In equation 5.5, the parameter ϵ is the non-dimensional damping coefficient. If $\epsilon = 0$, the classical free-surface boundary condition is restored. When $\epsilon > 0$, a damping lid is introduced at the free-surface. Generally, the damping coefficient is advised to be small, as it minimizes the influence of the damping lid at frequencies away from resonance. For instance, in a study by Chen [11] on resonance in a narrow gap between two barges, a damping coefficient of $\epsilon = 0.016$ is determined to exhibit favorable agreement with the measured data.

The influence of introducing a damping lid on the added mass and damping and Load RAO is given in Figures 5.15, 5.16 and 5.17. In Figure 5.15, it is evident that with an increasing damping coefficient, the added mass around the resonance frequencies decreases. This outcome is anticipated, as the standing wave inside the cylinder is dampened. At the highest damping factor in the analysis ($\epsilon = 0.3$), the curve becomes similar to that of the solid cylinder (closed bottom). The additional added mass between solid and the $\epsilon = 0.3$ curve is the water column inside the cylinder. As visualized in Figure 5.16, when the damping coefficient is increased, the radiation damping decreases, particularly at frequencies around

the resonance frequencies. In Figure 5.17, the load RAO is given. It is clear that the suppression of standing waves inside the cylinder, by increasing the damping coefficient, ϵ, suppresses the phase shift effect.

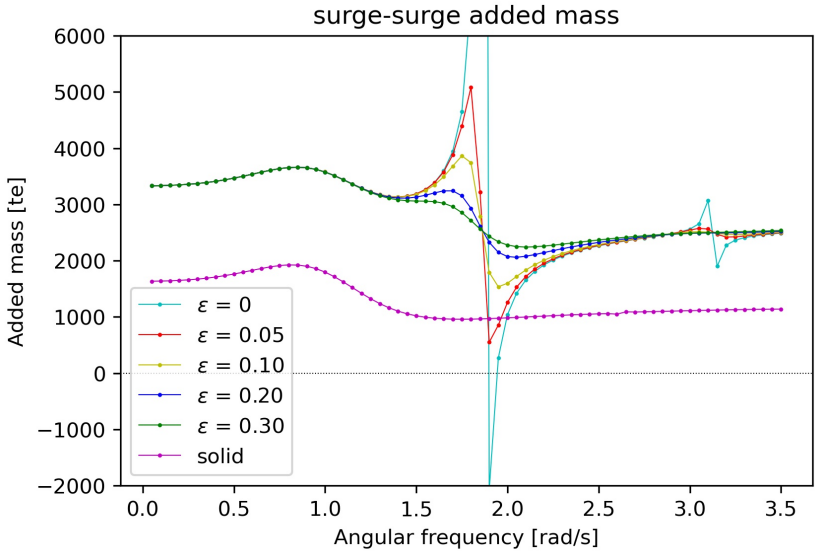

Figure 5.15: The added mass for an open ended cylinder with damping lid. Different values for the damping lid parameter, ϵ, have been applied. Also a closed bottom (solid) cylinder is used for reference. The submergence has a constant value of h = 20m.

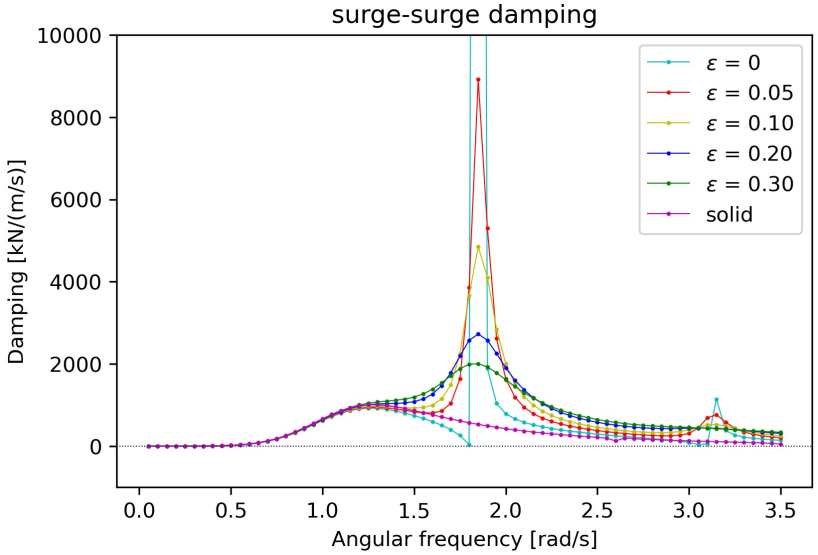

Figure 5.16: The damping for an open ended cylinder with damping lid. Different values for the damping lid parameter, ϵ, have been applied. Also a closed bottom (solid) cylinder is used for reference. The submergence has a constant value of h = 20m.

There is a substantial amount of empirical evidence in diffraction analysis and computational fluid dynamics that supports the notion that the boundary condition 5.5 exerts a beneficial damping influence on resonant wave motions [37]. Nevertheless, the theoretical justification is limited since 5.5 does not attempt to incorporate the viscous effects present in the Navier-Stokes equations, which are absent in potential theory. Therefore, validation with CFD increases reliability. This will be elaborated on in Section 7.2.1.

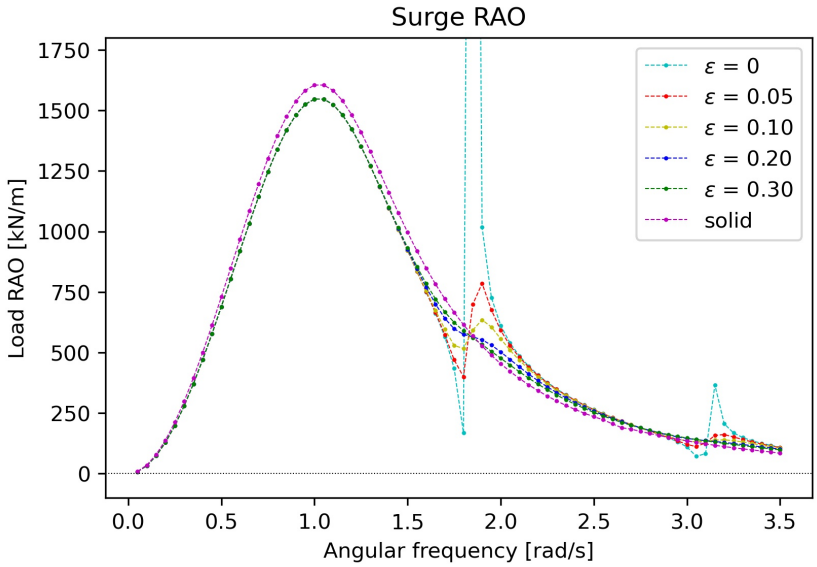

Figure 5.17: The Load RAO for an open ended cylinder with damping lid. Different values for the damping lid parameter, ϵ, have been applied. Also a closed bottom (solid) cylinder is used for reference. The submergence has a constant value of h = 20m.

5.3.4. Two-dimensional approach

A two-dimensional analysis of the monopile within the framework of linear potential flow is employed for comparison with the CFD model, as elaborated on in Section 6.

To obtain a two-dimensional result from OrcaWave, the geometry mesh in the software is elongated along the y-axis. The incident wave direction is head waves (thus along the x-axis), consistent with all previous models. To derive the two-dimensional approximation, the results are divided by the elongated y-extent of the stretched geometry. In Figure 5.18, a depiction of the mesh geometry utilized in the model is presented. Two models are employed, one with dipole panels and one with conventional panels. The conventional panel geometry features an inner diameter of 11 meters and an outer diameter of 12 meters (prior to elongation along the y-axis). For the dipole panels, a diameter of 11 meters is used. The conventional panel geometry aligns with two-dimensional geometry definition in the CFD analysis outlined in Section 6. The model's results are divided over the total length of the geometry in the y-direction to achieve a 2D representation.

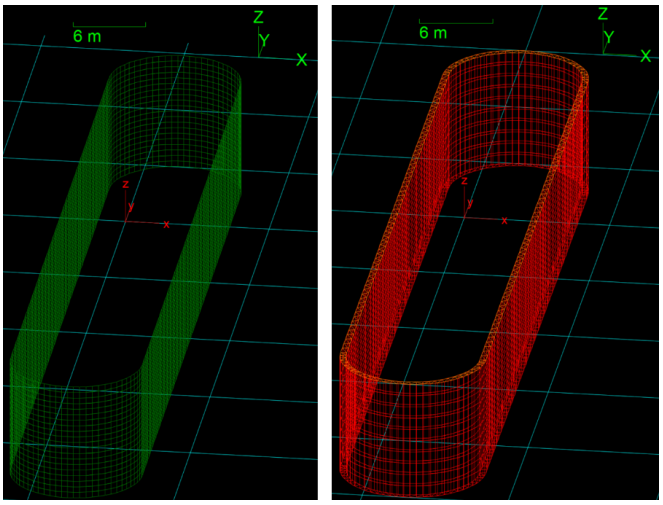

Figure 5.18: Mesh view of the OrcaWave models ($left$ = dipole panels, $right$ = conventional panels), showcasing the configuration used for the two-dimensional diffraction analysis. Wall thickness ($right$ model) is 0.5 $meters$ and submergence (h) is 10 $meters$.

5.4. Focus on 10 meter submergence

The piston mode can be well observed in the measured surface elevation during the LPF analyses shown in Figure 5.19 for a vertical cylinder with an inner diameter of $11m$ and a submergence of $10m$. The first symmetric sloshing mode is also visible in the field point RAO as the peak at the higher frequency. The black horizontal dotted lines in the figure represent surface elevations of 1 meter and 0 meters. It is evident that, up to the natural frequency of the piston mode, the surface elevation inside the geometry follows the wave height of the incident wave. However, at higher frequencies, the incident waves are reflected by the geometry, and the water inside the cylinder remains undisturbed (except for the symmetric sloshing resonance), no longer following the wave pattern.

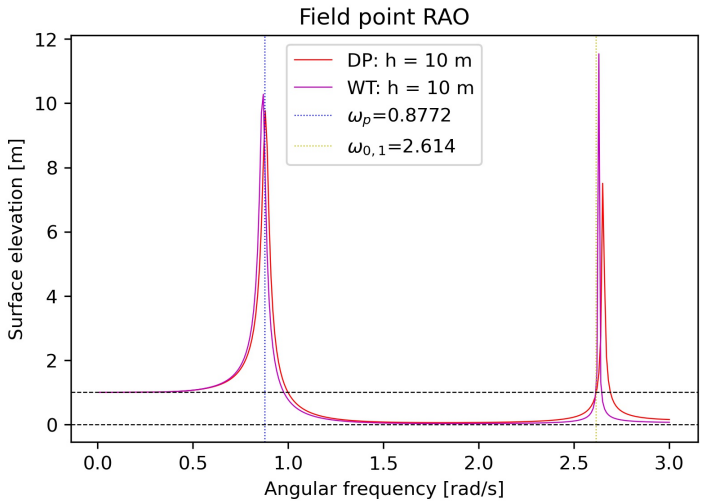

Figure 5.19: Absolute value of the field point RAO at center of cylinder [D=11m] at a submergence of 10 meters, with DP = dipole and WT = wall thickness. The field point is in the centre of the cylinder. The analytical value for the piston mode is based on the Falnes approximation (equation 4.15) and the analytical first symmetric sloshing mode follows from equation 4.26.

For the same MP the first sloshing mode can be found in the LPF analysis in the load RAO and the added mass. The load RAO represents the wave excitation load relative to the wave amplitude. The wave excitation load is the summation of the Froude-Kriloff loads and the diffraction loads. At the resonance frequency of the first sloshing mode, the added mass and damping become negative and the total wave force goes rapidly up. This can be explained by the resonance behaviour. The transition from sloshing that is out-of-phase to being in-phase is accompanied by a phase adjustment, causing the wave-induced force to become zero. As in-phase behavior becomes more pronounced, this leads to significant wave heights (sloshing) within the cylinder.

The surface elevation results following from the LPF simulations are visualized using the CAD software Rhino. The results at piston mode and sloshing mode resonance for the model with dipole panels is visualized in Figures 5.22 and 5.23 respectively.

The LPF results show reasonable resemblance with the analytical approximation in terms of resonance frequency. However it should be stated that viscous damping is not taken in account by the LPF theory. Also, the LPF theory neglects non-linear behaviour, which could be significant based on the observations at the SINTEF model testing campaign [30]. To evaluate if non-negligible sloshing inside the MP may occur, non-linearities matter. Therefore a second approach using CFD will be used to investigate further.

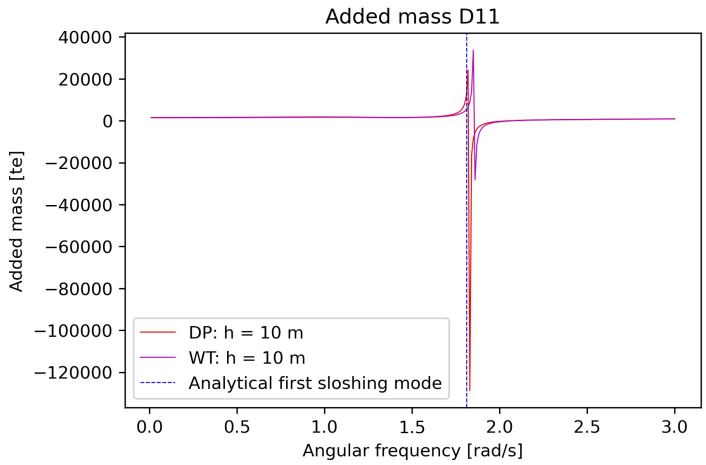

Figure 5.20: Added mass in surge direction (wave in surge direction as well) for inner diameter of 11 meters with DP = dipole and WT = wall thickness. The analytical value for the sloshing mode is following from equation 4.26.

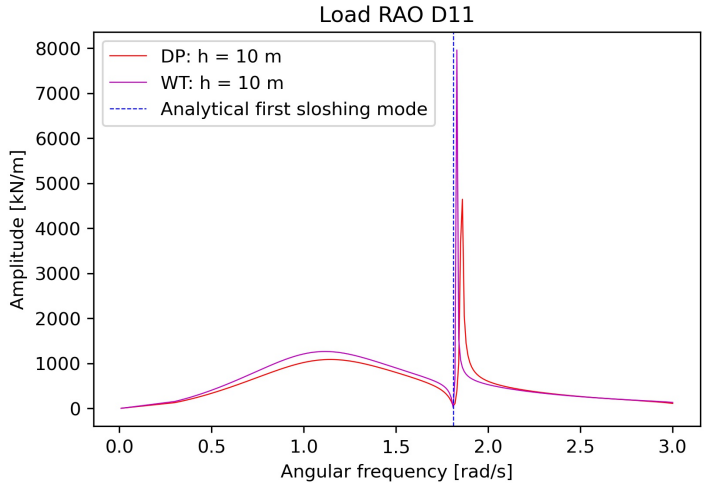

Figure 5.21: Load RAO in surge direction (wave in surge direction as well) for inner diameter of 11 meters with DP = dipole and WT = wall thickness. The analytical value for the sloshing mode is following from equation 4.26.

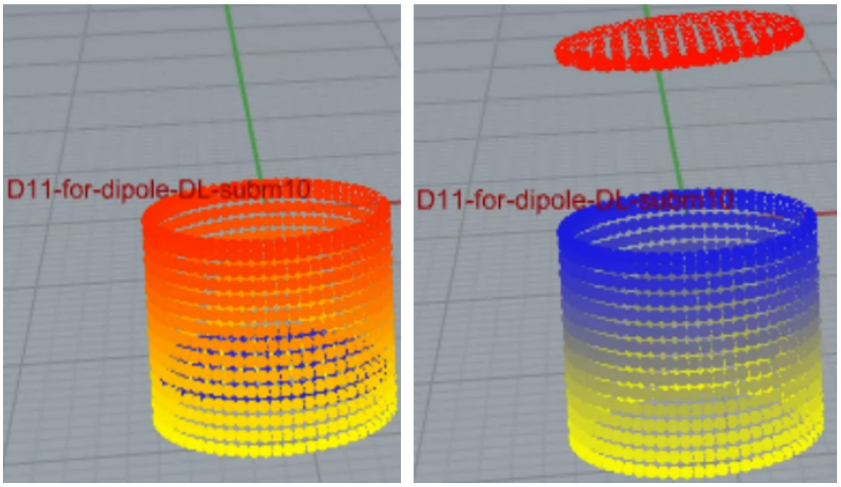

Figure 5.22: Visualization of the internal surface elevation at the piston mode natural frequency for a cylinder of $D_i = 11m$ and $h = 10m$.

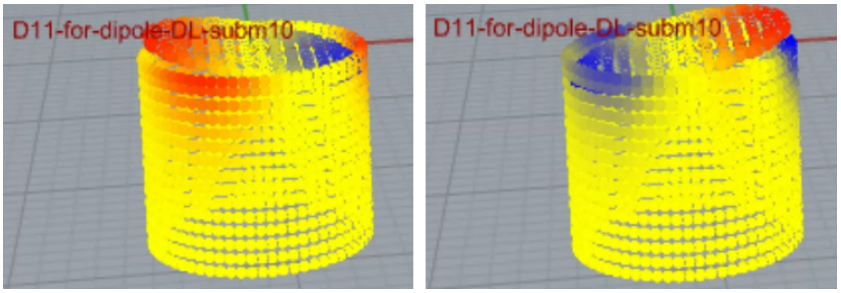

Figure 5.23: Visualization of the internal surface elevation at the first sloshing mode natural frequency for a cylinder of $D_i = 11m$ and $h = 10m$.

5.5. Inclined cylinder

Considering an inclination introduces the significance of wave directions. In this study, the installation ship is examined in head waves, aligning with the preferred operational heading of a floating installation vessel. In the LPF analysis, this implies waves approaching at a 180-degree angle, as visualized in Figure 5.24. In Figure 5.24, the ship is included purely for clarity, and it is not involved in any analysis. Therefore, shielding and other interference effects are not considered.

For cylinders penetrating the water surface at an angle, distinct resonance frequencies apply. The conventions used to characterize an inclined cylinder are outlined in Figure 4.3. An inclination angle (α) of 90 degrees corresponds to the upright cylinder, as considered thus far. For inclination angles of 90, 60, 45, and 40 degrees, the added mass and damping curves are presented in Figures 5.25 and 5.26. The submerged length, defined in Figure 4.3, is held constant at 10 $meters$, with the cylinder being rotated around a fixed point. This rotational method results in an increased draft as the angle increases, reaching a maximum at α = 90 $degrees$, where the draft equals the submerged length. It is anticipated that in the lower frequency range, piston-like resonance will occur, followed by the first asymmetric sloshing resonance at slightly higher frequencies. However, the analytical approximations valid for the vertical cylinder (i.e., α = 90 degrees) do not hold for an inclined cylinder. CFD analysis will be employed to identify the nature of the resonance, as one of the goals of the present work is to establish an analytical describtion for the inclined situation.

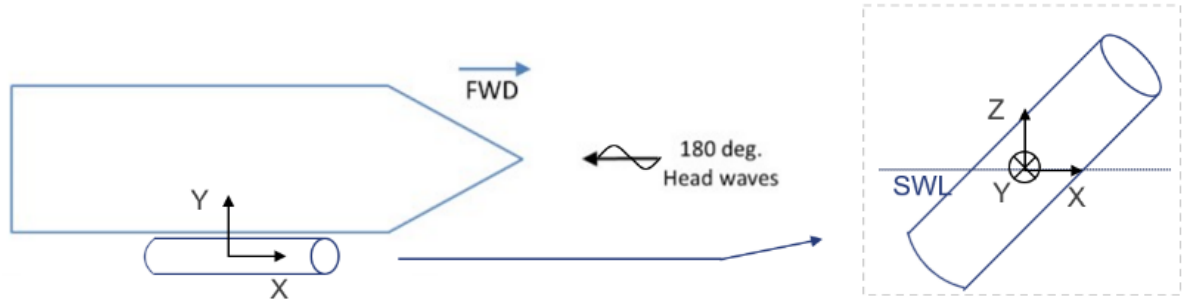

Figure 5.24: Schematic representation of the convention which is used in the inclined analysis. The ship is only included as a reference to visualize the upending procedure and is not included in the OrcaWave or ComFLOW analysis.

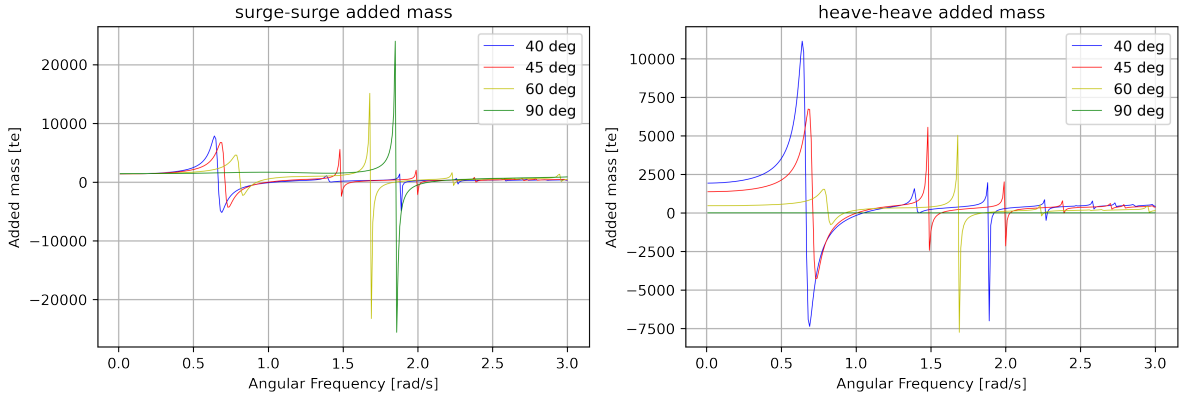

(a) Surge-surge **(b)** Heave-heave

Figure 5.25: Added mass at a constant submerged length of L_s = 10 meters and at various inclination angles.

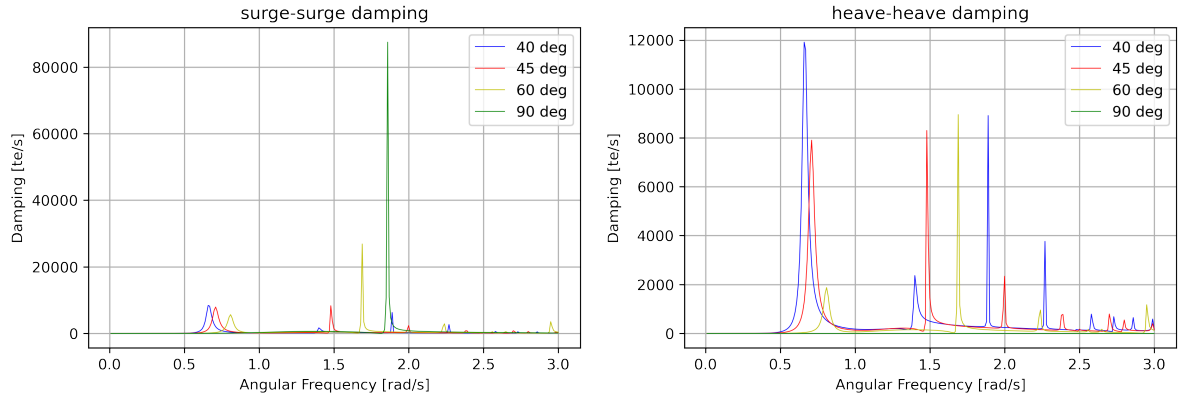

(a) Surge-surge **(b)** Heave-heave

Figure 5.26: Damping at a constant submerged length of L_s = 10 meters and at various inclination angles.

6

Computational fluid dynamics

In this chapter, Computational Fluid Dynamics (CFD) will be applied to verify the accuracy of the LPF method. CFD is a numerical approach for modeling fluid mechanics problems of high complexity, relying on extensive computational resources. It effectively addresses the nonlinear discretized differential equations related to continuity, momentum, energy, and species [3]. In contrast to linear potential flow based theory, CFD takes into account diverse factors such as viscosity, breaking waves, and turbulence by solving the Navier-Stokes equations, allowing for the simulation of unsteady three-dimensional flow. These equations, known as the governing equations of fluid motion, provide a comprehensive description of fluid behavior within a continuous framework.

The CFD code ComFLOW is a Volume of Fluid (VoF) method developed by the University of Groningen. The method has been widely utilized and verified in previous studies on sloshing loads in containment systems with predefined motions [74]. The CFD code is used to simulate both in 2D and 3D. Running the code in 3D greatly increases the simulation time. Therefore, in the present work, a 2D approach is chosen to validate the LPF results. Van der Plas [68] offers an extensive explanation of the theory supporting ComFLOW.

In the case of linear fluid behavior, it is expected that the CFD method will closely align with the LPF method. However, when higher harmonic wave frequencies are introduced, disparities emerge. The LPF method struggles to accurately represent responses at these frequencies, resulting in potential overestimation or underestimation of response amplitudes, depending on the phase differences between the harmonic frequencies. These phase differences, in turn, are influenced by the initial wave frequency. On the other hand, the CFD method has the capability to capture higher harmonic wave frequencies and may provide a closer approximation to real-world behavior.

6.1. Governing equations

In this section a brief introduction to the underlying mathematical and numerical model that serves as the foundation for the ComFLOW program provided. ComFLOW can be used to model either one-phase flow or two-phase flow. In the context of one-phase flow, water is treated as an incompressible, viscous fluid, while air is considered as a vacuum. In two-phase flow, water is still regarded as an incompressible, viscous fluid, and the modeling of air can involve selecting either an in-compressible or compressible viscous fluid representation. Two-phase flow might be of importance in case of determining the impact of breaking wave, and for example the impact of slamming, during the sloshing of the internal water column. However, in the first instance of the present study, a one-phase model is used, because it decreases the computational time. The physical parameters used are given in Table 6.1.

6.1.1. One-phase flow model

The one-phase flow model presented here is adapted from Kleefsman et al. [31]. It addresses fluid motion within a three-dimensional domain, denoted Ω, through the utilization of the Navier-Stokes equations. For water motion, where water is considered as an incompressible and viscous fluid, the Navier-Stokes equations can be simplified to:

Table 6.1: Physical parameters (one-phase flow)

Parameter	Value	Unit
Density	$1 \cdot 10^3$	kg/m^3
Viscosity	$1 \cdot 10^{-3}$	Ns/m^2
Gravity	9.81	m/s^2
Atmospheric pressure	$1 \cdot 10^5$	Pa

$$\nabla \cdot \mathbf{u} = 0 \tag{6.1}$$

$$\frac{\partial \mathbf{u}}{\partial t} + \mathbf{u} \cdot \nabla \mathbf{u} = -\frac{1}{\rho}\nabla p + \frac{\mu}{\rho}\nabla \cdot \nabla \mathbf{u} + \mathbf{F} \tag{6.2}$$

Where equation 6.1 describes the conservation of mass and equation 6.2 describes the conservation of momentum. In the equations $\mathbf{u} = (u, v, w)$ is the velocity vector, p is the pressure, μ represents dynamic viscosity, ρ stands for density, and $\mathbf{F} = (F_x, F_y, F_z)$ denotes external forces (such as gravity). These simplified Navier-Stokes equations are defined for domain Ω, which is bounded by the domain boundary $\partial\Omega$. In the case of incompressible flow, the density remains constant over time, resulting in a divergence of the velocity that is consistently zero, as indicated by the simplified continuity equation (6.1).

Boundary conditions

To solve the Navier-Stokes equations, boundary conditions are required both at the domain boundary $\partial\Omega$ and at the free surface. At solid boundaries and objects within the domain, a no-slip boundary condition is applied, ensuring that the fluid cannot penetrate the boundary and sticks to the wall due to viscosity. This condition is expressed as $\mathbf{u} = 0$ for stationary boundaries and $\mathbf{u} = \mathbf{u}_b$ for moving objects, where $\mathbf{u}_b$ represents the object's velocity. [31]

Certain domain boundaries may allow for the inflow or outflow of fluid. In our wave analysis simulations, specifically involving regular waves, we employ both inflow and outflow boundaries. In these simulations, a regular linear Airy wave is utilized. The treatment of both boundaries involves the application of generating and absorbing boundary conditions (GABC), which will be explained further in Section 6.3.3.

Free surface

When the free surface's position is defined as $s(\mathbf{x}, t) = 0$, the equation governing the displacement of the free surface can be expressed as in 6.3.

$$\frac{\mathbf{D}_s}{\mathbf{D}_t} = \frac{\partial s}{\partial t} + (\mathbf{u} \cdot \nabla)s = 0 \tag{6.3}$$

At the free surface, boundary conditions are required for both pressure and velocities. The continuity of normal and tangential stresses yields equations 6.4 and 6.5.

$$-p + 2\mu\frac{\partial u_n}{\partial n} = -p_0 + \sigma\kappa \tag{6.4}$$

$$\mu(\frac{\partial u_n}{\partial t} + \frac{\partial u_t}{\partial n}) = 0 \tag{6.5}$$

In this context, u_n and u_t represent the velocity's normal and tangential components, respectively. Furthermore, p_0 corresponds to atmospheric pressure, σ signifies surface tension, and κ refers to the overall curvature of the free surface.

Calculation of forces

Within a flow domain, the fluid exerts a force on an object located in that domain. This force can typically be broken down into two components: the pressure force and the shear force. In the ComFLOW framework, the shear force is typically disregarded due to its tendency to be significantly smaller than the pressure force. The pressure force is determined by evaluating the integral of the pressure along the object's boundary, as given in equation 6.6.

$$\mathbf{F}_p = \int_S p\mathbf{n}dS \tag{6.6}$$

For relatively basic 2D force calculations on objects it is considered sufficient to define a box area within which the pressure contributions on the solid object are integrated. Force boxes define a region in the domain where all pressure contributions on closed cell segments are integrated to determine the overall force and moments affecting the geometry.

In simulations involving moving objects, the force boxes can be adjusted to move along with the objects. Even after undergoing translation or rotation, the force box maintains its essential box shape, allowing its dimensions to adapt and change throughout the simulation.

6.2. Numerical model

6.2.1. Cell labelling

In order to conduct computer simulations of fluid flow, the flow domain Ω is discretized using a Cartesian grid featuring staggered variables. Within this grid, pressure values are defined at cell centers, while velocity components are assigned to cell boundaries. When modeling complex structures using a Cartesian grid, various types of cells emerge due to the grid's adaptability. This diversity is accommodated within the numerical method by introducing edge and volume apertures, which quantify the extent to which a portion of the cell face or cell volume is open to fluid flow. These edge and volume apertures contribute to the assignment of geometry labels to the cells, indicating their nature, such as being fluid cells, boundary cells (B), or exterior cells (X). Furthermore, to represent the free surface, fluid cells are further categorized as empty cells (E), surface cells (S), or fluid cells (F), with these distinctions being governed by free-surface labels that are updated at each time step. In Figure 6.1, we present an example of cell labeling taken from the study conducted by Kleefsman et al. [31].

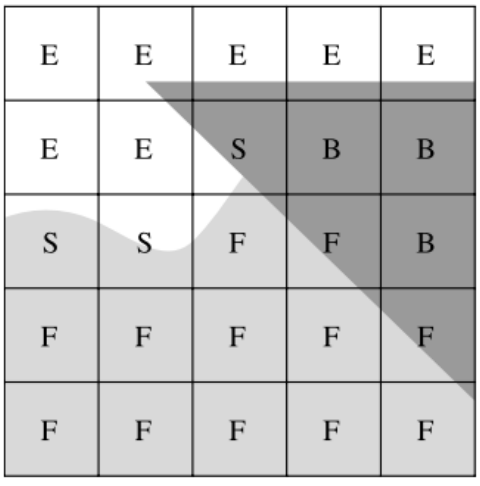

Figure 6.1: Cell labeling system: dark grey denotes solid body, light grey is liquid and white is empty. [31]

6.2.2. Discretization and solution

In order to address the Navier-Stokes equations, a process is applied to discretize these equations both in time and space. For time integration, either the first order Forward Euler method or the second order Adams-Bashforth method can be used. It is recommended to use one of these methods, but other alternatives are also acceptable, as long as the chosen method maintains consistency. Spatial discretization employs the finite volume method. There is the option to select either (second-order)

central discretization or first or second-order upwind discretization. To solve the discretized Navier-Stokes equations, a Poisson equation for pressure must be resolved at every time step, which becomes evident through the rearrangement of the discretized equations. When the GABC boundary equation is used, as in the present work, the stabilized Bi-Conjugate Gradient (BiCGSTAB) iteration method, in combination with the Incomplete Lower-Upper preconditioner (ILU(ε)) is used to solve the Poisson equation as described by Wellens [73]. Once the pressure solution is determined, the new velocity field is calculated, and thereafter, the free surface is shifted using the Volume-of-Fluid (VOF) method in conjunction with a local height function [31]. Ultimately, the time step is adapted in accordance with the CFL (Courant-Friedrichs-Lewy) condition. The CFL number is computed as in equation 6.7.

$$CFL = \max_{i,j,k} \left(\frac{|u_{ijk}|\,\delta t}{h_{x,i}} + \frac{|v_{ijk}|\,\delta t}{h_{y,j}} + \frac{|w_{ijk}|\,\delta t}{h_{z,k}} \right) \tag{6.7}$$

Here, u, v and w represent velocity components, while h_x, h_y, and h_z represent mesh sizes in their respective directions. If the calculated CFL-number exceeds the user-defined threshold (CFL_{max}) from the input file, the time step is reduced. Conversely, if the computed CFL-number remains below (CFL_{min}) for 10 consecutive time steps, the time step is doubled.

6.2.3. Initial settings

In this section some important initial settings for the ComFLOW simulation are given. For a more elaborete explanation of these settings reference is made to the ComFLOW program documentation [58].

Waves

For the simulation of incoming waves, Airy waves are used, aligning with the wave theory utilized in the LPF analysis. The simulations start with still water and ramping is used for a smooth startup of the simulation. Current is intentionally excluded from these simulations, as it is not a parameter taken into account in the current research.

Turbulence

In the initial stages of this study, turbulence is not expected to exert a substantial impact on the hydrodynamic response because the research primarily concentrates on large-scale phenomena like wave loads and internal forces. Therefore, turbulence models are not incorporated into the simulations.

Diffusion

The LS-STAG discretization scheme is employed due to its capability to provide a more precise estimation of viscous stresses within cells intersected by the geometry. Consequently, it is the recommended choice for general applications.

Convection

When discretizing the momentum equation, particularly for convection, there are two primary discretization options available. One choice is the combination of a first-order upwind scheme and a second-order central scheme, while the other option is a second-order upwind scheme. When employing the first-order upwind scheme, it is possible to introduce artificial diffusion to enhance the stability of the discretization process. For the present work, the first-order upwind scheme is used with an artificial diffusion factor of 1.0, since this yields the most stable solution.

Fill boxes

In order to measure the water height in grid-aligned direction, fill boxes can be used. In case of non-inclined geometries, fill boxes can surve as an appropriate measurement tool for the local water height at a specific location. However, for accurate water height calculations it is recommended to use relative water height lines, because these provide a more accurate representation of the actual liquid distribution [58]. In the current study, the preferred method for measuring water height is the use of fill boxes due to their ease of use and sufficient accuracy.

In section 6.5.1, the geometry undergoes forced motion. In such cases, it is feasible to define moving fill boxes. However, caution should be exercised when utilizing this feature, as the fill boxes are constrained to the grid, potentially leading to discontinuities in time. Again, in certain applications it is recommended to use relative water height lines.

6.3. Validation of the CFD code ComFLOW

First, the CFD simulation is validated in a 2D setup. In this configuration, a monopile is represented by two walls, and the distance between the walls corresponds to the inner diameter of the monopile. However, there is a lack of experimental data on the 2D resonance for a fixed open-ended cylinder exposed to regular waves. To address this, the ComFLOW numerical model is validated using physical experiments conducted by Saitoh et al. [62] and numerical investigations by Lu et al. ([42],[43]). These same studies are also used for validation by Gao et al. [19].

In the research by Gao et al. [19], a 2D numerical wave tank based on OpenFOAM® is utilized to study the resonant water motion occurring within a narrow gap between two identical fixed boxes positioned side by side. All dimensions and the wave height are set in accordance with the studies by Saitoh et al. [62] and Lu et al. ([42],[43]). For the present work, the same validation method is used.

A sketch of the 2D numerical computational domain used in the simulations is depicted in Figure 6.2. For the validation process, the wave tank dimensions and the values for the breadth (B), box height (H), box draught (h), gap width (B_g), water depth (D), air depth (D_a) and wave height (H_0) are given in Table 6.2.

The wave frequency, ω, considered in the simulations ranges from 3.866 rad/s to 6.957 rad/s. This corresponds to the dimensionless wavenumber, kD, ranging from 1.0 to 2.5. The wave number and the wave frequency are related through the dispersion relation (equation 6.8).

$$\omega^2 = gk\text{tanh}(kD) \tag{6.8}$$

In the research of Saitoh et al. [62] it is derived through the conservation of energy that for a situation as in Figure 6.2, the natural frequency of the fluid in the gap can be computed using equation 6.9 [50].

$$\omega_g = \sqrt{\frac{g}{\frac{B_g B}{D-h} + h}} \tag{6.9}$$

Equation 6.9 shows that the gap resonance only depends on the geometrical parameters of the system. This is also the case for the Molin [48] approximation for the piston mode natural frequency inside a moonpool (as given in equation 4.5). In comparison to the validation of the resonance behavior of the internal water column of the monopile, which will be addressed in Section 6.4, it is important to understand that the water depth influences the gap resonance in the wave flume shown in Figure 6.2. In Figure 6.2, G1 and G2 indicate the numerical wave gauges in front of the geometry and in the gap between the two geometries, respectively.

In the ComFLOW numerical method, the surface elevation is measured by monitoring the fill ratio of a small part of the domain. The water height is calculated in grid-aligned directions, e.g. a vertical fill box which encompasses precisely one column of grid cells. As a result, it serves as an approximation for the local water height. The results from the fill box inside the gap is compared with a fill box at the same location, when no geometry is present. All other variables are kept equal in both simulations. By comparing the two simulations, the effect of the presence of the boxes on the water level in the gap can be analysed.

Figure 6.3 shows the correlation between the dimensionless wave height in the gap (G2) and the incoming wave number. In addition to the present study, also the experimental restults by Saitoh et al. [62], and the numerical simulations of Lu et al. ([42],[43]) and Gao et al. [19] are visualized in the graph.

From Figure 6.3 it can be concluded that the amplification of the free-surface within the gap, as projected by the ComFLOW model, follows the same trend as the results from the previous works. The non-dimensional wave height peaks at the same frequency as the other works and thus the resonance frequency matches. However, the magnitude of the present work does not match the comparison works. As explained by Lu et al. [43], it is important to highlight that accurately determining the resonant frequency and the associated resonant wave height in the narrow gap is challenging when employing the viscous fluid model. This is due to the necessity of a very small frequency increment to achieve high resolution. Hence, in the present validation, when referring to the resonance frequency and the

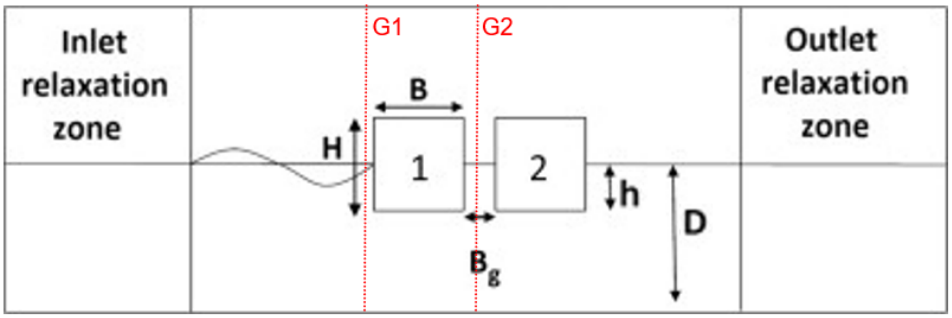

Figure 6.2: Sketch of the 2D numerical simulation domain. [50]

Table 6.2: Dimensions of the numerical domain.

Wave tank	L	8.5	m
	H	0.8	m
Box	H	0.5	m
	B	0.5	m
	h	0.25	m
Gap width	B_g	0.05	m
Water depth	D	0.5	m
Air depth	D_a	0.3	m
Wave height	H_0	0.024	m

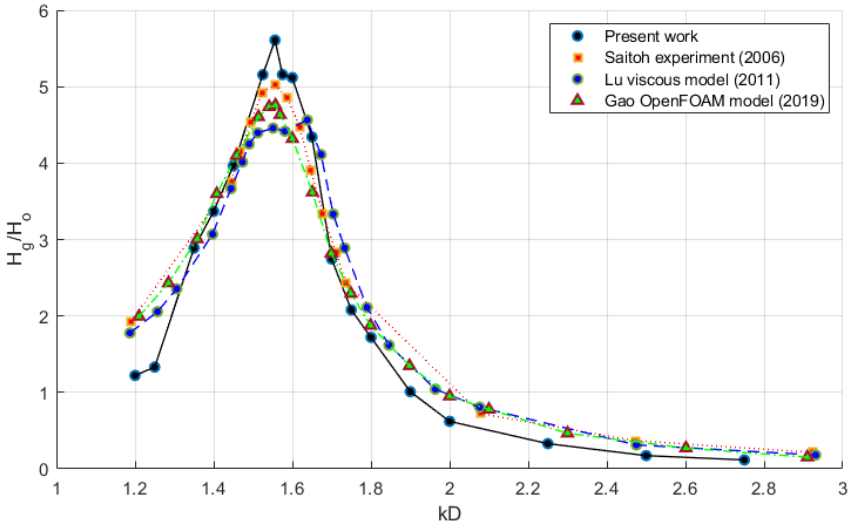

Figure 6.3: The amplification curve of the free-surface elevation in the gap between the two boxes, subjected to regular waves of waveheight H_0 = 0.024 m and various frequencies.H_g is the wave height in the gap (gauge G2 in Figure 6.2) and kD is the wave number.

associated resonant wave height associated to the ComFLOW model, we generally mean values that are within acceptable tolerance when compared to the other works.

6.3.1. Phase difference

In the work by Tan et al. [67], a method is described to find the phase angle between the oscillating motion in the gap and its excitation. The oscillating motion in the gap is measured with a wave gauge in the gap and the excitation frequency is measured outside of the geometry, at the incoming wave side.

In the study conducted by Tan et al. [66], it becomes evident that at the gap resonance frequency, there is an observable phase difference of approximately $\pi/2$ between the incoming wave and the oscillatory motion within the gap.

Additionally, when considering different incoming wave frequencies outside of the resonance conditions, the response amplitude within the gap exhibited a comparable magnitude to that observed at the front location of the leading box. In these cases, phase differences of approximately π and zero were observed. The results obtained in the present work exhibit the same outcomes, as depicted in Figure 6.4. The value for the resonance frequency derived from equation 6.9, $\omega_g = 5.294 rad/s$, agrees well with the $\omega_g = 5.285 rad/s$ at which resonance occurs according to the ComFLOW model. As visualized in Figure 6.4, at this frequency the surface elevation in the gap is $\pi/2$ out of phase with the incoming wave.

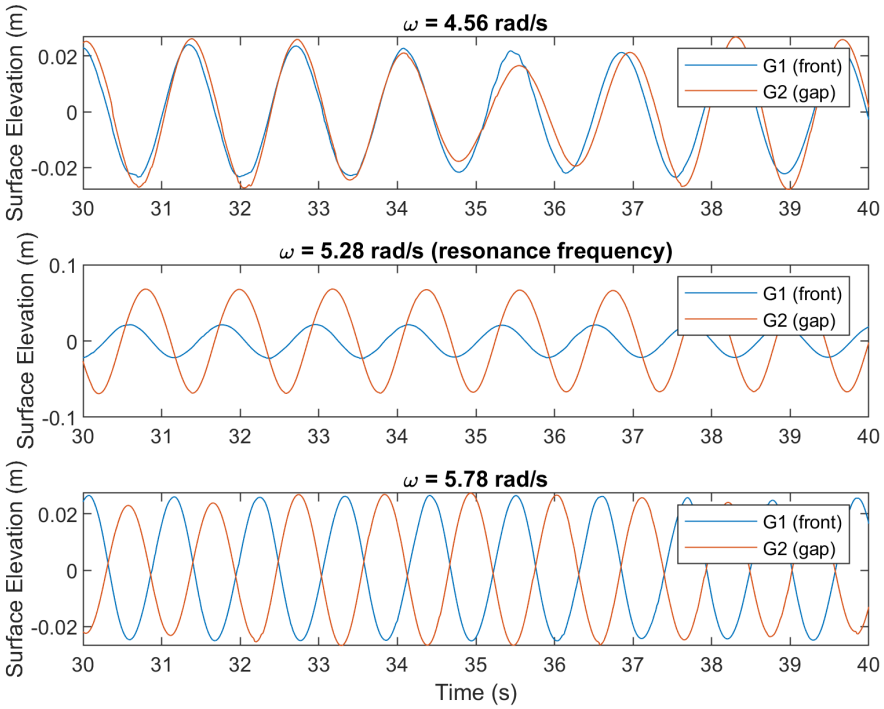

Figure 6.4: Time domain plot of the free-surface elevation at wave gauges G1 and G2 (see Figure 6.2) for different wave frequencies ω.

6.3.2. Grid resolution

The grid size is of importance for an accurate simulation of the waves. As described in the ComFLOW documentation [58], when an undisturbed wave is simulated, the rule is to use at least 60 grid cells per wavelength and 6 grid cells per wave height. For high waves, the number of cells per wave height should be increased to at least 10. For deep water simulations, this means a lot of cells are needed in the vertical direction. To counteract this consequence, grid stretching can be applied in vertical direction around the water surface, increasing the amount of cells in the region of the waves.

Before the results from ComFLOW are compared to the results of previous studies, grid dependence checks are carried out. To assess how the simulation outcomes are affected by the grid density, three grid types are compared: course, intermediate and fine. Regardless of the grid density, grid refinement is applied. The refinement of the grid is such that its density rises from the in- and outlet boundaries towards the domain's center, where the boxes are located. The maximum density is located within the

gap area, where the piston like water movement is expected.

In addition to grid refinement, we also apply grid stretching in the vertical direction. The introduction of grid stretching allows us to reduce the number of grid cells in the vertical dimension while still maintaining a minimum of 6 cells for wave height calculations. The grid density increases closer to the surface level and decreases towards the top and bottom of the domain.

In Appendix A, in Figure A.1, a surface elevation measurement in the center of the gap is provided for different grid sizes. The surface elevation prediction obtained from the 400x1x40 grid closely matches the results obtained from the finer 400x1x200 grid in the vertical direction. Similarly, in the horizontal dimension, the 400x1x40 grid exhibits strong agreement with the finer 512.5x1x50 grid. As a result, for the sake of computational efficiency, the intermediate grid (400x1x40) will be utilized for all subsequent simulations in the ComFLOW validation.

6.3.3. Generating and absorbing boundary condition (GABC)

The length of the wave tank in the present work is different from the work by Gao et al. [19]. In contrast to their work, where a wave tank with a length of 18.5 meters was utilized, we have opted for a reduced length of 8.5 meters. The reason behind this modification lies in the implementation of the non-reflective generating boundary condition (GABC) in ComFLOW. The GABC is implemented to eliminate wave reflection from the domain boundaries and create non-reflective conditions, which helps to simulate wave propagation more accurately. The GABC is used at the inflow ends (where waves are generated) and outflow ends (where waves leave the domain). The GABC is defined by specifying certain coefficients in the ComFLOW input file. A thorough description of the GABC is presented in Chang et al. [9].

The GABC is defined by specifying certain coefficients in the input file. The coefficients control the behavior of the boundary condition and how well it approximates the dispersion relation of the waves.

- Coefficients a_0, a_1, and b_1 are used to approximate the linear dispersion relation of the waves:

$$c_a = \sqrt{gh}\frac{a_0 + a_1(kD)^2}{1 + b_1(kD)^2} \tag{6.10}$$

- Coefficients kD_1 and kD_2 are associated with wave number values, and their specific values depend on whether the waves are regular or irregular.
- Coefficients $alfa_1$ and $alfa_2$ determine the angle at which the GABC provides the best absorption, and their values depend on the wave type (regular or irregular).

The coefficients a_0, a_1, and b_1 must satisfy certain requirements to ensure stability. Properly chosen coefficients lead to better approximation and less wave reflection. To find the optimal coefficients for a specified range of kD values a coefficient optimization function is used. [58]

The use of the GABC eliminates the requirement for extensive inlet and outlet relaxation zones within the domain, making it feasible to achieve the shortened length of the numerical wave tank.

6.4. Fixed geometry with regular incident waves

Computational Fluid Dynamics (CFD) simulations are utilized to investigate the behavior of surface water inside the cylinder near resonance frequencies. Initially, an analysis is conducted to identify the characteristics near the resonance frequency. This analysis involves studying both a fixed geometry exposed to regular incident waves (this section, 6.4) and a geometry forced to oscillate in calm water (Section 6.5). Surface elevation measurements are performed using numerical wave probes, and pressure is measured on the geometry. The CFD simulations are carried out in a 2D domain to limit the computational effort required for simulation, aiming to sufficiently identify the most important resonance characteristics. Subsequently, the LPF results from OrcaWave are compared to the CFD results.

Post processing

To derive experimental results from the collected data, various Matlab scripts are established to process the data. Please note that in all time series analyses in this research, the initial and final oscillations, where transient effects are present, are excluded from the time series analysis.

Vertical wave elevation

In the analyses of both upright and inclined cylinders, the wave probe measuring internal wave elevation is consistently aligned with the cylinder. Consequently, for inclined cylinders, the internal wave elevation recorded by the wave probe needs to be multiplied by the sine of the inclination angle (θ) to determine the vertical wave elevation. Throughout this report's analysis, the vertical wave elevation is utilized unless specified otherwise.

6.4.1. Piston mode - 2D - Upright

To be able to compare the results of CFD and LPF, the geometry in the CFD has the same dimensions as the LPF geometry with source panels, i.e. D_i = 11 meters, D_o = 12 meters and a submergence h of 5 and 10 meters. For the 2D CFD, the same conventions are used as in 4.1. The locations of the wave gauges and the direction of the incoming wave are added to Figure 4.1 and presented in Figure 6.5. In Section 6.3.2, the grid resolution convergence is explained, which is also used for the piston mode. The corresponding graph illustrating this concept can be found in Appendix A, Figure A.2.

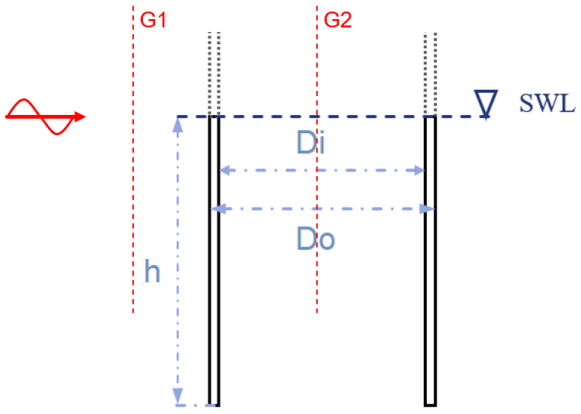

Figure 6.5: Wave gauges and wave direction used in the analysis added to conventions of Figure 4.1.

The Molin [48] approximation for the piston mode natural frequency (equation 4.5) holds for a 2D geometry. Therefore, the piston mode natural frequency from Table 5.1 is used as the best first guess for determining the piston mode with ComFLOW. It is expected that the piston mode resulting from the ComFLOW simulation will be in the vicinity of this frequency. However, because the Molin approximation assumes linearity, the piston mode resonance frequency from ComFLOW might deviate.

In Table 5.1, in Section 5.2, it becomes clear that the expected piston mode natural frequency based on the analytical approximation is in line with the LPF results. The results from the 2D ComFLOW simulations are given in Figures 6.6 and 6.7.

In Figures 6.6 and 6.7, the upper plot shows the relative wave height, H_g/H_0 (the wave height in the gap (H_g) divided by the incident wave height (H_0)), as a function of the non-dimensional incident

wave frequency Λ ($= \omega^2 * D_i/g$). The lower plot shows the phase difference between the wave gauge in front of the geometry ,$G1$, and inside the geometry,$G2$, (as visualized in Figure 6.5), as a function of non-dimensional incident wave frequency Λ. The phase difference is determined in the same way as explained in Section 6.3.1.

In Figure 6.6, the submergence of the 2D geometry is 5 meter and represented by blue lines. In Figure 6.7, the submergence is 10 meter and represented by green lines. At both submergence's analysed, the incident wave height (H_0) is 0.2 meter.

The maximum relative wave height, H_g/H_0, is anticipated to occur at resonance. It is expected that this peak will occur when there is an approximate 90-degree phase difference between the wave oscillations measured at $G1$ and $G2$. Furthermore, the phase difference is expected to gradually approach zero and 180 degrees as the incident wave frequencies approach zero and infinity, respectively [19]. From these results it can be concluded that the piston mode behaviour as explained by Gao et al. [19], for two identical fixed boxes positioned side by side, is also valid for two slender bodies with a larger gap.

In all plots, the non-dimensionalized piston mode resonance frequency, following from Molin's approximation and the 2D LPF analysis are indicated by the red and black dotted line respectively.

In Section 5.2 it was established that Molin's approximation closely matches the resonance frequency following from the LPF model for the 3D cylinder. The discrepancy between the resonance frquency found with the Molin approximation and the LPF model for a 2D structure should be sought in the fact that the 2D Molin approximation, which is designed for a moonpool, assumes a small $D_i/(wall\ thickness)$ ratio [33]. This ratio is not small for the 2D monopile representation.

The piston mode resonance frequency obtained from the ComFLOW simulations is slightly lower than following from the LPF analysis. As explained in 4.2.2, it is mainly the added mass term which determines the resonance frequency. However, if there is significant viscous damping, this can also influence the piston resonance frequency.

The discrepancy between the numerical values obtained from the ComFLOW model and those derived from the analytical approximation can be attributed to damping. Two types of damping are distinguished in this context. The first type is the radiation damping incorporated in the LPF method, consistent with Molin's approximation. This damping arises from the piston-mode motion of the water inside the moonpool, which interacts with the exterior domain by generating waves (radiation). The second type of damping is viscous damping caused by flow separation at the inlet (bottom edges) of the geometry and frictional stresses along the geometry. In Figure 6.8a, the effect of flow separation is illustrated and Figure 6.8b shows the occurrence of this phenomena in the ComFLOW calculation. The fluid experiences separation at the sharp corner, leading to the generation of vorticity that is released into the main body of the fluid [32]. The circulation is approximately 45 degrees out-of-phase with the ambient flow, such that the circulation creates a back-flow, acting as a damping effect.

According to Kristiansen's work [32], radiation damping is very small compared to viscous damping when the piston mode is excited. The dominance of viscous damping at resonance explains the large piston amplitude at piston mode resonance in the LPF method (where viscous damping is not included) and the discrepancy between the piston mode resonance frequency in the LPF (and Molin) method and the CFD, where both radiation damping and viscous damping is accounted for.

Another possible explanation could be that a significant portion of the incident regular wave is reflected by the geometry in the 2D domain. However, applying an incident wave with a lower wave height did not change the resonance frequency observed in the CFD analysis. Therefore, wave reflection is not expected to be the reason for the resonance frequency discrepancy between methods.

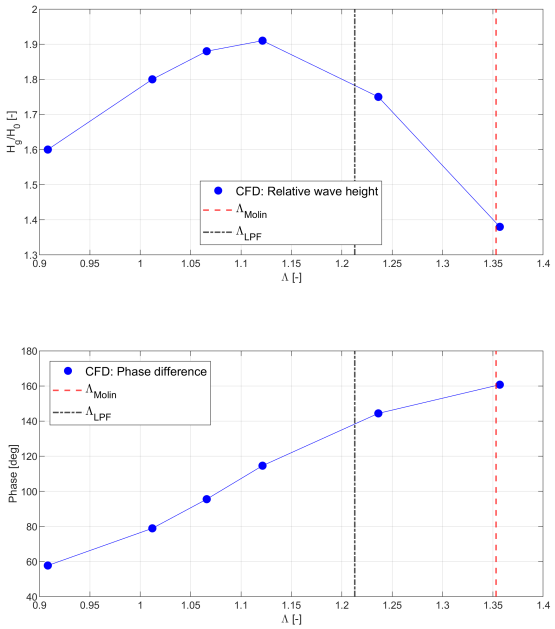

Figure 6.6: The upper plot shows the relative wave height, H_g/H_0, as a function of the non-dimensional incident wave frequency Λ ($= \omega^2 * D_i/g$). The lower plot shows the phase difference between $G1$ and $G2$ (Figure 6.5), as a function of non-dimensional incident wave frequency Λ. Submergence of the geometry (h) is 5 meters. The piston mode resonance frequency from Molin and the LPF method are indicated.

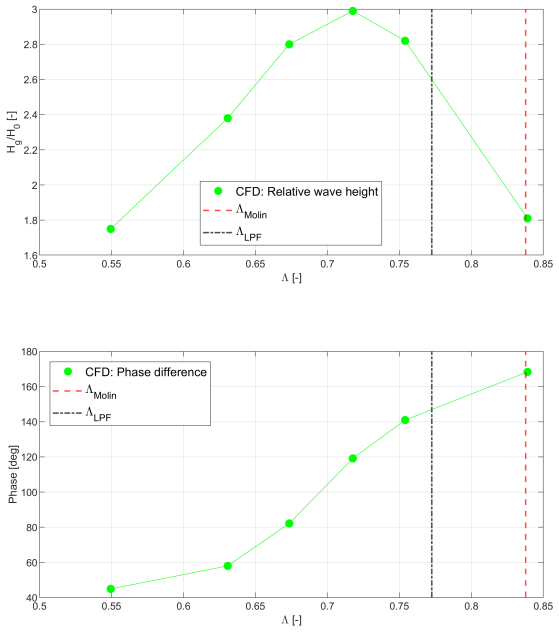

Figure 6.7: The upper plot shows the relative wave height, H_g/H_0, as a function of the non-dimensional incident wave frequency Λ ($= \omega^2 * D_i/g$). The lower plot shows the phase difference between $G1$ and $G2$ (Figure 6.5), as a function of non-dimensional incident wave frequency Λ. Submergence of the geometry (h) is 10 meters. The piston mode resonance frequency from Molin and the LPF method are indicated.

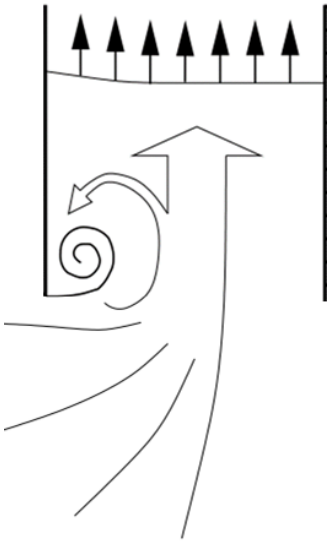

(a) Schematics of the effect of circulation for a 2D geometry. This figure is a variation on the schematic figure given by Kristiansen [32].

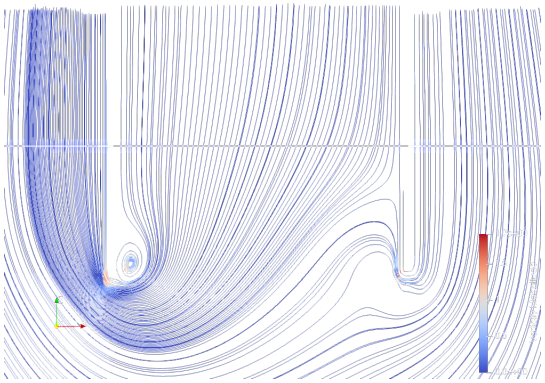

(b) Visualization of the vorticity magnitude from 2D ComFLOW CFD simulation. Geometry submergence,h = 5 meters.

Figure 6.8: Schematic and CFD visualization of the effect of circulation due to flow separation.

6.4.2. Piston mode - 2D - Inclined

In Section 4.2, the expectation is presented that the piston-mode natural frequency will decrease as the inclination with respect to the horizontal decreases. This assumption is case the submerged length remains constant. This hypotheses is tested for the 2D representation of a monopile with a constant submerged length L_s of 10 meters. To test this hypothesis, we utilize a 2D representation of a monopile with a fixed submerged length L_s of 10 meters, similar to the model presented in Section 5.5. However, the analysis in CFD is conducted for a 2D geometry, and the incident waves are following waves (see Figure 3 for the convention). This is necessary, since the piston resonance is not as effectively excited when dealing with head waves in the 2D CFD method.

In Figure 6.9 the relative wave height for the 45 degrees inclined geometry is given. The H_g is measured between the walls, and H_0 is in incident wave height. In the figure the piston mode resonance frequency for the upright geometry following from CFD is given as the green dotted line. Only the frequency is given, since the magnitude can not be compared directly, as the incident wave height, H_0, in the inclined simulations is 1 meter, which is significantly larger than the H_0 of 0.2 meter in the upright simulations. The anticipated decrease in piston mode resonance frequency due to the inclination is reflected in the results.

In Figure 6.10 a visualization is given of the piston mode resonance for the inclined situation. In Figure 6.11 a visualization of the presence of vorticity around the bottom edges is given. The magnitude of the vorticity is much higher than for the upright case in Figure 6.8b, because the wave height in the inclined analyses is 5 times greater, thus the waves contain much more energy. Therefore a comparison between Figure 6.11 and Figure 6.8b is not relevant.

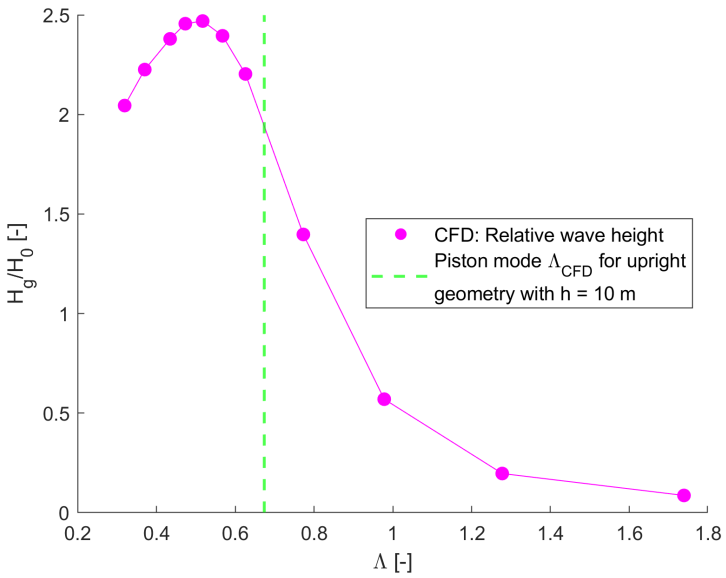

Figure 6.9: Relative wave height, H_g/H_0, as a function of the non-dimensional incident wave frequency Λ ($= \omega^2 * D_i/g$). The piston mode resonance frequency for the upright geometry following from CFD (from Figure 6.7).

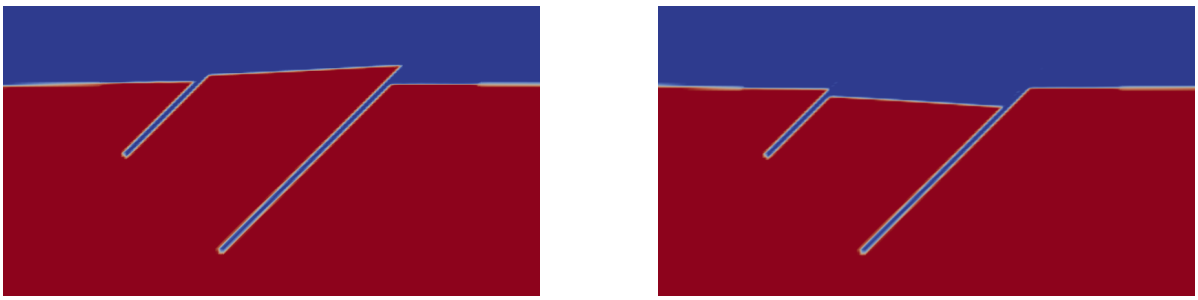

(a) Peak in the sinusoidal motion

(b) Trough in the sinusoidal motion

Figure 6.10: Visualization of the free surface motion at piston mode resonance frequency Λ = 0.517.

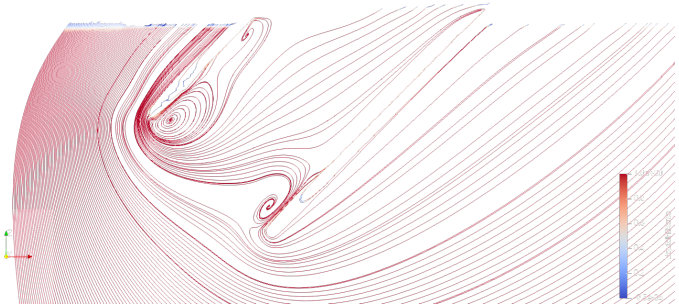

Figure 6.11: Visualization of the vorticity magnitude from 2D ComFLOW CFD simulation. Geometry submerged length, L_s = 10 meters and inclination angle α = 45 degrees and incident wave frequency Λ = 0.517.

6.5. Geometry forced to oscillate in calm water

6.5.1. Sloshing mode - 2D - Upright

To investigate at which frequencies the first asymmetric sloshing modes occur, forced motion of the 2D geometry in still water is employed rather than initiating the sloshing motion with an incident wave. The geometry is given a sinusoidal forced surge excitation at different frequencies, to investigate whether the analytically determined sloshing frequencies equal those following from the CFD model.

The structure is forced to oscillate horizontally. The focus is on the excitation frequency, ω, close to the lowest natural sloshing frequency. The sinusoidal surge excitation is given in equation 6.11.

$$\eta_1(t) = \eta_{1a} \cdot \cos \Omega t \tag{6.11}$$

In equation 6.11, η_{1a} and Ω are the excitation amplitude and frequency, respectively.

Finding the natural sloshing modes using forced oscillation in still water requires some considerations. First, it is important to determine whether the simulation is initiated from a complete stop or if an initial time (or phase shift) is chosen that corresponds to a small velocity for a smooth start. Furthermore, as found by Faltinsen and Timokha [17], increasing the forcing amplitude and the corresponding response of the primary excited mode or decreasing the submergence of the geometry can lead to the amplification of higher modes, thereby challenging the single-dominant modal system. Faltinsen and Timokha [17] extensively analyze these modes of amplification for both 2D and 3D sloshing. To facilitate a valid comparison between LPF and CFD, the forcing amplitude is maintained at a low level. The ratio of the forcing amplitude-to-breadth (η_{1a}/D_i) is equal to 0.0091. Note that D_i is used in 2D as the length between the two walls. This ratio in the specific context of this research does not lead to chaotic surface water behaviour, which makes it possible to draw a comparison between the LPF and CFD results. This ratio is kept constant throughout the CFD work.

Grid resolution

The optimum grid for the forced oscillation analysis is found by striking a balance between a fine enough grid and a reasonable computational effort while ensuring a file size that can be handled by the storage capacity. A refinement ratio of 2, which ensures a smooth transition in grid resolution, is applied on the grid cells at and around the geometry. This refinement ratio is recommended and extensively tested for ComFLOW. Moreover, the local refinement is supplemented by grid stretching, in order to obtain faster resolution changes. The measured force on the geometry is compared for different grid sizes. The results of this check are presented Appendix A, Figure A.3. Taking both accuracy and computational effort into consideration, the refined and stretched grid of 200×100 is sufficient for this research. The grid is given in Figure 6.12.

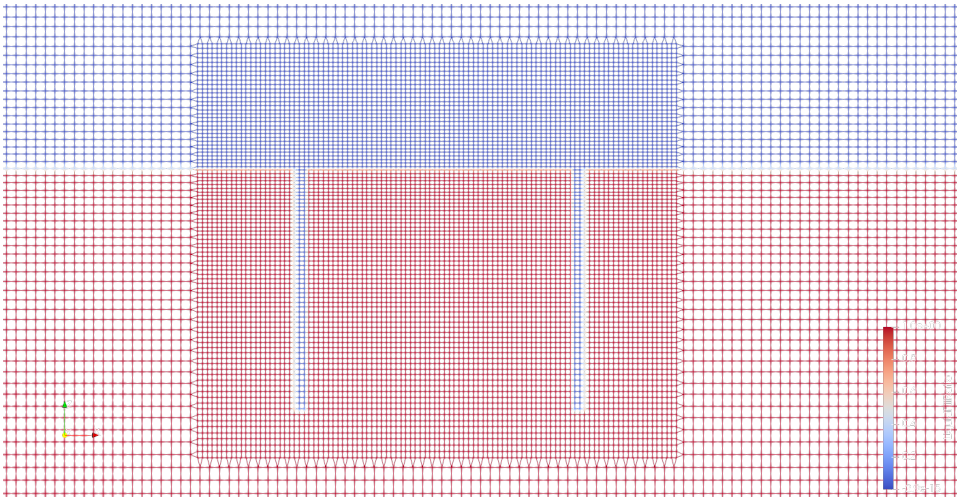

Figure 6.12: Grid resolution used for the 2D forced oscillation analysis. Grid refinement around the geometry and stretching in z-direction from the still water line is visible. Red indicates liquid and blue indicates no-liquid.

Time domain

The surface elevation in the forced oscillation analysis is measured at the same location as for the incident wave analysis, thus at side 1 (see Figure 4.5). In figure 6.13 and 6.14 the result of the numerical wave probe measurement for the forced motion analysis is given, for a vertical geometry with a submergence of $h = 5m$ and $h = 10m$ respectively, and a motion amplitude of $\eta_{1a} = 0.1m$ at various frequencies.

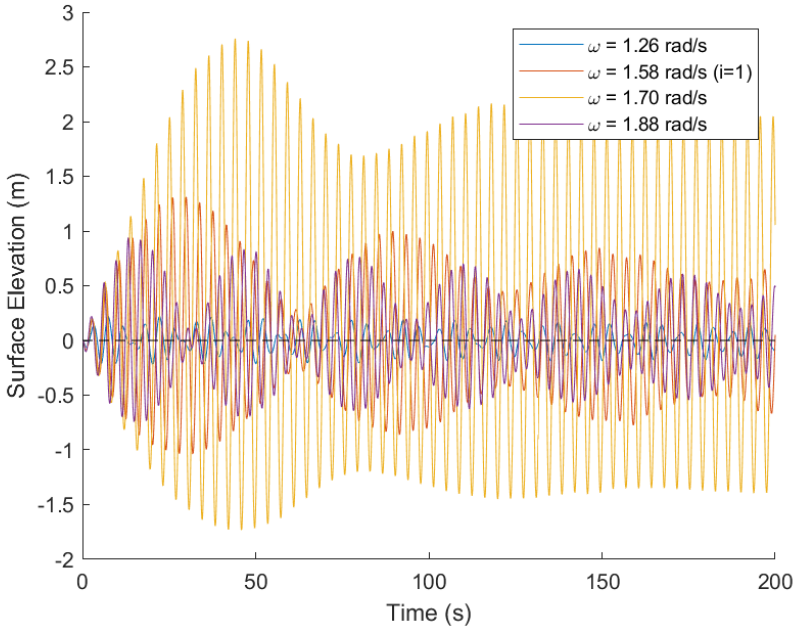

Figure 6.13: Surface elevation on side 1 of the geometry, with a submergence of $h = 5m$ and a motion amplitude of $\eta_{1a} = 0.1m$ at various frequencies (i = 1 indicates analytically determined sloshing frequency).

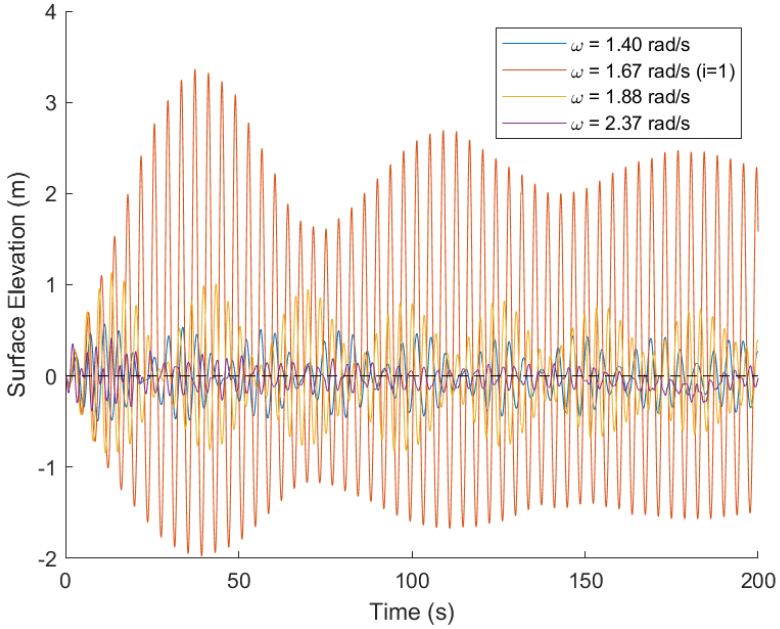

Figure 6.14: Surface elevation on side 1 of the geometry, with a submergence of $h = 10m$ and a motion amplitude of $\eta_{1a} = 0.1m$ at various frequencies (i = 1 indicates analytically determined sloshing frequency).

To accurately determine the first sloshing mode's natural frequency using 2D CFD forced motion analysis, it is necessary to run simulations with a larger number of frequencies than presented in Figures 6.13 and 6.14. This expanded analysis will help ascertain if the resonance frequencies observed in the 2D CFD analysis systematically differ from the analytically approximated frequencies. In the following section this frequency domain analysis will be carried out.

Frequency domain

In order to explain the behavior observed in Figure 6.13 and Figure 6.14, the data is analysed in the frequency domain. This method proves valuable as it offers insights into how a system reacts to various frequencies, particularly when investigating the dynamic behavior or resonant frequencies of the system. For the frequency domain analysis of the 2D forced motion simulations a submerged length (L_s) of 5, 10 and 15 meters is used. For the upright (i.e. 90 degrees inclination) structure, the submerged length is equal to the draft ($L_s = h$).

The CFD simulations operate in the time domain, therefore the results in frequency domain are obtained after multiple post-processing steps. First, the time domain is analyzed, starting from a point where a stable situation has begun. The initial portion of the time series is characterized by transient effects, and therefore is excluded. This specific analysis focuses on the time domain range from 300 to 400 seconds. Next, the force on the geometry is filtered to eliminate irregular frequencies in the response caused by numerical pressure peaks.

Filtering force data

The Savitzky-Golay filtering method [63] is employed to smooth out irregularities in the response. The employed method for peak filtering should be approached with caution to prevent smoothing-out genuinely existing flow characteristics. The occurrence of irregularities in the force data can be attributed to various factors. To enhance the accuracy of the CFD results, adjustments can be made to the input script. Various reasons for irregularities, and changes in the input script to address them, are listed below:

1. **Mesh Quality:** The quality of the mesh used in CFD simulations plays a crucial role. Poorly structured or unstructured meshes, especially near boundaries or critical regions, can lead to inaccuracies and irregularities.

   Address: Ensure that the mesh is well-structured and has sufficient resolution, especially in critical regions.
2. **Boundary Conditions:** Incorrectly specified boundary conditions or improper treatment of boundaries can cause irregularities. Ensure that the boundary conditions are accurately defined and represent the physical system.

   Address: Check whether the boundary conditions accurately represent the physical system.
3. **Numerical Instabilities:** Numerical methods used in CFD simulations can become unstable under certain conditions. This instability may lead to erratic behavior in the simulation results.

   Address: Adjust numerical schemes, decrease time step size, and monitor for stability issues during simulations.
4. **Time Step Size:** In time-dependent simulations, the choice of the time step size can impact the stability and accuracy of the solution. An inappropriate time step size may lead to irregular oscillations or divergence.

   Address: Experiment with different time step sizes, perform sensitivity analyses, and choose a time step that balances accuracy and stability.
5. **Solver Convergence:** Insufficient convergence of the solver can result in inaccurate and irregular results. Monitoring convergence criteria and adjusting solver settings may be necessary.

   Address: Increase the number of iterations, tighten convergence criteria, and consider using more advanced solvers if available.
6. **Physical Assumptions:** Assumptions made in the simulation, such as neglecting certain physical effects or simplifying geometry, can introduce irregularities.

   Address: Reevaluate assumptions, consider more detailed models, and compare results with simulations that include additional physical effects.

An example of force data with and without filtering of the irregularities is visualized in Figure 6.15. In Appendix D examples are given of how the filtering works for multiple excitation frequencies.

In addition to the general factors contributing to irregularities in the CFD results, there are also specific considerations pertinent to the pressure peaks observed, which are associated with the models used in this research. Iwanowski et al. [23] found, in their study using ComFLOW, that pressure spikes

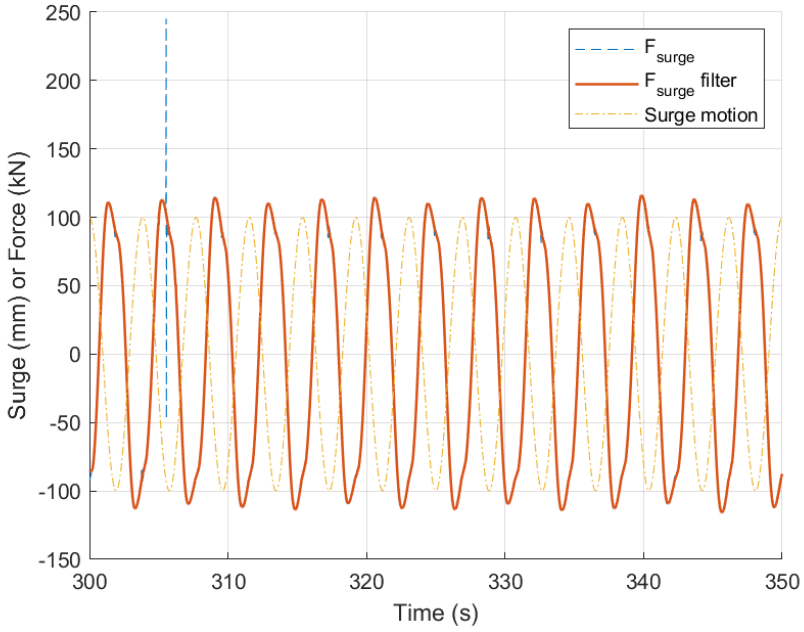

Figure 6.15: Time domain plot of the surge forced oscillation test in a 2D ComFLOW simulation with an amplitude of oscillation η_a = 0.1 m and a excitation frequency Ω of 1.63 rad/s.

are especially likely to occur in cells partially occupied by the immersed geometry, specifically in regions where the fluid's free surface has just appeared or dissipated. For the considered forced motions problem, this phenomenon occurs in the majority of cells surrounding the geometry in close proximity to the free surface. Furthermore, in the study conducted by Brodtkorb [6], employing ComFLOW, it is emphasized that numerical noise in pressure signals is more pronounced when fluid cells contain only a small portion of solid geometry. Brodtkorb [6] gives multiple mitigation measures. To reduce the magnitude of the peaks, larger time steps should be employed. Furthermore, the incorporation of a two-phase flow model may serve to diminish pressure peaks. The numerical simulation is also less susceptible to pressure peaks when the geometry aligns with the fluid mesh. This latter effect becomes apparent when examining inclined geometries, where the occurrence of numerical pressure peaks is more pronounced, as will be observed in Section 6.5.3 .

The mean values of the force amplitude are determined from the time series using equation 6.12. For an excitation frequency (Ω) of 1.7 rad/s, the method of finding the mean amplitude is visualized in Figure 6.16. For an excitation frequency (Ω) of 1.7 rad/s, a sudden shift in force occurs at approximately 360 seconds. This shift is attributed to the turbulence induced by the forced oscillation. A visualization illustrating the cause of this sudden shift is provided in Figure 6.16.

$$F_{surge} = \frac{mean(peaks) - mean(troughs)}{2} \tag{6.12}$$

Figure 6.17 provides the time-steps at which force peaks are measured in the response for various excitation frequencies.

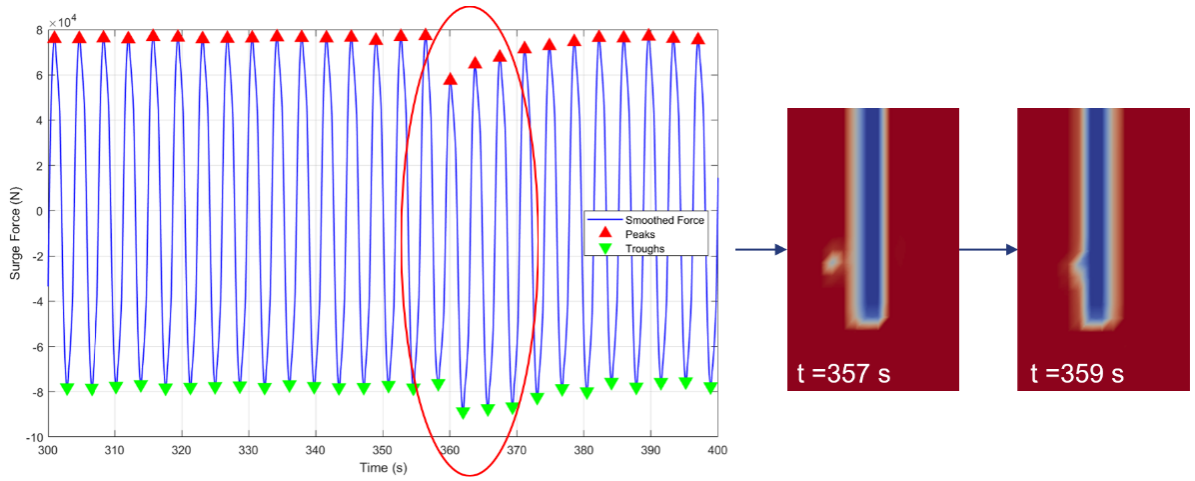

Figure 6.16: Graph of the peaks and troughs in the filtered surge force response. For this particular response, Ω is 1.7 rad/s, and the submergence is 10 meters. The cause of the response shift is visualized on the right, with the time steps indicated.

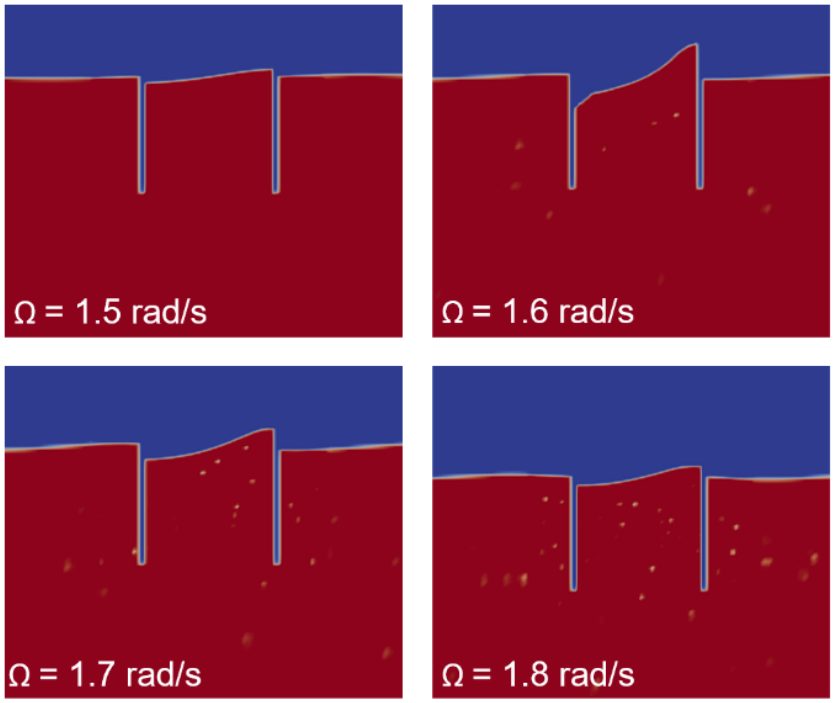

Figure 6.17: Time-step at which a force peak is measured in the response at different excitation frequencies. The geometry is submerged to h = 10 meter. The different excitation frequencies are provided in the bottom left of each visualization.

In Figure 6.18 the results are given in the frequency domain. In the upper figure, the phase difference between the motion and horizontal force on the geometry is given in degrees. In the lower figure, the horizontal force on the geometry in the is presented. The horizontal force on the geometry consists of an inertia force of the rigid liquid mass between the walls, the force acting on the interior structure, the force acting on the exterior structure and the viscous force acting on the walls. In Figure 6.18, a phase shift is evident at the frequency corresponding to the largest force on the geometry. This observed phenomenon is anticipated during sloshing resonance, as explained in Section 5.3.1. Nevertheless, there is no immediate occurrence of a 180-degree phase shift; instead, the phase shift gradually increases until reaching a 180-degree difference with the non-resonant fluid motion. Due to the viscous damping in CFD, the phase shift is less direct than that observed for in the LPF method (Section 5.3).

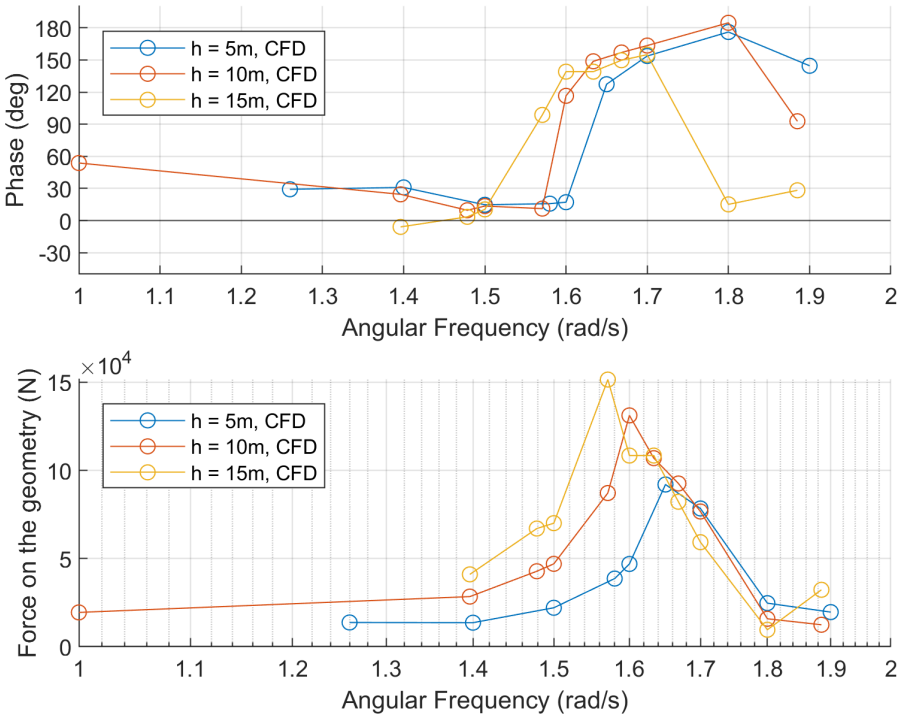

Figure 6.18: In the upper figure the phase angle between the force and the lateral motion is given. In the lower figure the absolute hydrodynamic force is presented. The structure remains vertical and is analysed at 3 different submergences (h).

6.5.2. Determination of the hydrodynamic properties

The added mass and damping can be determined based on the measured forces and motions [26].

The hydrodynamic coefficients will be derived for sinusoidal excitation in surge direction. The motion of the forced oscillation is defined by equation 6.13.

$$\eta(t) = \eta_a \cos(\Omega t) \tag{6.13}$$

The resulting forces on the oscillating object are given by equation 6.14, in which ε_{F_η} represents the phase difference between the force and the excitation.

$$F_\eta(t) = F_{\eta_a} \cos\left(\Omega t + \varepsilon_{F_\eta}\right) \tag{6.14}$$

The amplitudes utilized in the forced oscillation test are maintained at a level that allows the application of a linear approach. The (linear) equation of surge motion in the time domain for forced oscillation is provided by equation 6.15.

$$(m + a_{11})\ddot{\eta_1} + b_{11}\dot{\eta_1} = F_{\eta_{1a}} \cos\left(\Omega t + \varepsilon_{F_{\eta_1}}\right) \tag{6.15}$$

In equation 6.15, m represents the mass, a_{11} the added mass, b_{11} the damping. The stiffness in surge motion is equal to zero. $F_{\eta_{1a}}$ represents the force amplitude in surge direction.

Implementation of equation 6.13 and its time derivatives into equation of motion in surge (6.15), leads to equation 6.16.

$$-\eta_{1a}(m + a_{11})\Omega^2 \cos(\Omega t) + \eta_{1a} b_{11} \Omega \sin(\Omega t) = F_{\eta_{1a}} \cos(\varepsilon_{F_{\eta_1}}) \cos(\Omega t) - F_{\eta_{1a}} \sin(\varepsilon_{F_{\eta_1}}) \sin(\Omega t) \tag{6.16}$$

Due to the 90-degrees phase difference between the velocity and acceleration, the component of the exciting force in phase with the surge motion is related to inertia and stiffness, while the out-of-phase component is related to damping. Therefore the added mass (from $\Omega t = 0$) and damping (from $\Omega t = \frac{\pi}{2}$) obtained from equation 6.16, can be written as:

$$a_{11} = \frac{-\frac{F_{\eta_{1a}}}{\eta_{1a}} \cos(\varepsilon_{F_{\eta_1}})}{\Omega^2} - m \tag{6.17}$$

$$b_{11} = \frac{\frac{F_{\eta_{1a}}}{\eta_{1a}} \sin(\varepsilon_{F_{\eta_1}})}{\Omega} \tag{6.18}$$

The in-phase and out-of-phase parts of the excitation force during the CFD simulations will be determined. The added mass and damping are then computed based on this excitation force.

The in-phase and out-of-phase parts of the exciting force during an oscillation can be found from an integration over a whole number (N) of periods (T) of the measured signal F(t) multiplied with $cos(\Omega t)$ and $sin(\Omega t)$, respectively [26]:

$$F_a \sin \varepsilon_{F\eta_1} = \frac{2}{NT} \int_0^{NT} F(t) \cdot \cos \Omega t \cdot dt \tag{6.19}$$

$$F_a \cos \varepsilon_{F\eta_1} = \frac{2}{NT} \int_0^{NT} F(t) \cdot \sin \Omega t \cdot dt \tag{6.20}$$

These are the first order (and averaged) Fourier series components of $F(t)$ [26].

Phase difference

The phase difference between the forced surge motion and the force acting on the geometry is determined in the time domain. In Figure 6.15, the phase difference for a specific excitation frequency is visualized. The figure illustrates the results for the 2D representation of a vertical cylinder with an inner diameter of 11 meters and a submergence of 10 meters. The phase difference is utilized to determine the added mass and damping coefficients at that frequency. It serves as a measure of the damping present in the system. In the case of a substantial phase difference, the out-of-phase component of the force becomes more pronounced, indicating increased damping within the system.

Added mass and damping

The added mass and damping are determined using two methods. The first approach employs the phase difference approach, which utilizes the mean amplitude of the filtered force data (equation 6.12) and the phase difference, $\varepsilon_{F_{\eta_1}}$, to calculate the added mass and damping through equations 6.17 and 6.18. In the second approach, it is unnecessary to determine the phase difference. This method involves solving the integrals in equations 6.19 and 6.20 to find the in-phase force and the out-of-phase force, which are then applied in equations 6.17 and 6.18.

Figure 6.19 depicts the added mass (a_{11}) and damping (b_{11}) coefficients for a 2D structure at different submergences. First, focus on the red line, which indicates a submergence of h = 10 m. The material mass of the water between the two walls is $\rho h D_i \ kg$ per unit width. Which for this specific case is equal to 1.1e5 ($\rho = 1000kg/m3$). In Figure 6.19 it can be observed that the a_{11} approaches the material water mass at the lower oscillation frequencies. The added mass varies with frequency and is negative for Ω greater than the first sloshing frequency as shown in Figure 6.19. The added mass should not be interpreted as a physical mass. Because of this, the added mass can also have a negative value. A negative added mass indicates that the ”inertia force” acts in the opposite direction of the tank acceleration, or that we have an apparent reduction in the system mass. The occurrence of negative added mass is a widely recognized phenomenon in the context of the external flow issue surrounding a ship as well [17]. However, the damping b_{11} is positive, as it must be. The highest b_{11} values are present within a frequency range centered around the lowest sloshing frequency. A broader range of significant b_{11} values would have been observed if the damping ratio of the sloshing had been higher. In general, the damping increases as the ratio of liquid depth to wall gap (h/D_i) decreases [17]. This phenomena can be seen in the non-dimensionalized damping curves in Figure 6.20, where the largest damping is present at the lowest submergence (as the wall gap is equal for all cases).

In Figure 6.20 the results from Figure 6.19 are made dimensionless, to be able to analyse the influence of submergence on the added mass and damping. In Figure 6.20, it becomes evident that in the CFD method for a 2D open-ended structure, the frequency at which the first sloshing mode occurs reduces with an increasing submergence-to-breadth ratio (h/D_i). Furthermore, the amount of damping increases as the submergence-to-breadth ratio (h/D_i) decreases. However, it should be noted that the accuracy of the results depends on the number of excitation frequencies tested. Increasing the number of excitation frequencies at which the CFD simulations are carried out would enhance the reliability of the results.

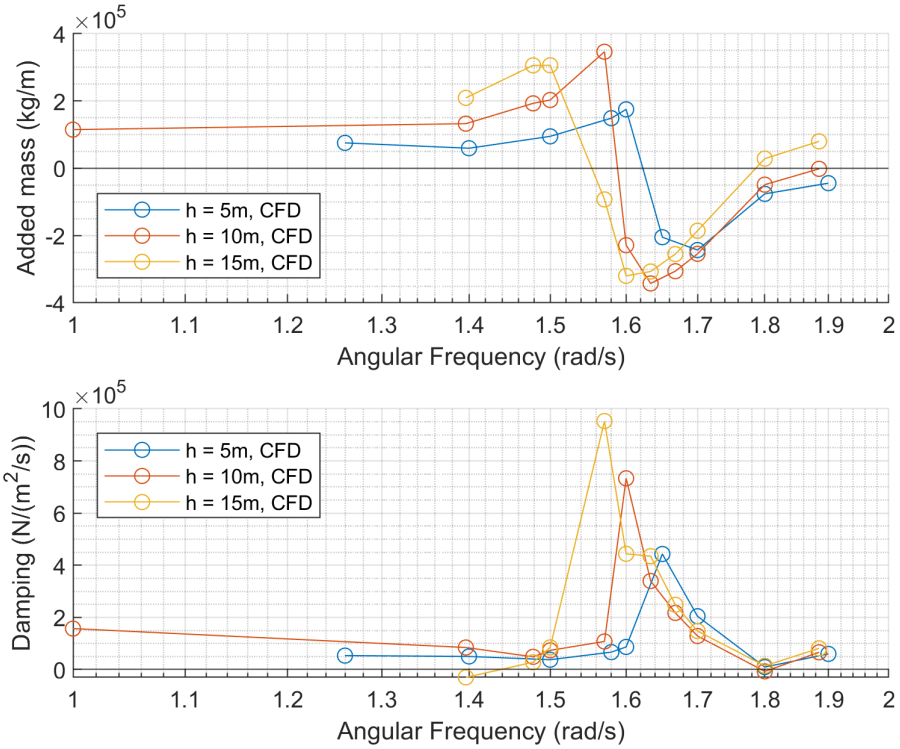

Figure 6.19: Added mass and damping of the 2D structure that is forced to oscillate in surge with amplitude η_{1a} = 0.1 m and angular frequency Ω, at various submergence h.

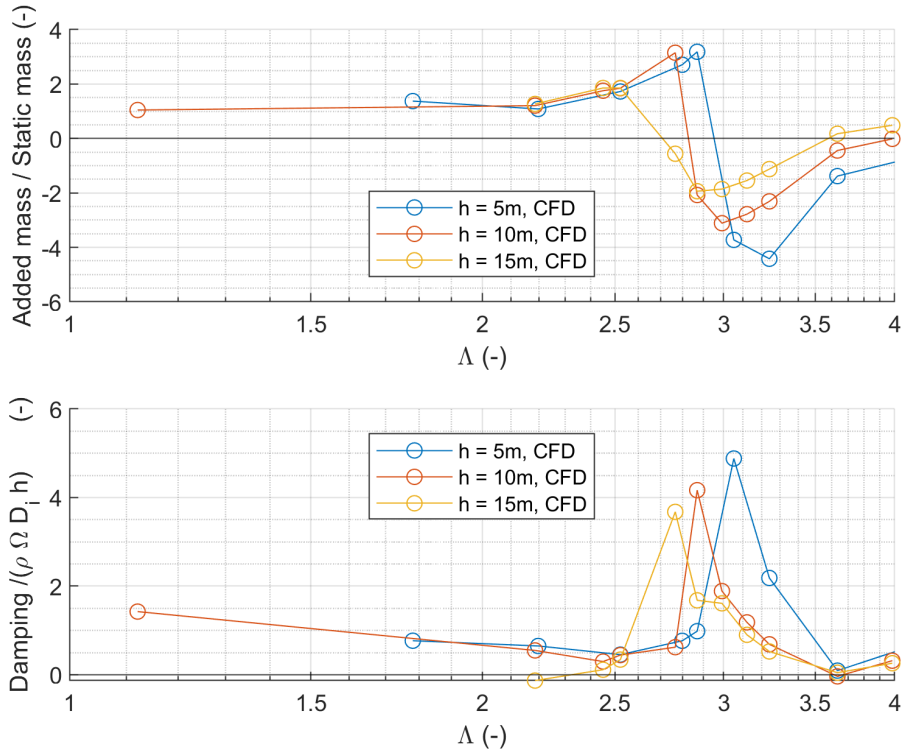

Figure 6.20: Non-dimensional added mass and damping of the 2D structure that is forced to oscillate in surge with amplitude η_{1a} = 0.1 m as a function of the non-dimensional excitation frequency Λ (= $\Omega^2 D_i/g$), at various submergence h.

6.5.3. Sloshing mode - 2D - Inclined

For the inclined analysis, the angles from Section 5.5 are followed, thus angles of 60, 45, and 40 degrees with respect to the horizontal. The submerged length has a constant value of L_s = 10 m. The surge excitation amplitude, η_{1a}, is adjusted according to the inclination angle such that the forcing amplitude-to-breadth ratio η_{1a}/B remains constant and equal to 0.0091. In this context, let B represent the breadth of the water surface between the two walls, defined as $B = D_i/\sin(\alpha)$. For inclination angles of 60, 45, and 40 degrees, this results in excitation amplitudes η_{1a} of 0.1155, 0.1414, and 0.1556, respectively.

For the inclined geometries, the same frequency domain analysis as explained in the previous section is carried out. The inclined geometry is not aligned with the fluid mesh, leading to a higher density of spurious pressure peaks in the pressure results compared to the upright case. As expected, mesh refinement does not counteract the occurrence of these spurious peaks, as it reduces the time step. In the present work, the same mesh as that used for the upright case is retained, and the Savitzky-Golay filtering method [63] is applied to remove spurious peaks.

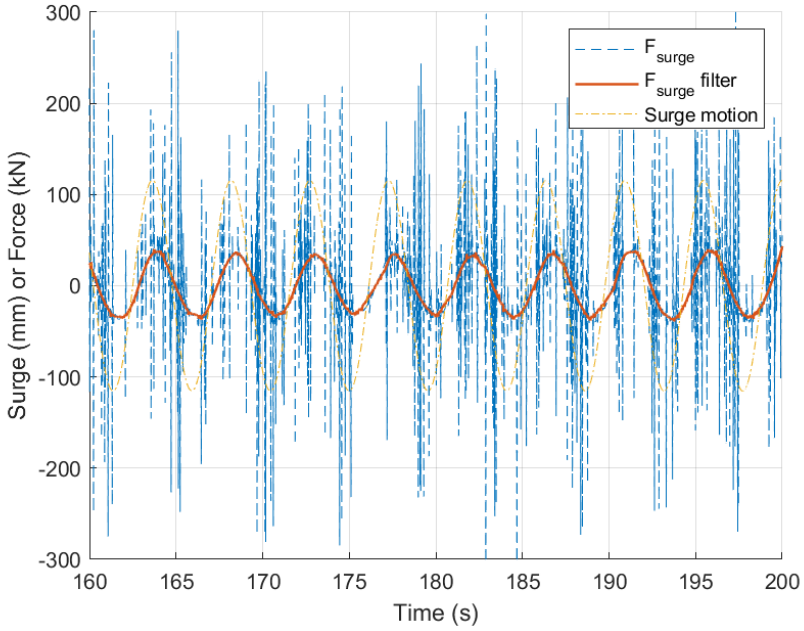

Figure 6.21: Time domain plot of the surge forced oscillation test in a 2D ComFLOW simulation with an amplitude of oscillation of $115mm$ and a period of $1.38rad/s$. The inclination angle (α) of the geometry is 60 degrees.

In the Figure 6.22 the added mass and damping values are given for the structure forced to oscillate in surge direction under an angle. The angles with respect to the horizontal are 60, 45 and 40 degrees respectively. As a reference, the results for the upright structure (α = 90 degrees) is also given in the figure. The analytical approximation for the first natural sloshing frequency is described in Section 4.3.3. The expectation is that the first natural sloshing frequency will decrease if the inclination angle with respect to the horizontal decreases, provided the submerged length remains constant. In other words, for decreasing angle, the free surface inside the structure will increase, causing the half wavelength that fits inside this structure to also increase. This increase in wavelength corresponds to a decrease in first natural sloshing frequency.

Comparison of the frequency at which sloshing resonance can be observed in the added mass and damping results (Figure 6.22) reveals agreement with the aforementioned expectation.

Furthermore, the magnitude of the added mass and damping terms in surge in the vicinity of the first sloshing mode significantly decrease when the inclination angle with respect to the horizontal is reduced.

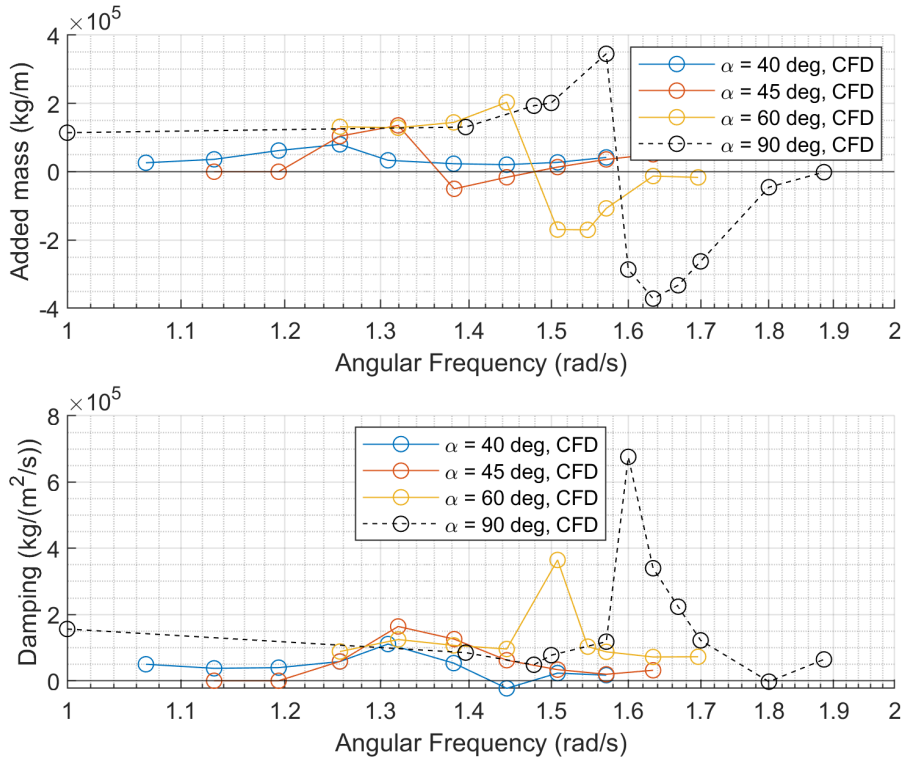

Figure 6.22: Added mass and damping of the 2D structure that is forced to oscillate in surge with an amplitude-to-length ratio η_{1a}/B of 0.0091 and excitation frequency Ω. The structure is under various inclination angles α with respect to the horizontal. The submerged length is L_s = 10 m.

7

Results

This chapter combines approaches from previous chapters to determine the best method for describing the researched phenomena.

7.1. Validation of LPF using CFD

In this section the results obtained from the LPF analysis conducted with Orcawave are validated with the CFD analysis conducted with ComFLOW. It is anticipated that the results should align consistently with both methods for frequencies away from the resonance frequency of the internal water column. However, in proximity to the resonance frequency, the LPF results tend towards infinity due to the linear approach. For frequencies near sloshing resonance, the objective is to obtain CFD results that more closely align with the physical phenomena occurring.

Two-dimensional models are employed to compare the LPF and CFD approaches. The emphasis is on comparing the results in terms of added mass and damping obtained from both methods near the first asymmetric sloshing frequency. The procedure utilizing LPF is detailed in Section 5.3.4, while the approach employing CFD is outlined in Section 6.5.2. The results for added mass and damping are presented for a model with a 2D geometry, featuring an inner diameter of 11 meters (D_i) and a wall thickness of 0.5 meters, at various submergences, and inclined at various angles with respect to the horizontal. In the presented forced oscillation CFD results, a motion-amplitude-to-breadth ratio (η_a/D_i) of 0.0091 is employed. A low ratio is chosen to prevent the free surface from behaving chaotically, causing substantial changes in the wetted area or significant water entry and exit between the geometric walls. This is desirable to facilitate a comparison of the CFD results with LPF results. The added mass and damping results from the CFD analysis are obtained through two methods, as explained in Section 6.5.2. The phase method, being more indirect, involves determining the phase angle first. Consequently, the integral method is employed to validate the outcomes of the phase method.

7.1.1. Upright structure

First, the 2D structure is compared in an upright position (α = 90 degrees), at various submergences. Focus is on the magnitude and the frequency of the sloshing resonance.

Added mass

The added mass in surge for submergence's h of 5, 10, and 15 meters, obtained from the OrcaWave and ComFLOW simulations, is presented in Figures 7.1a, 7.2a, and 7.3a, respectively. Additionally, in each figure, the analytical first asymmetric sloshing mode determined by Equation 4.19 is represented as a dotted vertical reference line. The submergence-to-breadth (h/D_i) ratio is 0.45 for a submergence of 5 meters, 0.91 for 10 meters, and 1.36 for 15 meters. As explained in Section 4.3.2, the analytical approximation is only valid when $h/D_i \gtrsim 1$. Therefore, it is expected that the resonance frequency for a submergence of 5 meters will deviate from the value determined analytically, as the deep liquid condition is not satisfied. For a submergence of 10 meters, the deep liquid condition is almost reached, and for a submergence of 15 meters, the deep liquid condition does apply. The fundamental natural sloshing frequency, based on linear potential flow theory, should accurately predict the resonance frequency

for the open structure if deep liquid conditions apply. This is also visible in the figures, where only at a submergence of h is 5 meters, the analytical determination does not match the linear potential flow result.

Then, consider the magnitude of the added mass in the OrcaWave method. In the OrcaWave method, viscous damping effects are neglected. A linear theory based on potential flow of an incompressible liquid predicts infinite steady-state response for a forcing frequency equal to a natural frequency of the liquid motion. However, there is a damping source due to the radiated waves, because of the open bottom of the structure. This damping is more severe if the submergence is smaller. This can be explained by considering the surface level of the internal water column. With increased submergence, the energy dissipating through radiation diminishes because of reduced interaction with the surface water level outside the cylinder.

The amplitude of the excitation is kept at a small value, therefore the surface water in the CFD simulation does not include chaotic behaviour or wave breaking, however the surface water behaviour (especially the wave run up) is not completely linear.

Looking at the oscillation frequencies away from the resonance frequencies, the results from OrcaWave and ComFLOW align well, indicating the a linear system description is correct and superposition is possible.

Damping

The damping in surge for submergence's h of 5, 10, and 15 meters, obtained from the OrcaWave and ComFLOW simulations, is presented in Figures 7.1b, 7.2b, and 7.3b, respectively.

As in the figures in which the added mass results are presented, in each figure, the analytical first asymmetric sloshing mode determined by Equation 4.19 is represented as a dotted vertical reference line.

Both methodologies exhibit peak damping values in the vicinity of the analytically determined first sloshing mode. However, the damping coefficients derived from the CFD analysis appear to influence a wider range of frequencies. In the LPF method, only radiation (or wave-making) damping is considered, while the CFD method incorporates viscous damping, resulting in a noticeable shift in the frequency at which the damping peaks. The difference in resonance frequency of the first sloshing mode suggests that damping due to flow separation around the bottom corners of the structure has a significant influence. This finding is supported by the work of Ravinthrakumar et al. [60]. The percentage deviations between the resonance frequencies from CFD and LPF for submergences of h = 5, 10, and 15 meters are 4.62%, 6.16%, and 7.87%, respectively.

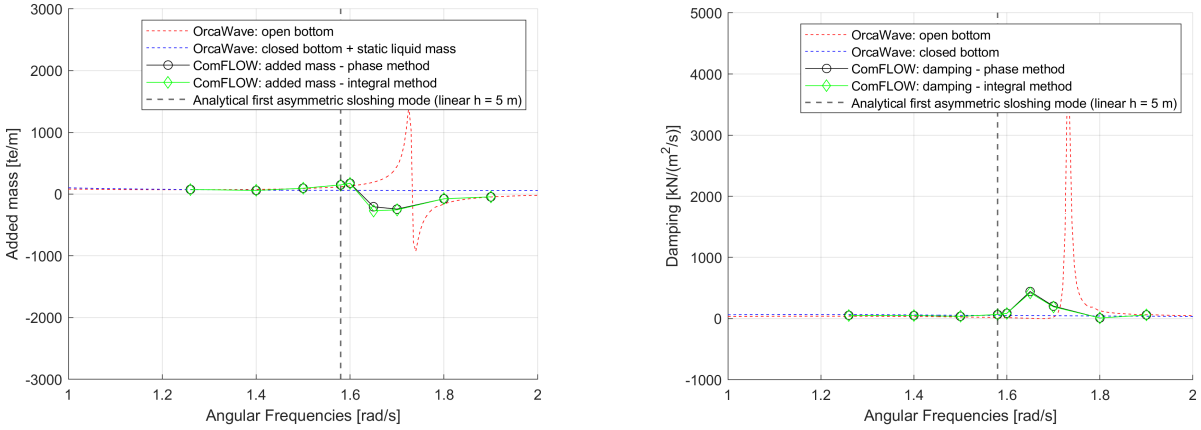

(a) Added mass

(b) Damping

Figure 7.1: Added mass and damping in surge direction for surge motion with a submergence of h = 5 meter.

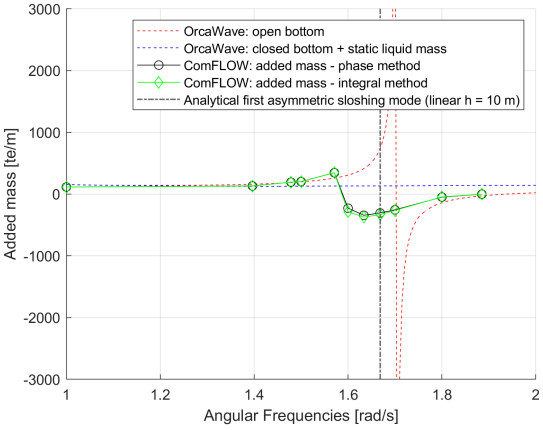

(a) Added mass

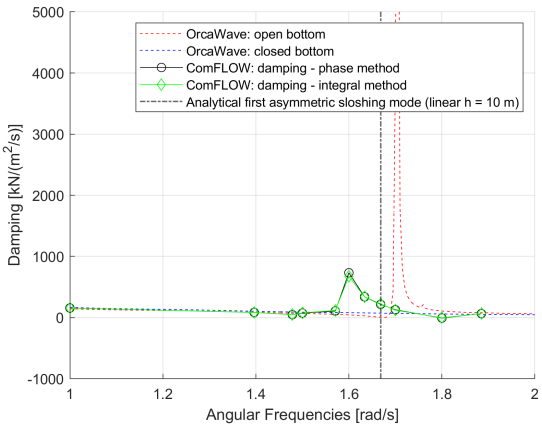

(b) Damping

Figure 7.2: Added mass and damping in surge direction for surge motion with a submergence of h = 10 meter.

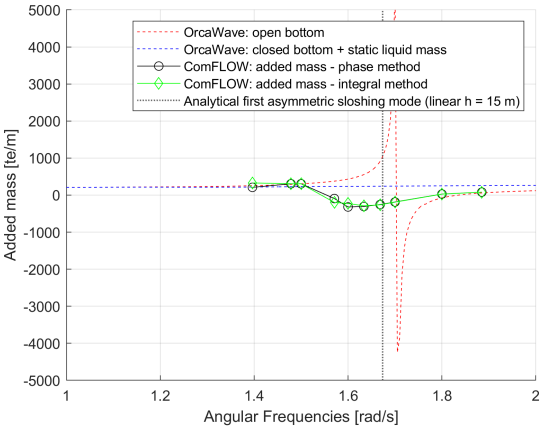

(a) Added mass

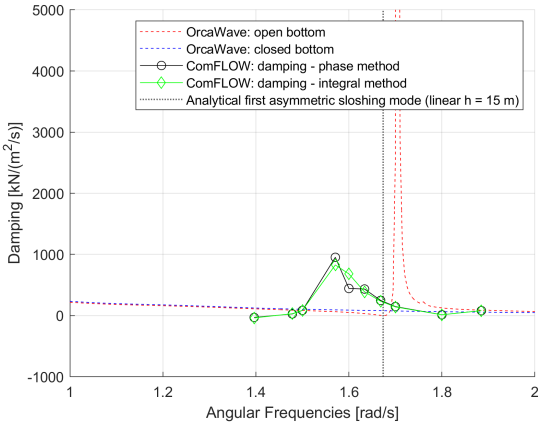

(b) Damping

Figure 7.3: Added mass and damping in surge direction for surge motion with a submergence of h = 15 meter.

7.1.2. Inclined structure

This section provides a preliminary comparison of the added mass and damping of the 2D structure around the first sloshing mode at various inclination angles. Figures 7.4, 7.5, and 7.6 show the results for inclination angles of 40, 45, and 60 degrees respectively. The similarities between the CFD results and the LPF results are not as pronounced as in the case of upright structures. One reason for this is the reduced excitation of sloshing as the inclination with respect to the horizontal decreases. The sloshing that does occur is less linear compared to the upright case because the walls are inclined. This inclination results in wave run-up on one side and breaking on the other, making it more challenging for sloshing resonance to be excited.

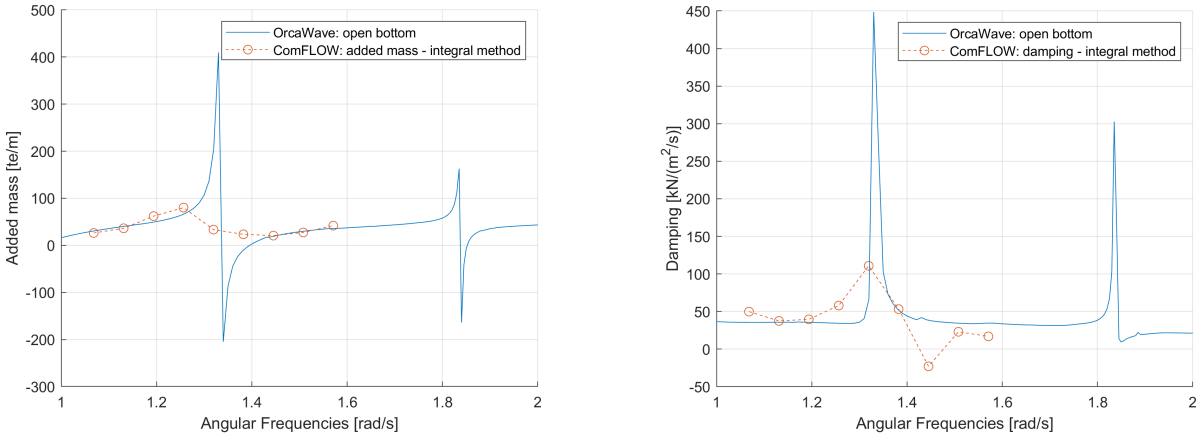

(a) Added mass **(b)** Damping

Figure 7.4: Added mass and damping in surge direction for surge motion with a submerged length of L_s = 10 meter. The angle with respect to the horizontal is 40 degrees.

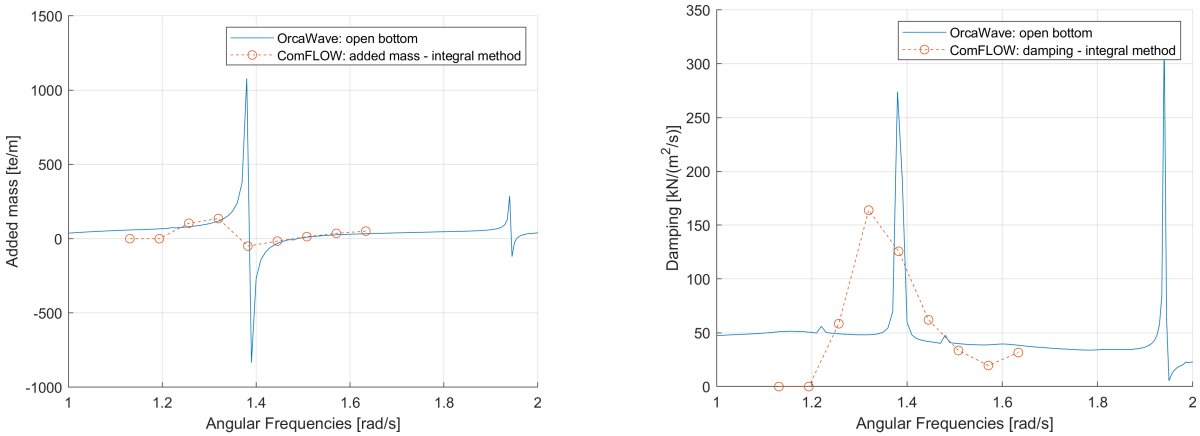

(a) Added mass **(b)** Damping

Figure 7.5: Added mass and damping in surge direction for surge motion with a submerged length of L_s = 10 meter. The angle with respect to the horizontal is 45 degrees.

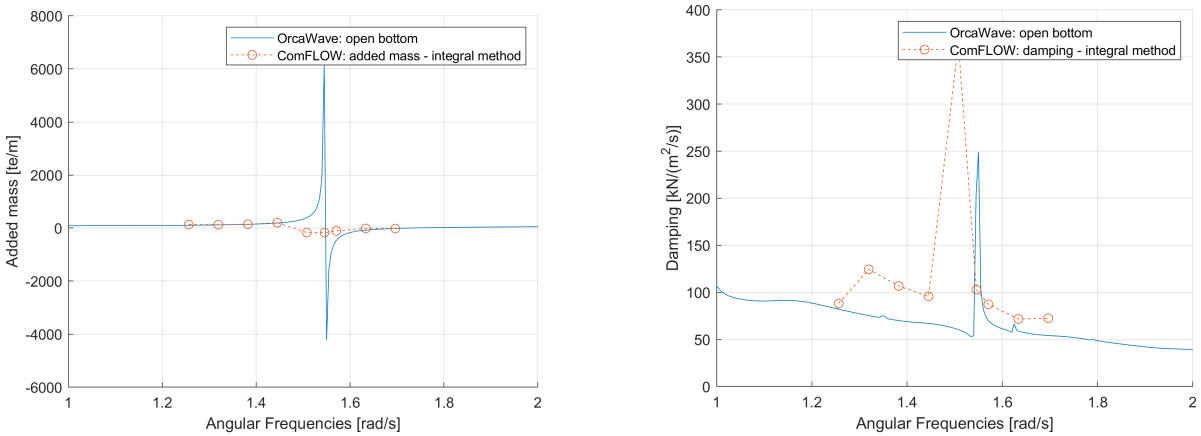

(a) Added mass

(b) Damping

Figure 7.6: Added mass and damping in surge direction for surge motion with a submerged length of L_s = 10 meter. The angle with respect to the horizontal is 60 degrees.

7.2. Modelling the sloshing resonance

The primary emphasis in this part is on the fundamental sloshing mode. This is because this specific mode generates the most noteworthy lateral movement of the center of gravity.

7.2.1. Damping lid for modelling purposes

As discussed in Section 5.3.3, a damping lid can be used to simulate additional damping for the internal water column in the LPF simulation. The CFD results can be employed to find the appropriate level of damping that the lid should impose on the surface water of the internal water column, to achieve a similar response. Figure 7.7 and 7.8 show the added mass and damping results from Figure 7.2a and 7.2b, with the addition of the LPF results for an open bottom structure with a damping lid between the walls. In the legend the damping coefficients ϵ are indicated. For modelling purposes the application of this damping lid can be used for a better estimation of the added mass and damping, following from the LPF results. In the specific case shown in Figure 7.7 and 7.8, a damping lid with a damping coefficient ϵ of 0.06, would be the best choice to approach the ComFLOW added mass and damping results around the first sloshing frequency. The damped natural frequency of the system is given by [47]:

$$\omega_d = \omega_n \sqrt{1 - \epsilon^2} \tag{7.1}$$

Thus the natural frequency decreases from its undamped value by a factor of $\sqrt{1-\epsilon^2}$, which in the case of ϵ = 0.06 is 0.9982. This is a very small shift, which is hardly visible in Figure 7.7. Therefore, the fact that the resonance frequency from OrcaWave does not match with the ComFLOW result is not addressed with this method.

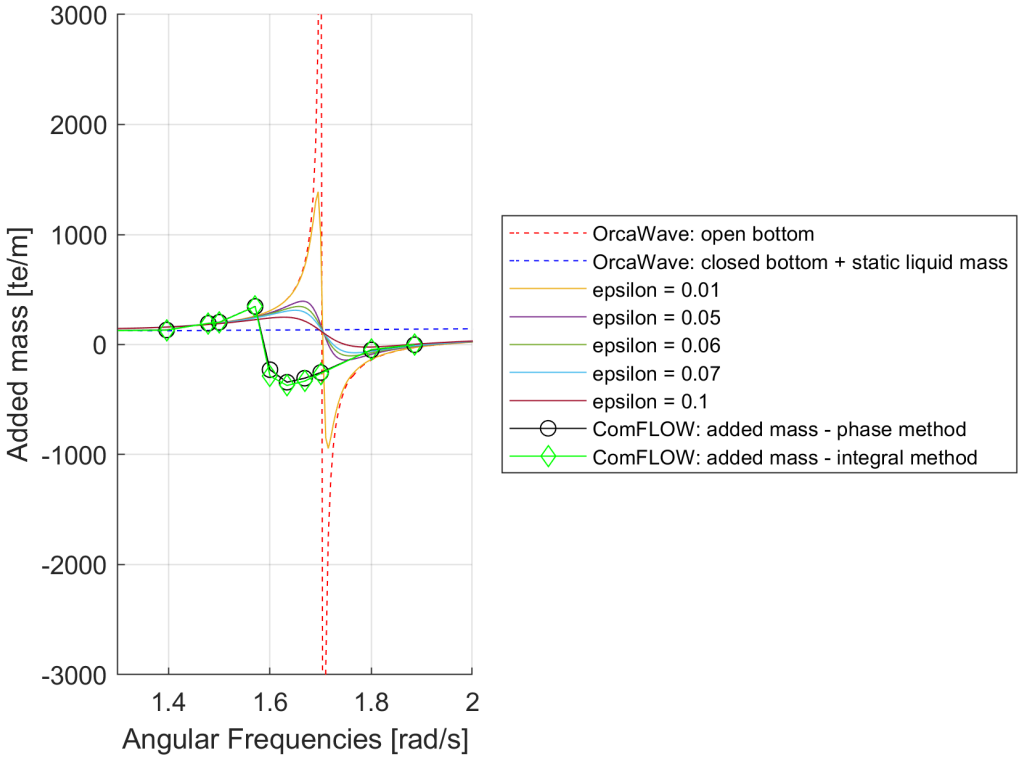

Figure 7.7: Added mass in surge direction for surge motion with a submergence of h = 10 meter. OrcaWave models including damping coefficients epsilon (ϵ) are also given.

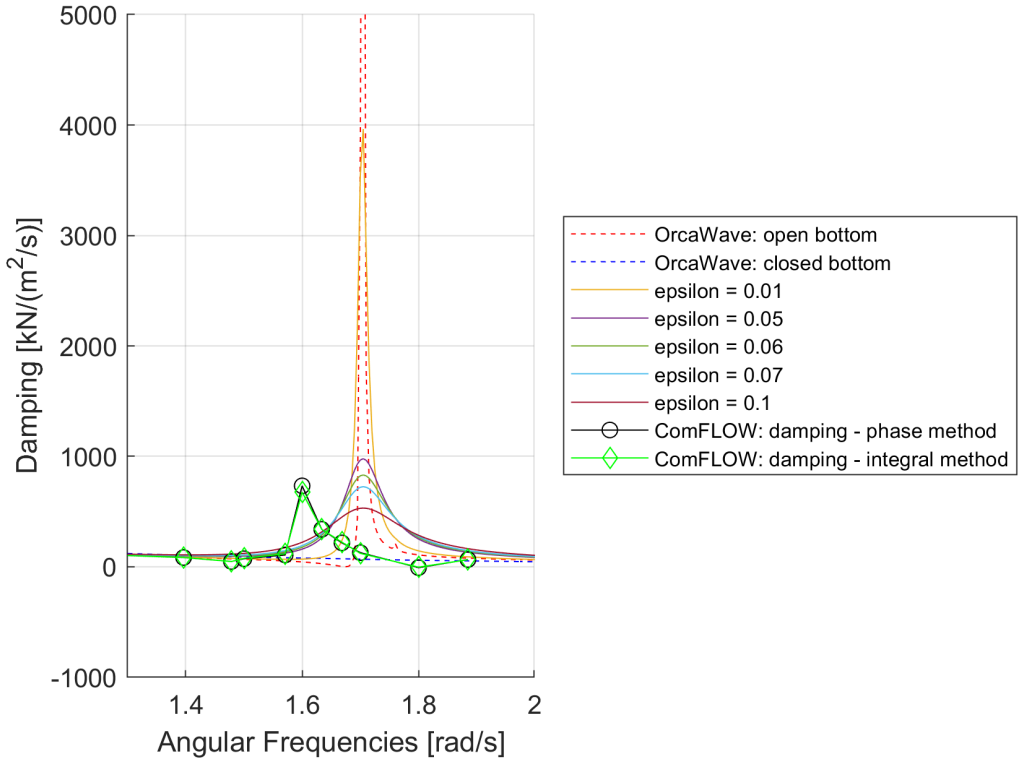

Figure 7.8: Damping in surge direction for surge motion with a submergence of h = 10 meter. OrcaWave models including damping coefficients epsilon (ϵ) are also given.

7.2.2. Hydrodynamic force ratio

To assess the impact of sloshing on the overall equation of motion, two models are compared. The first model contains a closed bottom geometry in which the mass of the internal water column at rest is equal to the mass of the internal water column of the open bottom geometry. The free surface of this internal water column is considered rigid. This model is referred to as ”frozen”. The second model is the open ended monopile in which the free water surface is not rigid, thus this model includes sloshing behaviour. This model is referred to as ”open”. The equation describing the total hydrodynamic force acting on the structure is given in respectively equation 7.2 and 7.3.

$$F_{frozen} = A_f \ddot{\eta_1} + B_f \dot{\eta_1} + C_f \eta_1 \tag{7.2}$$

$$F_{open} = A_o \ddot{\eta_1} + B_o \dot{\eta_1} + C_o \eta_1 \tag{7.3}$$

The ratio of these forces is given in equation 7.4.

$$\frac{F_{open}}{F_{frozen}} = \frac{A_o \ddot{\eta_1} + B_o \dot{\eta_1} + C_o \eta_1}{A_f \ddot{\eta_1} + B_f \dot{\eta_1} + C_f \eta_1} \tag{7.4}$$

The oscillatory motion in surge in complex notation is given by:

$$\eta_1 = \eta_{1a} e^{-i\omega t} \tag{7.5}$$

The velocity and acceleration of this oscillation are:

$$\dot{\eta_1} = -i\omega \eta_{1a} e^{-i\omega t} \tag{7.6}$$

$$\ddot{\eta_1} = -\omega^2 \eta_{1a} e^{-i\omega t} \tag{7.7}$$

Considering only the forced oscillation in the surge direction, the stiffness term C is omitted since there is no static stiffness in the surge direction. When equations 7.6 and 7.7 are applied to the remaining part of equation 7.4, the resulting complex value ratio is expressed in equation 7.8.

$$\frac{F_{open}}{F_{frozen}} = \frac{-\omega \eta_{1a} (\omega A_o + i B_o) e^{-i\omega t}}{-\omega \eta_{1a} (\omega A_f + i B_f) e^{-i\omega t}} \tag{7.8}$$

Then, several terms cancel each other out. The absolute value of the remaining term provides the hydrodynamic force ratio, as given in equation 7.9.

$$\frac{F_{open}}{F_{frozen}} = \left| \frac{\omega A_o + i B_o}{\omega A_f + i B_f} \right| \tag{7.9}$$

The hydrodynamic force ratio at the frequencies surrounding the resonance frequency is given in Figure 7.9. This figure illustrates the significance of the sloshing behavior within the internal water column around the fundamental sloshing frequency. As the submergence decreases, the relative impact of the sloshing behavior becomes more pronounced. This is expected since a relatively greater amount of the total mass of the internal water contributes to the hydrodynamic force due to sloshing at smaller submergences. Based on Section 6.5.3 it can be expected that the hydrodynamic force ratio observed for the upright structure near the first sloshing mode is higher than that for the inclined structures.

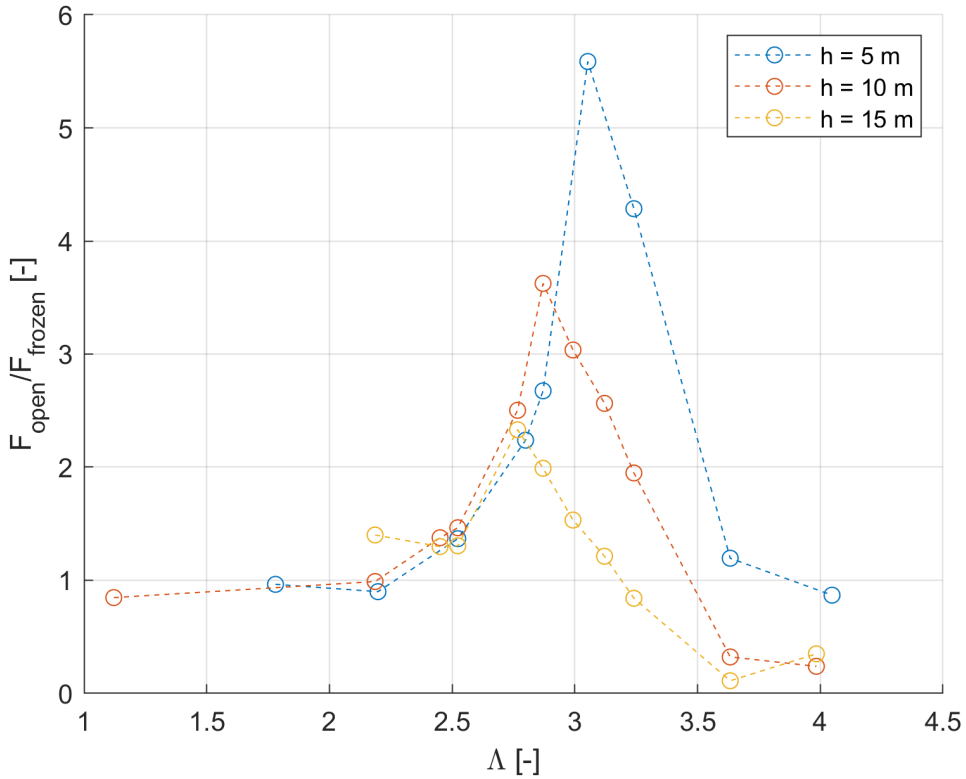

Figure 7.9: The hydrodynamic force ratio F_{open}/F_{frozen} as function of non-dimensional excitation frequency Λ (= $\omega^2 D_i/g$). The structure remains upright and the hydrodynamic forces at three submergences are analyzed.

8

Experimental model tests

Validation of the LPF method with CFD has its limitations. For example CFD results are not equivalent to actual wave loads due to uncertainties in the turbulence models. Better validation for the LPF method as well as the CFD method can be accomplished by doing model experiments. In other research focused on surface water elevation multiple measuring methods are presented.

8.1. Other model test in the research field

In research by Gabl et al. [18] two methods are used to capture the transient motion of the inner free surface without significantly impacting the fluid or structure response. The first method utilizes resistive wave gauges constructed from copper tape to measure the water run-up height on the structure's walls. The second method extends the conventional use of optical motion tracking to track the positions of randomly placed markers floating on the internal water surface.

The study by Moreau et al. [51] examines the damping characteristics of surge and pitch motions, as well as the first lateral sloshing mode, in a rigid free-floating upright circular dock equipped with bilge boxes and an open bottom. Experimental model tests are conducted using a 0.80 m diameter model subjected to regular waves with periods close to the highest natural sloshing period. Measurements are taken to assess the elevation of the internal free surface and the rigid body motions of the model using wave probes.

The thesis by Gerritsen [20] found for a vertical cylinder similar to this research, that close to the expected natural frequency for sloshing of the internal water mass, the water started to randomly show rotating sloshing behaviour, occurring either in a clockwise or counter-clockwise direction. This sloshing behaviour represents a non-linear phenomenon. This "rotary" sloshing or swirl behaviour is non-linear and can thus not be described by LPF, but it can be modelled in CFD and then validated with model tests. In the thesis by Gerritsen [20] the surface elevation inside the cylinder were measured during the 'forced oscillation' tests and the 'fixed model' tests. These sensors consists of a rigid plastic strip with on the sides two steel rods. These rods are connected to a instrumentation amplifier which shows the change of electrical resistance due to water. The average is taken of the two rods to give a reliable free-surface elevation.

The research by Balkema [4] focusses on the surface water penetration of inclined monopiles. In this research, only the piston mode resonance of the internal water column in taken into account, since natural sloshing modes are not expected to be present in the given sea state and geometry. The experiments carried out by Balkema [4] consist of measurement of the forces, motions and wave elevation. For the measurement of forces and motions, a hexapod is used to which the model is mounted during the experiments. For the wave elevation, seven wave probes are used. Three of these are located outside the model to measure the external wave elevation and four internal wave probes are used.

9 Conclusions

The results obtained in this study can serve as guidelines for a deeper understanding of the resonance behavior of the internal water column within a monopile during the installation cycle. Two methods to describe fluid behavior have been employed: one based on linear potential flow (OrcaWave) and one based on the Navier-Stokes equations (ComFLOW). The study concludes that viscous damping and nonlinearities in fluid flow significantly influence both the frequency of resonance and its consequences on hydrodynamic properties. This section will draw conclusions from the study based on the answers provided to the research questions.

9.1. Determination of the resonance frequencies

In this section the following secondary research question is addressed:

Can an analytical equation be employed to determine the frequencies of the piston mode and sloshing mode within the internal water column of both vertical and inclined monopiles?

To address this research question the piston mode and sloshing mode are treated separately.

Piston mode

The analytical derivations based on literature in Section 4.2, are based on linear theory, and serve as accurate approximations of the resonance frequencies induced by the piston mode in the 3D potential flow analysis (Figure 5.2).

However, there is a deviation between the 2D analytical piston mode frequency determination, based on a moonpool, and the frequency found in the LPF analyses of a thin walled cylinder. This can be explained by the 2D monopile representation being a thin-walled structure and the 2D analytical approximation is only valid in case of significant wall thickness.

In Section 4.2, analytical approaches are presented to evaluate the influence of the structure piercing the water surface at an inclined angle on the resonance frequencies. The expectation that the piston mode resonance frequency will decrease with a decreasing inclination angle relative to the horizontal, while the submerged length is constant, is confirmed with CFD (Section 6.4.2).

Sloshing

The analytical approaches based on literature in Section 4.3.4, consistently predict a lower fundamental (first asymmetric) sloshing frequency when compared to the 3D LPF approach. The relative deviation is about 1-2%, depending on the monopile diameter. (Figure 5.6 and Table 5.2).

For a 2D monopile representation, the fundamental sloshing frequency can closely be determined with the method described in Section 4.3.2, but only when the submergence-to-breadth ratio is $h/D_i \gtrsim 1$. If this is the case, the deep liquid condition is reached, and the free surface do not ”feel” the open bottom in LPF. When the ratio $h/D_i \gtrsim 1$ holds true, in CFD, the fundamental sloshing resonance frequency is lower than the frequency predicted by the analytical approximation and LPF (Section

7.1.1). The difference in resonance frequency of the first sloshing mode suggests that damping due to flow separation around the bottom corners of the structure has a significant influence.

In Section 4.3.3, analytical approaches are presented to evaluate the influence of the structure piercing the water surface at an inclined angle on the 2D sloshing resonance frequencies. The expectation that sloshing resonance frequencies decrease with a decreasing inclination angle relative to the horizontal, while the submerged length is constant, is confirmed with CFD (Section 6.5.3).

9.2. Accuracy of linear system description

In this section the following secondary research question is addressed:

Is it possible to describe the internal water behavior in an open-ended monopile accurately with linear theory, or is it necessary to take non-linearities into account?

To verify whether non-linearities should be taken into account, the results from the LPF (OrcaWave) analyses are compared with CFD (ComFLOW). To address this research question the piston mode and sloshing mode are treated separately.

Piston mode

First the 2D CFD model is validated with literature results (Section 6.3). The results indicate that the ComFLOW 2D CFD model successfully captures the observed trend in the gap resonance between two fixed bodies. Nevertheless, there is a discrepancy in the magnitude of the gap resonance when compared to findings from prior research, which could be attributed to the accuracy of the computational grid.

The piston mode resonance peak observed in the CFD results does not coincide with the value found in the LPF analysis. The discrepancy is attributed to viscous damping, primarily arising from flow separation at the lower edges of the geometry (Figure 6.6, 6.7, and 6.8). This phenomenon is not accounted for in LPF.

The piston mode resonance frequency for an inclined structure is found to be lower than for an upright structure if the submerged length is kept constant, as shown in Figure 6.9. This is in line with the expectation following from the approach in Section 4.3.3. However, only this trend is observed; the accuracy of the approach in Section 4.3.3 is not further tested. The reason for this choice was the observed difficulty in simulating the piston mode resonance in head waves using 2D CFD.

Sloshing

In Section 7.1.1, it is addressed that due to the nonlinear viscous flow in the CFD, a deviation in the first sloshing mode frequency is found between the LPF sloshing frequency and the CFD result. The percentage deviations between the resonance frequencies from CFD and LPF for a D_i of 11 meter, and at submergences of h = 5, 10, and 15 meters are 4.62%, 6.16%, and 7.87%, respectively. Thus, for an increase in submergence, the influence of radiation damping reduces, and viscous damping becomes more dominant. The dominance of viscous damping also explains the arbitrarily high amplitudes in added mass and damping in the LPF results, where viscous effects are not present.

In Section 6.5.3 it is demonstrated that, as the angle with respect to the horizontal decreases while keeping the forced oscillation amplitude-to-breadth ratio η_{1a}/B and submerged length L_s constant, the amplitudes of the added mass and damping around the first sloshing frequency decrease. Therefore, a more in-depth analysis with a focus on the hydrodynamic forces acting on the monopile is conducted for the upright case.

9.3. Effect of the resonance of the internal water column

In this section the following secondary research question is addressed:

Is it feasible to formulate a precise method for translating the motions of the internal water column into forces acting upon the monopile?

In Section 7.2.2, it is demonstrated that it is necessary to take non-linearities into account in the vicinity of the first sloshing mode. The hydrodynamic force acting on the structure due to sloshing of the internal water column ,compared to the "frozen" state, is significant (Figure 7.9). In Figure 7.9 it is demonstrated that at the highest amplitude of the hydrodynamic force at the first sloshing mode, the ratio F_{open}/F_{frozen}, for submergences of h = 5, 10 and 15 meter are, 5.59, 3.62 and 2.33, respectively. The hydrodynamic force F_{open} represents the open bottom CFD model and F_{frozen} the closed bottom LPF model with a static internal water column.

For modelling purposes the application of the damping lid can be used for a more accurate determination of the added mass and damping using the LPF method. The LPF calculations over-predict the peak values at resonance frequencies due to the absence of viscous damping in the method. Comparison with CFD enables the inclusion of a damping lid to mimic the viscous damping effect in the LPF model. However, it should be noted that the frequency at which sloshing occurs is not hardly effected by the damping lid, and although it is useful for engineering purposes, the damping lid does not incorporate the viscous damping effects present in the Navier-Stokes equations. For the specific case given in this study, a 2D monopile with D_i = 11 meter and a submergence of h = 10 meters, a damping lid coefficient of $\epsilon = 0.06$ is optimal (Section 7.2.1).

9.4. Primary research question

In this section the primary research question is addressed:

Is it possible to predict the internal water behavior, particularly resonance motions, in an open-ended monopile during the installation sequence, and what is the impact of this behavior on the overall motions of the monopile?

In the present work, more insight is gathered on predicting the internal water behavior inside an open-ended monopile. The impact of the sloshing behaviour is investigated in a 2D CFD approach. It can be concluded that employing 2D CFD is an effective method for predicting internal water behavior when used to verify LPF results. To increase confidence in the outcomes of the present work, experimental model tests should be conducted to validate the results, however this was not withing the scope of this work.

The present work does not explore the impact of the piston mode resonance on the overall motions of the monopile. Instead, it focuses on investigating the impact of the first sloshing mode, revealing a substantial increase in the hydrodynamic force magnitude due to sloshing resonance. These results should be evaluated in the context of the analyses, as it is found that, in certain circumstances, incident waves may not generate sloshing. This raises the question of whether waves during normal operation will be capable of exciting sloshing.

The current method of verifying the LPF method with 2D CFD has both advantages and shortcomings. A notable advantage is the use of small excitation amplitudes and incident wave heights in CFD, ensuring that the water surface behavior remains comparable to linear flow and providing a suitable comparison for the LPF method. Nevertheless, forced oscillation tests with larger amplitudes should be conducted to explore the effect of nonlinear chaotic sloshing. In the 2D approach, lateral motion of the surface water at sloshing resonance is observed, considered positive in this work due to its ability to be well-described in a linear manner. However, in the case of 3D CFD, swirling near the resonance frequency is expected.

10 Recommendations

This section provides recommendations for further related research, arranged by the different topics addressed in the present work.

10.1. Resonance behaviour

- Investigate the effect of the piston mode resonance on the overall motions of the monopile. In the present work only the effect of the first sloshing mode has been investigated.
- In the present work, the impact of the sloshing internal water column on the added mass and damping terms has been investigated. It would be valuable to further explore this aspect to establish a relationship between the potential flow approach away from resonance and a CFD approach in the vicinity of resonance.
- Empirically derive equations to estimate the resonance frequencies of open-ended inclined monopiles. In this study, assumptions regarding the resonance frequency caused by the inclination of the monopile are formulated and validated, yet overarching formulas are not established.

10.2. Monopile installation method

- Investigating mitigation measures to reduce internal sloshing during installation. Possible measures may include the use of internal solid or porous baffles.
- Include the influence of the vessel on the monopile during the operation. What is the interaction between the monopile and the ship during installation in terms of shielding and diffraction effects.
- Investigate the influence of directionality. The present work only focuses on head waves during the installation procedure, but other wave heading might induce different behaviour.

10.3. Environmental conditions

- Because the focus of this study was on resonance of the internal water column, forced oscillation and regular incident is employed. The study could be extended to also include irregular waves and current.
- Capture the motion of a monopile in an actual installation with a defined sea state. Examine the behavior of the internal water column and evaluate its response when encountering significant motions.

10.4. 2D CFD

- The present work employs CFD simulations in 1-phase flow. The use of 2-phase flow (both liquid and gas phase) might reduce the numerical pressure peaks in the CFD results and therefore increase the accuracy of the results.
- Investigate the effect of breaking waves and slamming. The present work focuses on small wave heights and motion amplitudes to maintain surface water behaviour that can be compared with

the linear potential flow. However, in certain sea states this assumption of linear surface water behaviour might not hold.
- Include a turbulence model in the CFD model for more accurate determination of the hydrodynamic loads on the geometry.
- Further investigate the computational grid for inclined geometries to find a suitable method to reduce the spurious peaks.
- In the present work, CFD analyses are conducted for a fixed diameter. Investigating the influence of the diameter on resonance frequencies provides valuable information, as demonstrated when the water surface area is increased due to inclination in the present study.

10.5. 3D CFD

- In the present work, preliminary analyses with 3D CFD have been conducted. During these analyses, beating appeared to significantly influence the response near the first sloshing mode, preventing the attainment of a steady state. Utilizing 3D CFD will allow for the modeling of more complex resonance behavior, such as swirling, thereby expanding the scope of the study.

10.6. Experimental model tests

- The present work necessitates an experimental model study to validate whether the findings from CFD around the resonance frequency show agreement.
- In experimental model tests the question of whether waves during the monopile installation operation will be able to excite sloshing can be examined.

10.7. Mechanical sloshing model

- Multiple studies have been conducted on representing the sloshing resonance as a pendulum or mass-spring system. This can be a suitable approach to standardize the expected forces due to resonant behaviour of the interal water column.

Bibliography

[1] H. Abramson. The Dynamic Behavior of Liquids in Moving Containers, with Applications to Space Vehicle Technology. Technical report, National Aerospace Space Administration (NASA), Special Publication SP-106, Washington D.C., 1966.

[2] H. N. ABRAMSON, W.-H. CHU, and G. E. RANSLEBEN. Representation of Fuel Sloshing in Cylindrical Tanks by an Equivalent Mechanical Model. *ARS Journal*, 31(12):1697–1705, 12 1961.

[3] B. Andersson, R. Andersson, L. Hakansson, M. Mortensen, R. Sudiyo, and B. Van Wachem. *Computational fluid dynamics for engineers*. Cambridge University Press, 2011.

[4] T. Balkema. Hydrodynamic loads on an inclined monopile in the splash zone, 2018.

[5] H. F. Bauer. Liquid sloshing in a cylindrical quarter tank. *AIAA Journal*, 1(11):2601–2606, 1963.

[6] B. Brodtkorb. PREDICTION OF WAVE-IN-DECK FORCES ON FIXED JACKET-TYPE STRUCTURES BASED ON CFD CALCULATIONS. Technical report, 2008.

[7] F. Bugg. Experimental determination of liquid oscillation frequency in an inclined right circular cylinder, 1970.

[8] T. Bunnik and A. Veldman. Modelling the effect of sloshing on ship motions. *Proceedings of the International Conference on Offshore Mechanics and Arctic Engineering - OMAE*, 1:279–286, 2010.

[9] X. Chang, I. Akkerman, R. H. Huijsmans, A. E. Veldman, and t. RHMHuijsmans. GENERATING AND ABSORBING BOUNDARY CONDITIONS FOR COMBINED WAVE-CURRENT SIMULATIONS. Technical report, 2016.

[10] F. Chen, Y. Lin, Y. Dong, and D. Li. Numerical investigations of soil plugging effect inside large-diameter, open-ended wind turbine monopiles driven by vibratory hammers. 38(1):83–96, 1 2019.

[11] X.-B. Chen. Hydrodynamics in offshore and naval applications-Part I. In *Keynote lecture of 6th Intl. Conf. HydroDynamics*, Perth (Australia), 2004.

[12] I. De Vries, Y. Roux, M. Naciri, and G. Bonnaffoux. DYNAMICS OF ENTRAPPED WATER IN LARGE DIAMETER TURRET MOONPOOLS. Technical report, 2013.

[13] DNV AS. DNV-RP-C205 Environmental conditions and environmental loads. Technical report, 9 2019.

[14] F. T. Dodge. *The new" dynamic behavior of liquids in moving containers"*. San Antonio, Texas, 2000.

[15] J. Falnes. *Ocean waves and oscillating systems : linear interactions including wave-energy extraction*. Cambridge University Press„ Cambridge ;, 2002.

[16] O. Faltinsen. *Sea loads on ships and offshore structures*, volume 1. Cambridge university press, 1993.

[17] O. M. Faltinsen and A. N. Timokha. *Sloshing*, volume 577. Cambridge University Press„ Cambridge :, 2009.

[18] R. Gabl, J. Steynor, D. Forehand, T. Davey, T. Bruce, and D. Ingram. Capturing the Motion of the Free Surface of a Fluid Stored within a Floating Structure. *Water*, 11(1):50, 12 2018.

[19] J. Gao, J. Zang, L. Chen, Q. Chen, H. Ding, and Y. Liu. On hydrodynamic characteristics of gap resonance between two fixed bodies in close proximity. *Ocean Engineering*, 173:28–44, 2 2019.

[20] J. Gerritsen. The hydrodynamics of a suspended cylinder in waves, 2017.

[21] B. K. Gupta and D. Basu. Offshore wind turbine monopile foundations: Design perspectives. 2020.

[22] R. Ibrahim. Liquid Sloshing Dynamics: Theory and Applications. Technical report, Cambridge University Press, 2005.

[23] B. Iwanowski and M. Lefranc. OMAE2009-79053 WAVE-IN-DECK LOAD ON A JACKET PLATFORM, CFD-DERIVED PRESSURES AND NON-LINEAR STRUCTURAL RESPONSE. Technical report.

[24] Z. Jiang. Installation of offshore wind turbines: A technical review. *Renewable and Sustainable Energy Reviews*, 139, 4 2021.

[25] Z. Jiang, R. Yttervik, Z. Gao, and P. C. Sandvik. Design, modelling, and analysis of a large floating dock for spar floating wind turbine installation. *Marine Structures*, 72:102781, 7 2020.

[26] J. M. J. Journée and W. W. Massie. OFFSHORE HYDROMECHANICS Second Edition (2008) Based on Original Lecture Notes (2000) by. Technical report.

[27] E. Kalker. Internal communication van oord. Subsea engineering department, March 2023.

[28] E. Kalker and A. Doss. Internal communication van oord. SINTEF model tests, February 2023.

[29] G. Katsikogiannis and R. Firoozkoohi. Model tests for van oord monopile upending operations. SINTEF Ocean AS, March 2023.

[30] G. Katsikogiannis and R. Firoozkoohi. Model Tests for Van oord monopile upending operations. Technical report, SINTEF Ocean AS, Trondheim, 2 2023.

[31] K. M. T. Kleefsman, G. Fekken, and A. E. P. Veldman. A Volume-of-Fluid based simulation method for wave impact problems. *Journal of Computational Physics*, 206:363–393, 2005.

[32] T. Kristiansen. *Two-Dimensional Numerical and Experimental Studies of Piston-mode Resonance*. PhD thesis, NTNU, Trondheim, 4 2009.

[33] T. Kristiansen and O. M. Faltinsen. A two-dimensional numerical and experimental study of resonant coupled ship and piston-mode motion. *Applied Ocean Research*, 32:158–176, 2010.

[34] V. J. Kurian, C. Y. Ng, and M. S. Liew. Dynamic responses of classic spar platforms subjected to long crested waves: Morison equation vs. diffraction theory. *ICSSBE 2012 - Proceedings, 2012 International Conference on Statistics in Science, Business and Engineering: "Empowering Decision Making with Statistical Sciences"*, pages 524–529, 2012.

[35] M. I. Kvittem, E. E. Bachynski, and T. Moan. Effects of hydrodynamic modelling in fully coupled simulations of a semi-submersible wind turbine. *Energy Procedia*, 24:351–362, 2012.

[36] C. H. Lee and J. N. Newman. Wamit user manual. *WAMIT, Inc*, 42, 2006.

[37] C. Li. Numerical Investigation of a Hybrid Wave Absorption Method in 3D Numerical Wave Tank. Technical Report 2, 2015.

[38] L. Li, Z. Gao, and T. Moan. OMAE2013-11200 NUMERICAL SIMULATIONS FOR INSTALLATION OF OFFSHORE WIND TURBINE MONOPILES USING FLOATING VESSELS. 2013.

[39] L. Li, Z. Gao, and T. Moan. Operability Analysis of Monopile Lowering Operation Using Different Numerical Approaches. *International Journal of Offshore and Polar Engineering*, 26(2):88–99, 2016.

[40] L. Li, Z. Gao, T. Moan, and H. Ormberg. Analysis of lifting operation of a monopile for an offshore wind turbine considering vessel shielding effects *. 2014.

[41] Y. Liu. Introduction of the Open-Source Boundary Element Method Solver HAMS to the Ocean Renewable Energy Community.

[42] L. Lu, B. Teng, L. Cheng, L. Sun, and X. Chen. Modelling of multi-bodies in close proximity under water waves-Fluid resonance in narrow gaps. *Science China: Physics, Mechanics and Astronomy*, 54(1):16–25, 1 2011.

[43] L. Lu, B. Teng, L. Sun, and B. Chen. Modelling of multi-bodies in close proximity under water waves - Fluid forces on floating bodies. *Ocean Engineering*, 38(13):1403–1416, 9 2011.

[44] S. Malhotra and S. Malhotra. Selection, Design and Construction of Offshore Wind Turbine Foundations. *Wind Turbines*, 4 2011.

[45] S. A. Mavrakos and D. N. Konispoliatis. Hydrodynamics of a free floating vertical axisymmetric oscillating water column device. *Journal of Applied Mathematics*, 2012, 2012.

[46] W. A. McNeill and J. P. Lamb. Fundamental sloshing frequency for an inclined, fluid-filled right circular cylinder. *Journal of Spacecraft and Rockets*, 7(8):1001, 1970.

[47] H. R. Miller and A. Mattuck. 18.03 Differential Equation. *MIT*, 2004.

[48] B. Molin. On the piston and sloshing modes in moonpools. *J. Fluid Mech*, 430:27–50, 2001.

[49] B. Molin, F. Remy, A. Ledoux, N. Ruiz, A. Ledoux, and N. Ruiz. Effect of roof impacts on coupling between wave response and shloshing in tanks of LNG-carriers EFFECT OF ROOF IMPACTS ON COUPLING BETWEEN WAVE RESPONSE AND SLOSHING IN TANKS OF LNG-CARRIERS. 2008.

[50] N. Moradi, T. Zhou, and L. Cheng. Effect of inlet configuration on wave resonance in the narrow gap of two fixed bodies in close proximity. *Ocean Engineering*, 103:88–102, 5 2015.

[51] M. Moreau, T. Kristiansen, B. Ommani, and B. Molin. An upright bottomless vertical cylinder with baffles floating in waves. *Applied Ocean Research*, 119:102934, 2 2022.

[52] J. R. Morison, M. P. O'brien, J. W. Johnson, and S. A. Schaaf. The Force Exerted by Surface Waves on Piles. *Journal of Petroleum Technology*, 2(05):149–154, 5 1950.

[53] A. Nematbakhsh, E. E. Bachynski, Z. Gao, and T. Moan. Comparison of wave load effects on a TLP wind turbine by using computational fluid dynamics and potential flow theory approaches. *Applied Ocean Research*, 53:142–154, 2015.

[54] J. Newman. Marine Hydrodynamics. Technical report, 1977.

[55] J. N. Newman. Algorithms for the free-surface Green function. *Journal of Engineering Mathematics*, 19:57–67, 1985.

[56] D. Norske Veritas. RECOMMENDED PRACTICE DET NORSKE VERITAS AS Self-elevating Units. 2012.

[57] Orcina Ltd. Orcina Ltd - the home of OrcaFlex, 2023.

[58] P. van der Plas. ComFLOW reference pages, 2018.

[59] M. H. Patel and J. A. Witz. *Compliant offshore structures*. Butterworth-Heinemann, 2013.

[60] S. Ravinthrakumar, T. Kristiansen, B. Molin, and B. Ommani. A two-dimensional numerical and experimental study of piston and sloshing resonance in moonpools with recess A two-dimensional numerical and experimental study of piston and sloshing resonance in moonpools with recess A Two-Dimensional Numerical and Experimental Study of Piston and Sloshing 2 Resonance in Moonpools with Recess. *Journal of Fluid Mechanics*, 877:142–166, 2019.

[61] J. S. Reeves. The Jones Act and the Denunciation of Treaties. *American Journal of International Law*, 15(1):33–38, 1 1921.

[62] T. Saitoh, G. Miao, and H. Ishida. Saitoh, T., Miao, G. P., & Ishida, H. (2006, June). Theoretical analysis on appearance condition of fluid resonance in a narrow gap between two modules of very large floating structure. *Proceedings of the 3rd Asia-Pacific Workshop on Marine Hydrodynamics*, pages 170–175, 6 2006.

[63] R. W. Schafer. What is a savitzky-golay filter? *IEEE Signal Processing Magazine*, 28(4):111–117, 2011.

[64] V. Sharma, C. O. Arun, and I. R. Praveen Krishna. Development and validation of a simple two degree of freedom model for predicting maximum fundamental sloshing mode wave height in a cylindrical tank. *Journal of Sound and Vibration*, 461:114906, 2019.

[65] W. Sheng, E. Tapoglou, X. Ma, C. J. Taylor, R. M. Dorrell, D. R. Parsons, and G. Aggidis. Hydrodynamic studies of floating structures: Comparison of wave-structure interaction modelling. *Ocean Engineering*, 249, 4 2022.

[66] L. Tan, L. Cheng, and T. Ikoma. Damping of piston mode resonance between two fixed boxes. *Physics of Fluids*, 33(6), 6 2021.

[67] L. Tan, L. Lu, G. Q. Tang, L. Cheng, and X. B. Chen. A viscous damping model for piston mode resonance. *Journal of Fluid Mechanics*, pages 510–533, 2019.

[68] P. Van Der Plas. Local grid refinement for free-surface flow simulations. Technical report, 2017.

[69] C. P. Van Steensel and A. Metrikine. An Analysis of the Dynamic Behaviour of a Noise Mitigation System During Installation, 2016.

[70] M. R. Vetrano, K. U. Leuven, P. Colinet, and A. Simonini. Reference Image Topography technique applied to harmonic sloshing. Technical report, INTERNATIONAL SYMPOSIUM ON PARTICLE IMAGE VELOCIMETRY -, 2015.

[71] P. P. Vijith, S. Viswanathan, and R. Panneerselvam. Moonpool effects on a floating body. Technical report, 2014.

[72] H. Wang and J. M. Falzarano. Energy extraction from the motion of an oscillating water column Simple Analytical Models for Parametric Roll in Longitudinal Irregular Seas View project Ocean Wave Energy Converters (OWEC) View project Energy extraction from the motion of an oscillating water column. *Ocean Systems Engineering*, 3(4):327–348, 2013.

[73] P. Wellens. Wave Simulation in Truncated Domains for Offshore Applications. Technical report, 2012.

[74] R. Wemmenhove, R. Luppes, A. E. Veldman, and T. Bunnik. Application of a VOF method to model compressible two-phase flow in sloshing tanks. *International Conference on Offshore Mechanics and Arctic Engineering*, 48227:603–612, 1 2008.

[75] S. R. Winterstein, A. K. Jha, and P. R. De Jong. MOTIONS OF A SPAR BUOY IN RANDOM SEAS: COMPARING PREDICTIONS AND MODEL TEST RESULTS Extreme Response of Marine Structures and Ships View project Reliability of Wind Turbines View project Probability-Based Engineering MOTIONS OF A SPAR BUOY IN RANDOM SEAS: COMPARING PREDICTIONS AND MODEL TEST RESULTS. 2:333–347, 1997.

A

Appendix A: Grid resolution

A.1. Gap resonance

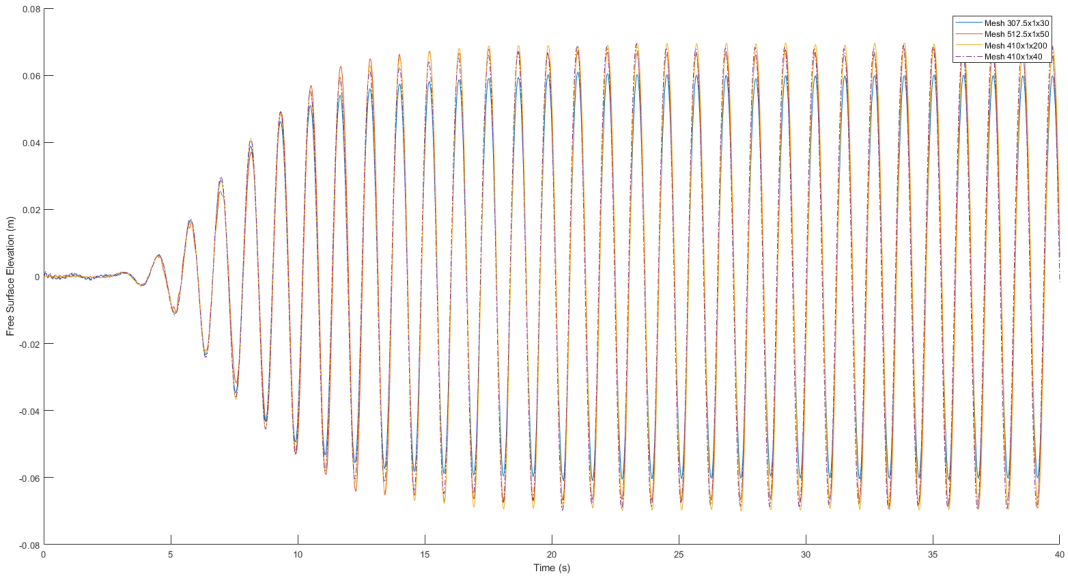

(a) Surface elevation in the gap in full 40 second run.

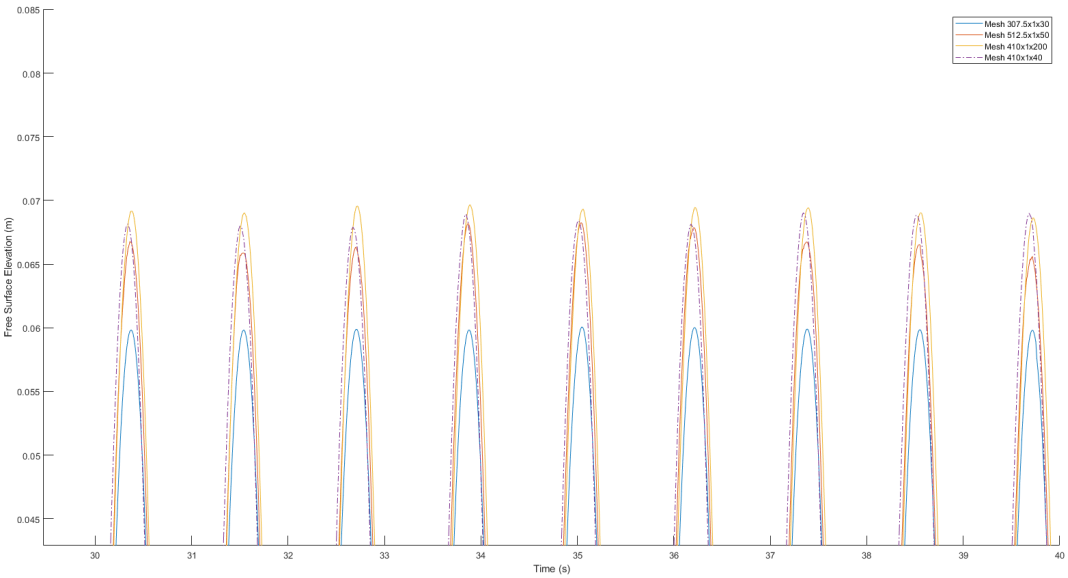

(b) Zoom of the positive peaks of the surface elevation in the range of 30-40 seconds.

Figure A.1: Dependence of the free-surface elevation at the desired focus position (i.e., in the center of the gap) on the grid resolution for regular waves with wave number $kD = 1.6$ or frequency $\omega_g = 5.38 rad/s$ and incident wave height $H = 0.024m$.

A.2. Piston mode

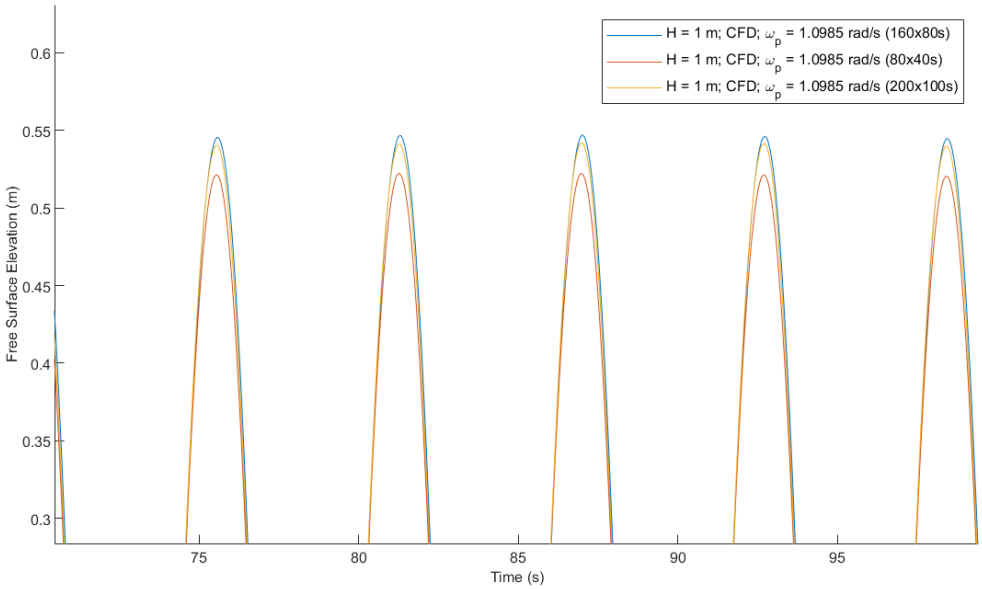

Figure A.2: Zoom of the positive peaks of the surface elevation at the incoming face of the geometry at different grid resolutions. Free surface elevation measurement between the two geometry walls. Geometry present at a submergence of $h = 5m$, an incident wave frequency of $\omega = 1.0985 rad/s$ and an incident wave height of $H = 1m$.

A.3. Sloshing mode

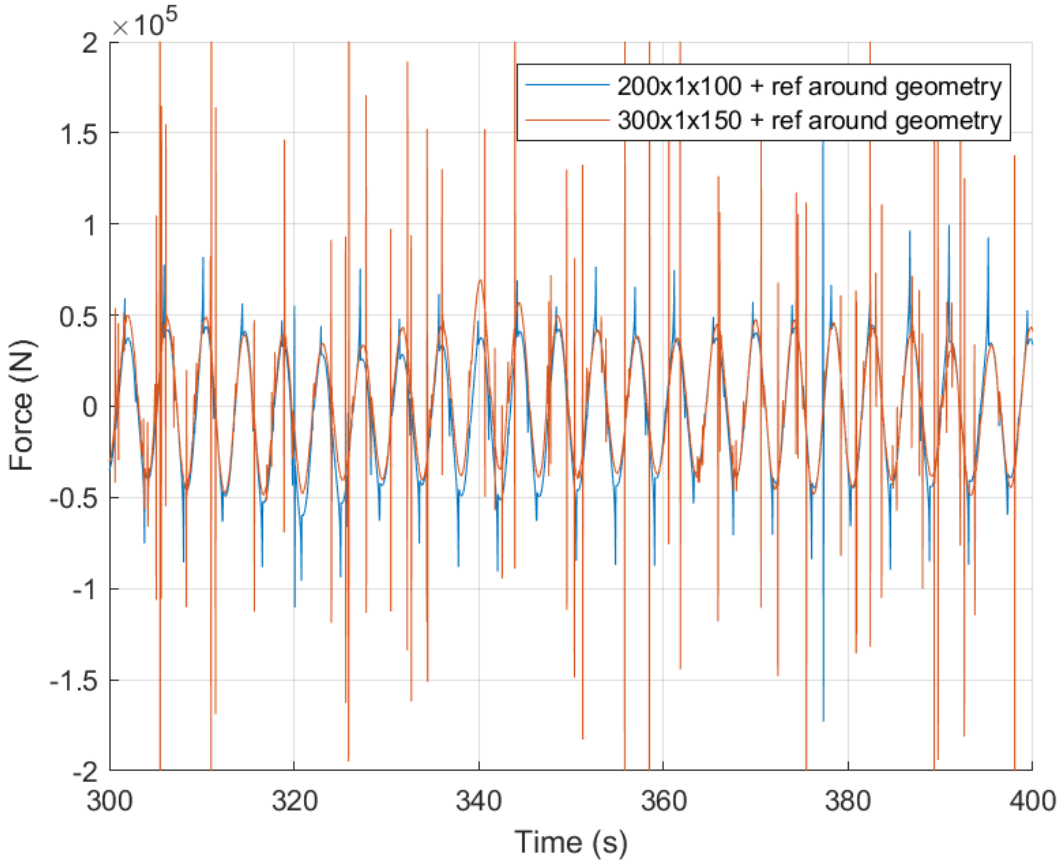

Figure A.3: The hydrodynamic force measurement at an excitation frequency of $\omega = 1.48 rad/s$ for the grid used in the analysis (blue) and the a finer grid (red). Both grids are refined around the geometry and stretched in the z-direction from the still waterline.

B

Appendix B: Potential theory (OrcaWave)

B.1. Governing equations

The linear radiation-diffraction analysis is conducted in OrcaWave. Therefore, the terminology used by this method is presented [57]. The assumption is made that the flow of the fluid is incompressible, inviscid, and is irrotational. The velocity of the fluid is represented by the gradient of a scalar function Φ, known as the velocity potential. The velocity potential, Φ, satisfies Laplace's equation within the fluid domain:

$$\nabla^2\Phi(\boldsymbol{X},t)=0 \tag{B.1}$$

After performing substitutions in the Navier-Stokes equation and subsequent integration, the resulting outcome is the Bernoulli equation, which is an expression that relates pressure within a fluid flow system:

$$p(\boldsymbol{X},t)=-\rho(\frac{\partial\Phi}{\partial t}+\frac{1}{2}(\nabla\Phi)^2+gZ) \tag{B.2}$$

B.1.1. First-order equations

The linear boundary value problem for the first-order complex potential $\phi^{(1)}$ is given by:

$$\phi=\phi_I+\phi_S+\phi_R \tag{B.3}$$

where ϕ_I is the potential of the incident wave, ϕ_S is the scattered potential due to the presence of a fixed obstructing body, and ϕ_R is the radiation potential caused by first-order motion of the body in the fluid.

B.1.2. Boundary value problems

The fluid domain, V, is the volume occupied by the fluid. This domain is enclosed by the surface of the body, S_B, the water free surface, S_F, and the seabed,S_{SB}. If infinite-depth water is considered, $Z\to-\infty$, the seabed boundary is not present. For all components of the first-order complex potential, $\phi^{(1)}$, the following general boundary value problems are present:

$$\begin{aligned}
\nabla^2\Phi&=0 && \boldsymbol{X}\in V\\
\frac{\partial\Phi}{\partial n}&=q_B(\boldsymbol{X}) && \boldsymbol{X}\in S_B\\
g\frac{\partial\Phi}{\partial n}-\omega^2\phi&=q_F(\boldsymbol{X}) && \boldsymbol{X}\in S_F\\
\frac{\partial\Phi}{\partial Z}&=0 && Z\to-\infty \quad (or \boldsymbol{X}\in S_F)
\end{aligned} \tag{B.4}$$

The forcing functions q_B and q_F are different for each component in equation B.3.
These three-dimensional partial differential equations on the unbounded domain, V, are reduced to the two-dimensional problem of finding the unknown ϕ on the surface S_B. Therefore Green's theorem and the boundary integral equation method are used ([55]), which will be elaborated on in Section B.1.3.

B.1.3. The potential formulation

The potential formulation, based on the values of ϕ, provides the most precise estimates for fundamental results, including added mass and damping, load RAOs (Response Amplitude Operators), and displacement RAOs.
Upon applying Green's theorem, the outcome is an integral equation that expresses the potential on the body surface:

$$2\pi\phi(\boldsymbol{X})+\int_{S_B}\phi(\xi)\frac{\partial G}{\partial n_\xi}\mathrm{d}S_\xi=\int_{S_B}q_B(\xi)G\mathrm{d}S_\xi+\int_{S_B}\frac{q_B(\xi)}{g}G\mathrm{d}S_\xi \quad \boldsymbol{X}\in S_B \tag{B.5}$$

where $G(\boldsymbol{X},\xi)$ is the classical Green's function for the problem. To simplify the appearance of the equation, the arguments of G are omitted, with the understanding that every occurrence of G represents $G(\boldsymbol{X},\xi)$ for the sake of clarity. The notation $\mathrm{d}S_\xi$ is used to emphasize that ξ is the dummy integration variable in each of the surface integrals in equation B.5. The notation $\frac{\partial}{\partial n_\xi}$ represents the normal

derivative with respect to the ξ variable, denoted as $\boldsymbol{n}(\xi) \cdot \nabla_{\xi}$. Equation B.5 is solved assuming that ϕ is constant on each mesh panel of S_B.

Green's Theorem

The classical Green's function, denoted as $G(\boldsymbol{X}, \xi)$, which represents the complex potential of the response to a point source at ξ. It is defined in the absence of a body and a damping lid, and therefore satisfies the general boundary value problem with ϵ, q_F, and q_B all equal to zero, and no body surface S_B. This well-known and well-understood Green's function serves as a fundamental component in the OrcaWave model.

C

Appendix C: Analytical forced oscillation description for a 3D cylinder

C.1. Fundamental sloshing mode

The linear surface elevation resulting from a sinusoidal external excitation of the liquid contained in the cylindrical geometry can be described analytically. When sinusoindal surge oscillation is considered, the surface elevation inside the cylinder is found with the following equation [22]:

$$\begin{aligned} \eta_1(t) &= \eta_{1a} \cdot \sin \Omega t \\ \eta(r,\theta,t) &= \frac{\eta_{1a}\Omega^2}{g} \cos(\theta) \cos(\Omega t)[r+B] \\ B &= \sum_{i=1}^{\infty} \frac{2R}{\left(\iota_{1,i}^2 - 1\right)} \frac{\Omega^2}{\left(\omega_{1,i}^2 - \Omega^2\right)} \frac{J_1\left(\iota_{1,i} r/R\right)}{J_1\left(\iota_{1,i}\right)} \end{aligned} \tag{C.1}$$

In equation C.1, the first asymmetric mode, $m = 1$, is considered. The variables r and θ represent cylindrical coordinates from figure 4.7. Equation C.1 shows, that when the applied oscillation frequency, Ω, approaches the natural frequency $\omega_{1,i}$, the solution becomes unbounded due to the invalidation of the linearized theory [70]. The maximum surface elevation occurs at $r = R$, $\theta = 0$, and $\Omega t = \pi/2$, represented by equation C.2 [22].

$$\begin{aligned} \eta(r,\theta,t) &= \frac{\eta_{1a}\Omega^2}{g}[r+B] \\ B &= \sum_{i=1}^{\infty} \frac{2R}{\left(\iota_{1,i}^2 - 1\right)} \frac{\Omega^2}{\left(\omega_{1,i}^2 - \Omega^2\right)} \end{aligned} \tag{C.2}$$

Zero wave height (nodes) occurs at $r = 0$, $\theta = \pi/2, 3\pi/2, ...$

In Figure C.1 a visualization of an instance of the free surface shape during forced oscillations at its maximum displacement is given. The parameters belonging to Figure C.1 are given below.

Radius R[mm]	40
Level L[mm]	$2.4R$
Excitation amplitude A[mm]	1.2
Dimensionless excitation Ω/ω_{1i}	0.9

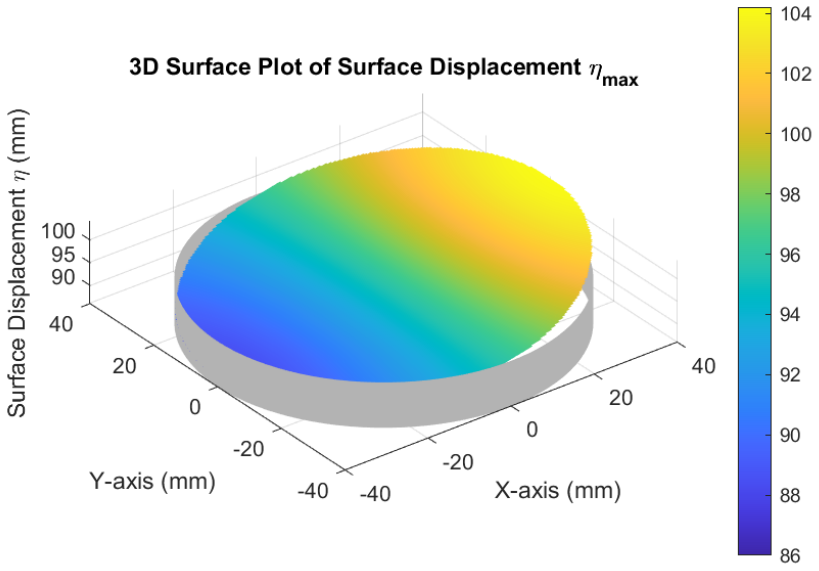

Figure C.1: 3D surface plot of surface displacement η_{max}.

D

Appendix D: Analysis of 2D forced oscillation results

In this section the force filtering as it is applied to the forced oscillation results for the upright structure being submerged to h = 10 meter is shown. The same method has been applied to the other CFD hydrodynamic force results.

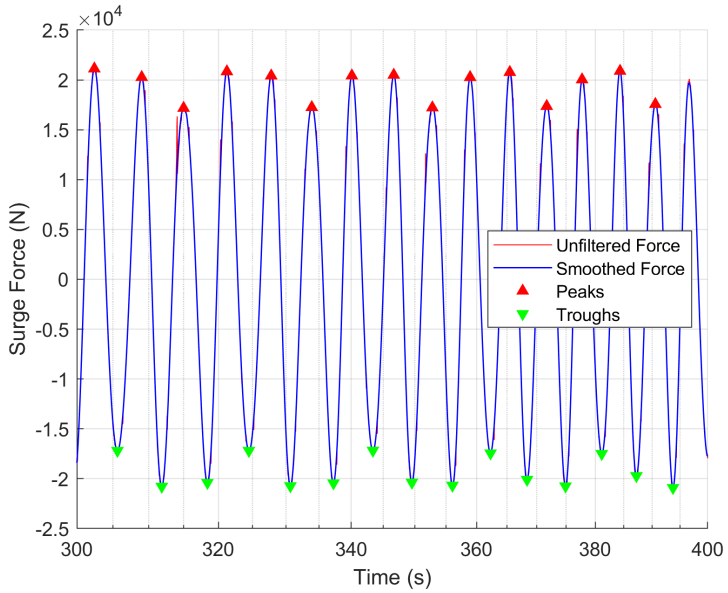

Figure D.1: Result of hydrodynamic force in surge for an upright structure, submerged to h = 10 meter. The excitation frequency Ω = 1 rad/s.

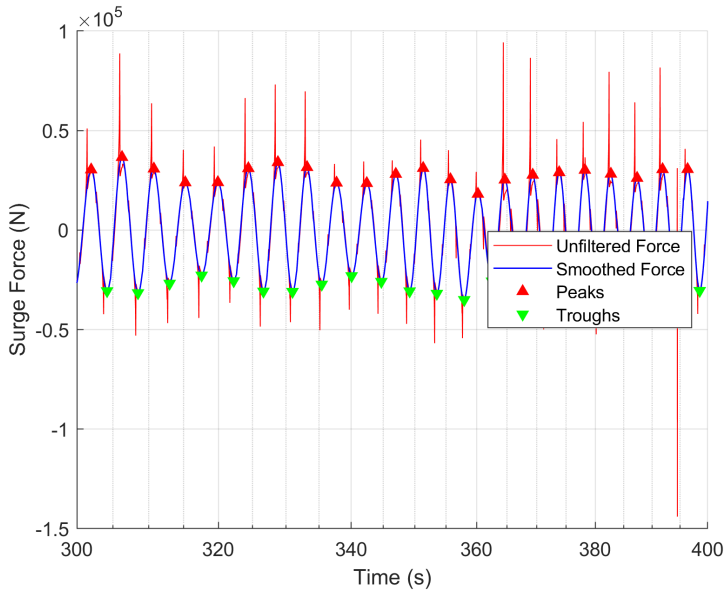

Figure D.2: Result of hydrodynamic force in surge for an upright structure, submerged to h = 10 meter. The excitation frequency Ω = 1.40 rad/s

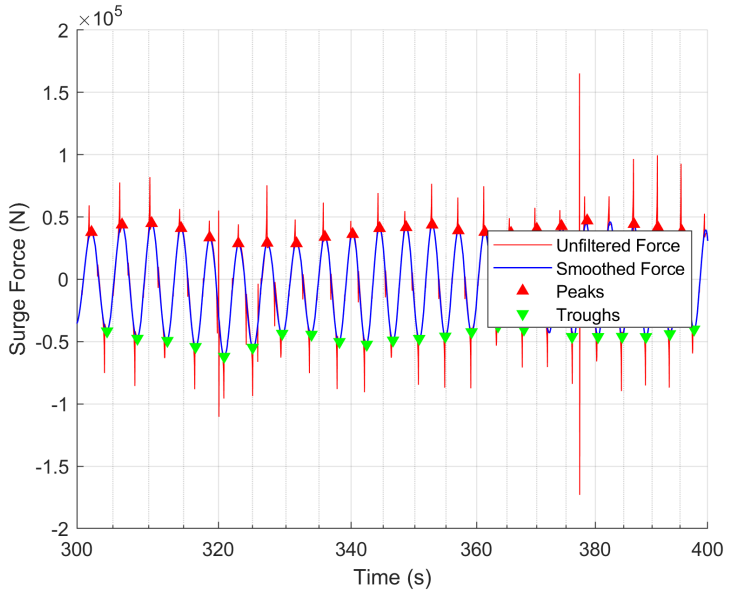

Figure D.3: Result of hydrodynamic force in surge for an upright structure, submerged to h = 10 meter. The excitation frequency Ω = 1.48 rad/s

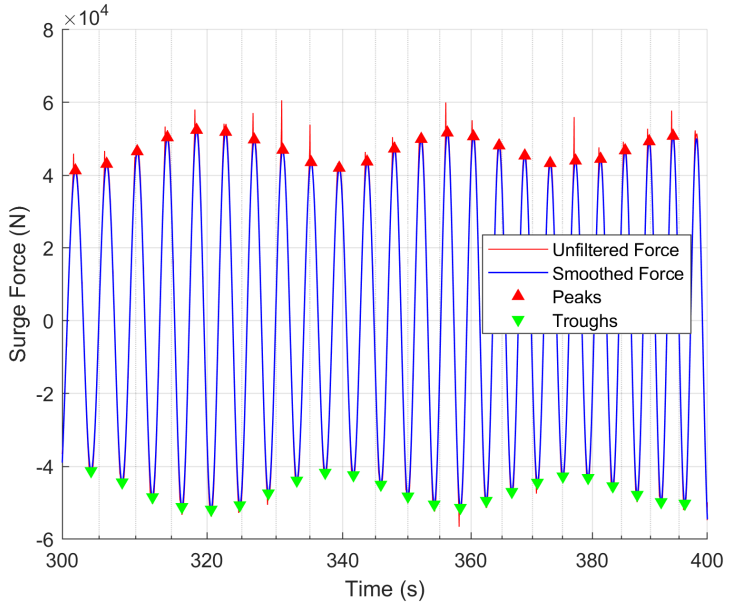

Figure D.4: Result of hydrodynamic force in surge for an upright structure, submerged to h = 10 meter. The excitation frequency Ω = 1.5 rad/s

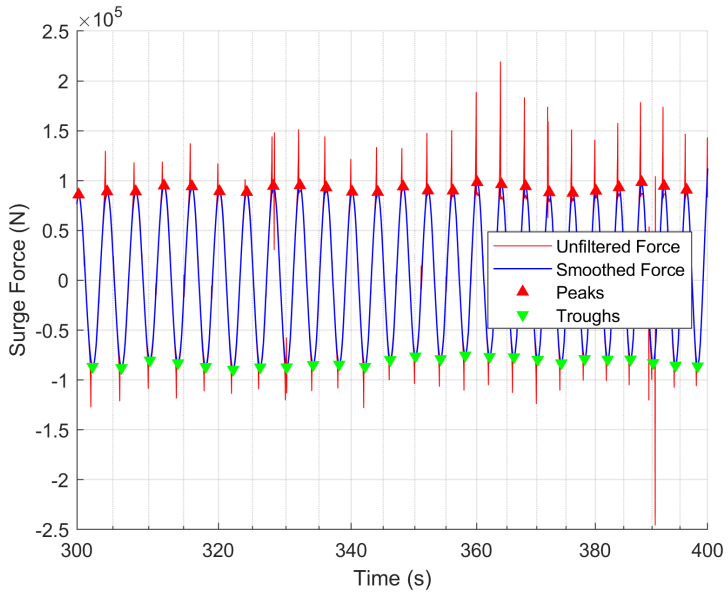

Figure D.5: Result of hydrodynamic force in surge for an upright structure, submerged to h = 10 meter. The excitation frequency Ω = 1.57 rad/s

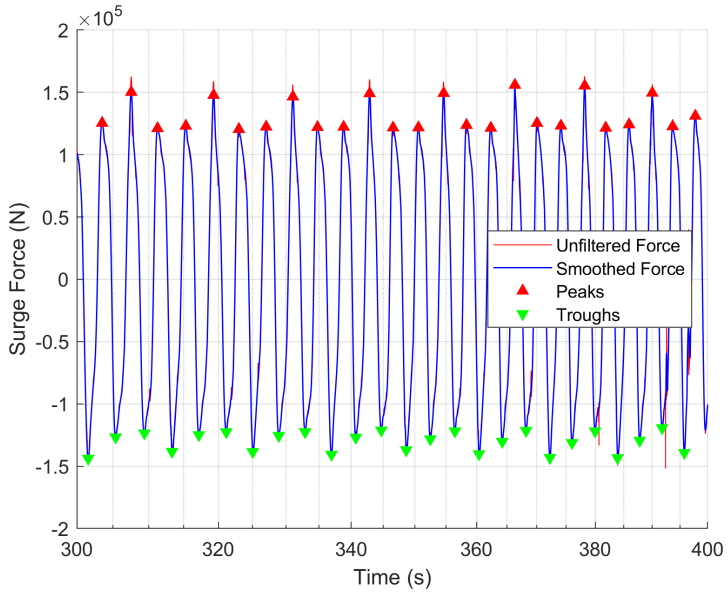

Figure D.6: Result of hydrodynamic force in surge for an upright structure, submerged to h = 10 meter. The excitation frequency Ω = 1.6 rad/s

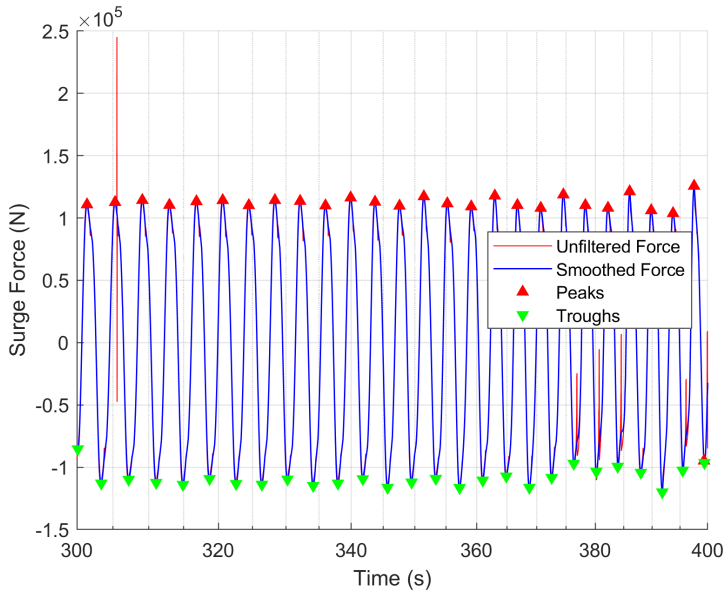

Figure D.7: Result of hydrodynamic force in surge for an upright structure, submerged to h = 10 meter. The excitation frequency Ω = 1.63 rad/s

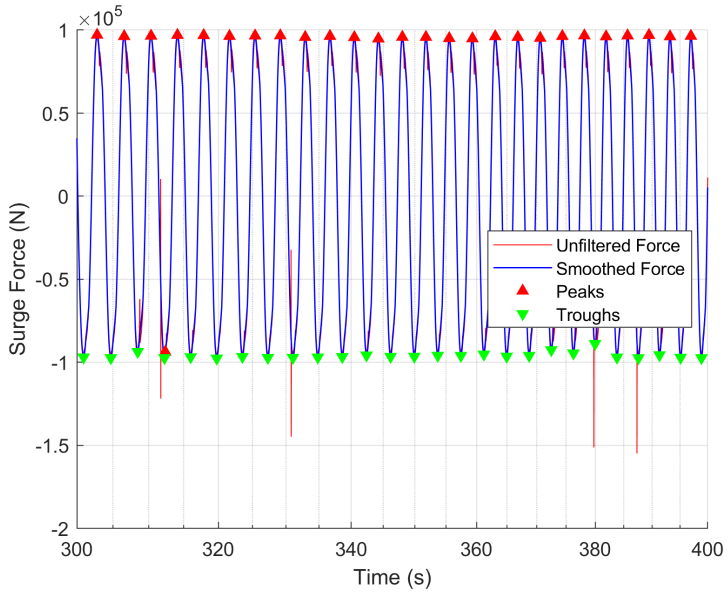

Figure D.8: Result of hydrodynamic force in surge for an upright structure, submerged to h = 10 meter. The excitation frequency Ω = 1.67 rad/s

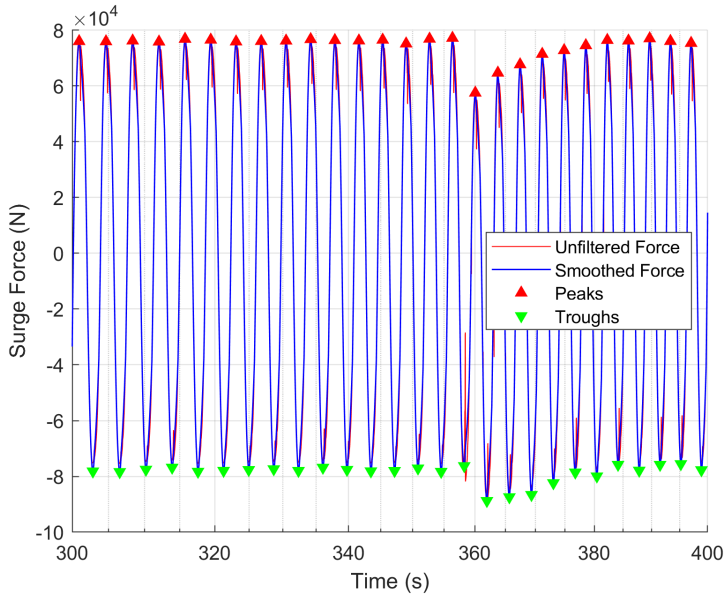

Figure D.9: Result of hydrodynamic force in surge for an upright structure, submerged to h = 10 meter. The excitation frequency Ω = 1.7 rad/s

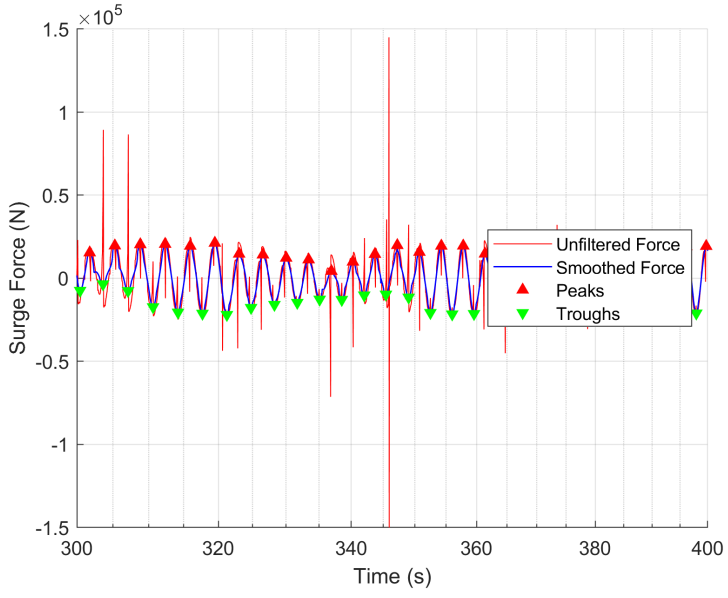

Figure D.10: Result of hydrodynamic force in surge for an upright structure, submerged to h = 10 meter. The excitation frequency Ω = 1.8 rad/s